CO_2 Dynamics in the Greenland Sea

as Observed by an Argo Float and a 1-D Mixing Model

Ingrid Sælemyr

A thesis presented for the degree of
**Master of Science
in Marine Biogeochemistry**

Geophysical Institute
University of Bergen
June 2023

Acknowledgements

Ingrid Sælemyr
Bergen, June 2nd 2023

Abstract

The Greenland Sea is one of few areas where open ocean convection occurs. It is therefore an important sink of anthropogenic CO_2. While the carbon inventory of the region is well known, the dynamics of the processes governing carbon uptake remain unclear. The difference between pCO_2 in the ocean and the atmosphere determines if there is uptake or outgassing, and DIC is the main driver of ocean pCO_2 variability. It is therefore essential to decompose the importance of physical *versus* biological drivers on DIC. Here, a mixed layer budget was used to carry out this decomposition. Physical fluxes from the mixed layer budget, *i.e.* vertical fluxes and air-sea gas exchange, were estimated using a one dimensional mixing model. Net community production was estimated as a residual between DIC calculated from measurements from an Argo float and model output. To this end, an existing PWP model tuned for the Greenland Sea was improved by including biogeochemistry and air-sea gas exchange. This is the first time these components have been added to a Price Weller Pinkel (PWP) model tuned to this region. A scheme to reinitialize the model for every Argo profile was implemented in order to facilitate estimates of net community production. Model calculations resulted in vertical transport of $15\pm15\%$ g C m^{-2} y^{-1} into the mixed layer and $27\pm22\%$ g C m^{-2} y^{-1} of carbon uptake from the atmosphere. Net community production in the upper 20 dbar was deterimed as the residual, and was $39 \pm27\%$ g C m^{-2} y^{-1}. Gas exchange was strongest in the productive season, while winter convection led to outgassing of CO_2 due to the large amounts of DIC mixed up from below. Vertical transport in the model is likely a little too high, leading to overestimated NCP and stronger outgassing in winter than reality. Erroneous results in the form of negative vertical surface fluxes means there is yet more to learn about and improve in the model before it is applied to evaluate carbon dynamics in this amount of detail. While the Argo data used was calibrated from the data assembly sensor, some sensor drift was not fully corrected for. This was reported to Argo Quality Control and is now corrected. The method employed is imperfect, but with further improvements it may become a valuable tool in carbon dynamics studies in the region. This requires continued Argo float deployments and ship-board measurements.

Contents

Chapter 1

Introduction

Until the industrial revolution, the global carbon cycle was in a steady state. Through the burning of fossil fuels such as coal, oil, and natural gas, as well as through land use change, human emissions have caused an excess of atmospheric CO_2 and an imbalance in the carbon cycle at a rate never before seen (*Zeebe*, 2012). The increased levels of atmospheric CO_2 drive climate change. However, as seen in Figure 1.1, not all emitted CO_2 remains in the atmosphere. In fact, around 26% of the anthropogenic carbon is taken up terrestrially, and 26% by the ocean (*Gruber et al.*, 2019; *Friedlingstein et al.*, 2022). To understand the future development of climate change, we must comprehend the mechanisms that govern these carbon sinks and their vulnerability to global warming. As one of two major carbon sinks, it is essential to know how much carbon the ocean can sequester now and in the future. This requires detailed knowledge of the drivers of the processes affecting oceanic carbon sequestration.
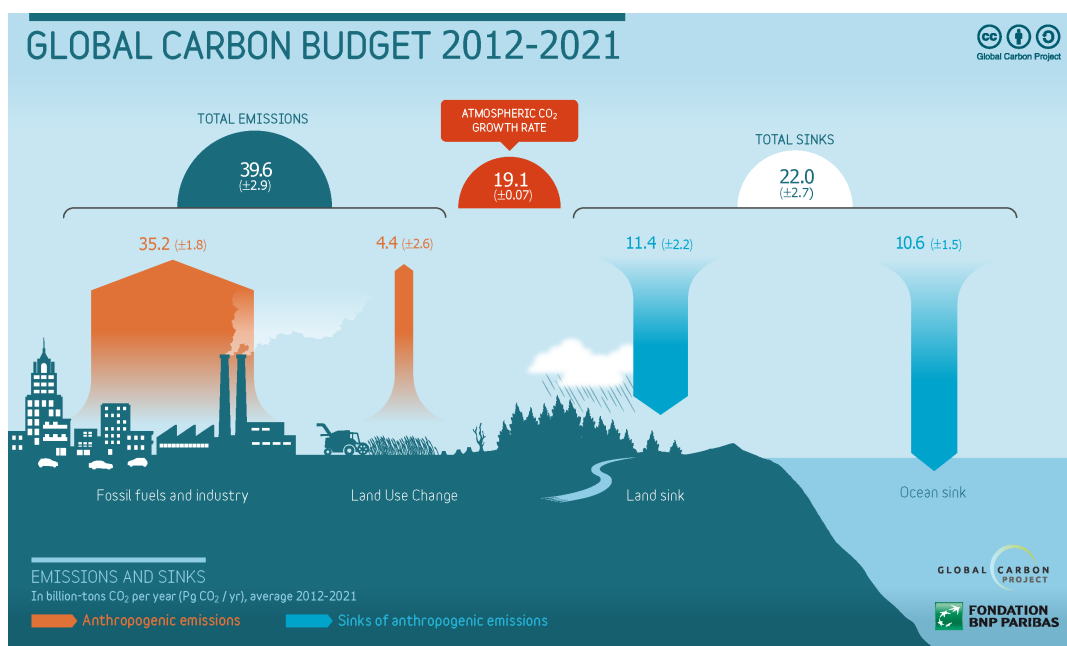

Figure 1.1: Carbon budget. Red arrows show anthropogenic emissions, blue arrows show uptake of anthropogenic emissions. Overarching half-circles indicate sums. Figure: Global Carbon Project. Data: the Global Carbon Budget 2022 (*Friedlingstein et al.*, 2022).

Ocean uptake of CO_2 is directly proportional to the difference in CO_2 content in the atmosphere and that of the surface water. These are often expressed in terms of the partial pressure of CO_2 in each phase ($p CO_2^{atm}$ and $p CO_2^{oc}$ respectively). $p CO_2^{atm}$ increases with increasing anthropogenic emissions. It is somewhat higher near major sources of emissions such as large cities. However, it is considered a well-mixed gas in the atmosphere, especially over the ocean, and as such is subject to considerably less variability than in the sea surface. Elucidating the drivers of $p CO_2^{oc}$ variability is therefore of greater interest.

When $p CO_2^{atm}$ is higher than $p CO_2^{oc}$, the ocean is undersaturated and uptake occurs. On a global scale, the ocean is undersaturated with respect to CO_2 by approximately 10 µatm. Hence, it is a net carbon sink (as shown in Figure 1.1). However, the saturation state of the world ocean is highly variable both in space and time. In fact, the global surface ocean is in some areas undersaturated with respect to atmospheric CO_2 by as much as 40%, and in other areas supersaturated by the same magnitude. Thus, despite the ocean being a net sink, there are also areas of outgassing (sources). Examples are the equatorial divergence zone, and the Baltic Sea. Regions of net uptake include the Southern Ocean and the Arctic Mediterranean.

$p CO_2^{oc}$ is governed by biological processes, the global ocean circulation, heat fluxes, wind, and air-sea gas exchange. Biological processes lead to a strong seasonal pattern in carbon uptake. Areas of intense biological production consume CO_2, causing undersaturation in spring and summer. As biological matter sinks through the water column, it is returned to its inorganic state, leading to high concentrations of carbon at depth. The global ocean circulation transports this inorganic carbon at depth to upwelling regions such as the aforementioned equatorial divergence zone. Here, cold, carbon-rich water masses from the deep ocean are transported to the surface. The water is heated by the strong thermal forcing in the area, reducing the solubility of CO_2 in water, and increasing $p CO_2^{oc}$. This leads to supersaturation and consequently outgassing. It is also the global circulation that drives the transport of warm surface water through the Arctic Mediterranean. Heat is lost to the atmosphere along its path. The consequence of this heat loss is two-fold: the CO_2 solubility as well as the water's density increase. This not only causes undersaturation, but is also an important mechanism for the vertical transport of carbon into the ocean interior, which is the overall bottleneck for ocean anthropogenic carbon uptake. Undersaturation is both the underlying requirement for carbon uptake, and a driver of its magnitude. Wind further enhances the air-sea gas exchange. Wind is also a key driver of the aforementioned vertical transport. Thus, there is an intricate interplay between the three main processes: biological processes, ocean circulation, and air-sea gas exchange. Ultimately, these drive $p CO_2^{oc}$ variability and in turn govern oceanic uptake of anthropogenic emissions. To understand the future role of the ocean as a carbon sink, it is vital to understand the dynamics between these three components, especially in sink regions.

The Greenland Sea is one of the few locations in which open-ocean convection occurs. In this region, wintertime mixed layer depths have regularly exceeded 500 m the last 10 years (*Brakstad et al.*, 2019). The deep mixing does not only transport carbon from the surface to the ocean interior, but also supplies dense, carbon-rich water to the overflows over the Greenland-Scotland Ridge. As such, the Greenland Sea represents a window of transport for carbon from the atmosphere into the lower limb of the thermohaline circulation. While the general hydrography (*Brakstad et al.*, 2019), carbon inventory (*Olsen et al.*, 2010), and carbon budget (*Jeansson et al.*, 2011) are well understood, the relative importance of vertical

transport, gas exchange, and biology in driving carbon uptake remains unclear. A 3-year study carried out by *Miller et al.* (1999) decomposed observed changes in dissolved inorganic carbon (DIC) to the theoretical contribution of air-sea gas exchange, biological processes, and vertical transport. They found that biology removed 70 ± 10 µmol C kg^{-1} from the surface in summer, leading to undersaturation on the order of 109 µatm. In winter, lower temperatures increased the ocean's uptake capacity by 50 µmol C kg^{-1}. However, due to deep winter convection, 80 µmol C kg^{-1} was mixed back to the surface, strongly inhibiting air-sea gas transfer. While certainly interesting results, the values obtained did not represent actual carbon fluxes, but rather a theoretical potential of DIC change. Additionally, the data consisted of measurements taken roughly every three months. Such sparse observations may not capture the full temporal variability. Other work in the area also cite a lack of wintertime data as a limiting factor in fully understanding the dynamics of the Greenland Sea (*Fransner et al.*, 2022).

New methods for data collection may help increase our knowledge of remote regions with harsh weather conditions. Autonomous sensors have become increasingly available. Instruments such as gliders and Argo floats take hydrographic measurements at frequent intervals and are capable of capturing full annual cycles and longer. These may also be equipped with biogeochemical sensors (*e.g.*, BGC-Argo), facilitating detailed studies of the carbon system. These have previously been utilised successfully in the investigation of net community production (NCP) in the Gulf of Alaska (*Plant et al.*, 2016), oxygenation of deep water in the Labrador Sea (*Wolf et al.*, 2018), and physical and biological drivers of BGC tracers in the Southern Ocean (*Briggs et al.*, 2018).

In terms of distinguishing between the physical and biological drivers of ocean carbon dynamics, it is necessary to apply more than high-frequency measurements through the annual cycle. One needs tools to actually quantify the strength of each driver. One approach is to determine the vertical transport and air-sea gas exchange through box models, as implemented in work such as *Anderson et al.* (2000). Box models decompose a system into several compartments (boxes) in which tracer concentrations are assumed homogeneous. For example, one might apply a box model separating the atmosphere, surface ocean, mid-depth ocean, and deep ocean into separate compartments, each with their own bulk tracer concentrations. Other processes such as biological activity and carbon system calculations may also be applied to each box. Transport between boxes is allowed through prescribed mixing rates. *Anderson et al.* (2000) applied a two-layered box model to determine carbon fluxes in the Greenland Sea. They estimated a gas exchange flux into the ocean of 53 ± 4 g C m^{-2} yr^{-1}, vertical transport of 11 g C m^{-2} yr^{-1}, and primary (new) production of 34 g C m^{-2} yr^{-1}. Although the resulting annual fluxes were comparable to other work at the time, this type of model cannot in sufficient detail describe the dynamics of the carbon system. In particular, their model resulted in very abrupt changes in time in the development of vertical carbon fluxes which do not reflect reality.

In recent years, biogeochemical dynamics have been explored using more sophisticated mixed layer models (*Plant et al.*, 2016; *Briggs et al.*, 2018). For this work, I follow *Plant et al.* (2016) and *Briggs et al.* (2018) in combining Argo data with a one-dimensional mixed layer model dubbed the Price-Weller-Pinkel model (PWP; (*Price et al.*, 1986)). This model is able to represent the development of the mixed layer, and thus vertical mixing, in much higher detail than the traditional box models. For cyclonic areas, where the assumption of horizontal homogeneity is (nearly) valid, it has been found to predict mixed layer depths with

success. While *Plant et al.* (2016) and *Briggs et al.* (2018) focus on the Gulf of Alaska and the Southern Ocean respectively, I apply the method to the Greenland Sea.

Earlier work on Greenland Sea hydrography has tuned the model to account for lateral advection of heat and salt (*Moore et al.*, 2015; *Brakstad et al.*, 2019). In this work, I further improve the model by adding BGC tracers and air-sea gas exchange parameterization with the aim of determining the drivers of pCO$_2$ variability. The total change in pCO$_2$ (ΔpCO$_2$) for a given period of time can be expressed as

$$\Delta p\mathrm{CO}_2 = \Delta p\mathrm{CO}_2^{\mathrm{GE}} + \Delta p\mathrm{CO}_2^{\mathrm{BIO}} + \Delta p\mathrm{CO}_2^{\mathrm{Fz}} \tag{1.1}$$

where $\Delta p\mathrm{CO}_2^{\mathrm{GE}}$ represents the change in pCO$_2$ due to air-sea gas exchange, $\Delta p\mathrm{CO}_2^{\mathrm{BIO}}$ the change due to biological processes, and $\Delta p\mathrm{CO}_2^{\mathrm{Fz}}$ the change caused by vertical transport. Through the model adjustments mentioned above, air-sea gas exchange and vertical transport of CO$_2$ are calculated directly by the model by way of DIC and Alkalinity. I reinitialize the model using every Argo profile, such that the model "drifts" in periods of approximately 5 days. The biological contribution to DIC variability is then estimated as the residual of model output and Argo profiles. This separation of biological and physical influences on carbon dynamics constitutes a valuable addition to our understanding of the carbon system in the region.

The overall aim of this thesis is to determine the drivers of pCO$_2$ variability. To reach this goal, I reach the following objectives:

- Add biogeochemical tracers and air-sea gas exchange of CO$_2$ and oxygen to the PWP model

- Add reinitialization scheme to the model

- Determine vertical transport of DIC and air-sea gas exchange fluxes using the model

- Estimate the contribution of biological processes to changes in DIC using DIC calculated from measurements from an Argo float and model output

- Evaluate how the carbon fluxes above affect pCO$_2$

Chapter 2

Background

2.1 Marine carbon chemistry

The distribution of carbon in the oceans is influenced by three main chemical processes, the major ocean circulation systems, and air-sea gas exchange. It is the latter that transports anthropogenic carbon from the atmosphere into the ocean. While nonreactive chemical components such as oxygen (O_2) equilibrate relatively quickly with the atmosphere, CO_2 entering the ocean through the atmosphere partakes in a series of chemical reactions. On average, 19/20 moles of gaseous CO_2 ($CO_{2(gas)}$) are buffered away by carbonate ions (CO_3^{2-}) and water (H_2O) to form bicarbonate (HCO_3^-) (*Sarmiento and Gruber*, 2006). Only the last 1/20 moles remain as CO_2 and carbonic acid (H_2CO_2), and contribute to increase the CO_2 partial pressure in the seawater. The equilibrium reactions may be expressed as follows:

$$CO_{2(gas)} + H_2O \overset{K_0}{\rightleftharpoons} H_2CO_3^* \tag{2.1}$$

$$H_2CO_3^* \overset{K_1}{\rightleftharpoons} H^+ + HCO_3^- \tag{2.2}$$

$$HCO_3^- \overset{K_2}{\rightleftharpoons} H^+ + CO_3^{2-} \tag{2.3}$$
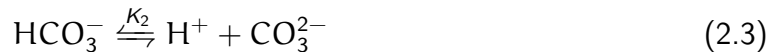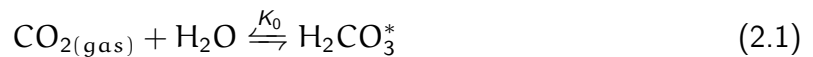
where $H_2CO_3^*$ denotes the sum of aqueous CO_2 and carbonic acid (H_2CO_3). K_0, K_1, and K_2 are the equilibrium constants of each reaction. Due to its complex behaviour, CO_2 takes a long time to equilibrate with the atmosphere.

Carbon does not only react with water in the process of dissolution. It is also one of the building blocks of life, participating in photosynthesis. In this reaction triggered by sunlight, CO_2, nitrate (NO_3^-), phosphate (HPO_4^{2-}), water and free protons form organic matter ($C_{106}H_{175}O_{42}N_{16}P$) and oxygen (*Anderson*, 1995):

$$106CO_2 + 16NO_3^- + HPO_4^{2-} + 78H_2O + 18H^+ \rightleftharpoons C_{106}H_{175}O_{42}N_{16}P + 150O_2 \tag{2.4}$$
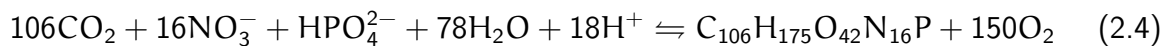
When working from right to left, organic matter is broken down by microorganisms in a process called remineralization. This returns the components to their inorganic forms.

C:N:P:O_2=106:16:1:-150 is the stoichiometric ratio of nutrient utilization and oxygen consumption in photosynthesis, called the Redfield ratio. This is a representation of the global mean composition of ocean phytoplankton. The molar ratios of nutrients contained in organic matter vary spatially and temporally depending on nutrient availability in a given region and the adaptations species have undergone. The Redfield ratio is a topic of continuous revision as other ratios are revealed on sub-global scales (*e.g. Takahashi et al.* (1993); *Frigstad et al.* (2014)). In fact, the cited ratio is itself a revision; the original Redifeld ratio had lower oxygen consumption (*Redfield et al.*, 1963). The Redfield ratio allows conversion of calculated biological production or remineralization based on one element to, *e.g.*, units of C, which is useful for determining the effects of biology on carbon sequestration.

The last major chemical reaction affecting the marine carbon system is the formation and dissolution of calcium carbonate ($CaCO_3$). This process occurs when certain types of plankton form calcite or aragonite shells, and subsequently when these shells break down:

$$Ca^{2+} + CO_3^{2-} \leftrightharpoons CaCO_3 \tag{2.5}$$

Thus, we have identified the three main chemical reaction systems governing the marine carbon system: dissolution of $CO_{2(gas)}$, photosynthesis (and respiration), and the formation (and dissolution) of biogenic calcium carbonate. They are dubbed the solubility pump, soft tissue pump and carbonate pump respectively.

There are challenges associated with measuring several of the individual components of the carbon system mentioned above. The easiest measurable properties are pCO_2, pH, dissolved inorganic carbon (DIC), and total alkalinity (Alk). pCO_2 is the partial pressure of CO_2 in water. pH = -log([H^+]) and as such is the measure of the concentration of free hydrogen in the water. From Equations (2.1) to (2.3), it is clear that this is closely related to the system of carbon dissolution reactions. DIC is the total concentration of the carbon atom in inorganic forms in seawater:

$$DIC = [H_2CO_3^*] + [HCO_3^-] + [CO_3^{2-}] \tag{2.6}$$

Finally, Alk is a measure of the balance between bases and acids present. As such, it tells us about the ocean's ability to buffer acids like CO_2. It is defined as

$$Alk = [HCO_3^-] + 2[CO_3^{2-}] + [OH^-] - [H^+] + [B(OH)_4^-] + \text{minor bases} \tag{2.7}$$

Here, [OH^-] is the concentration of hydroxide and [$B(OH)_4^-$] the concentration of borate. Both DIC and Alk are conservative properties with respect to changes of state (*i.e.*, temperature and pressure), and are therefore more suitable for model applications than pCO_2 and pH.

In total, the carbon system consists of 10 unknowns and 8 equations. Therefore, we can solve the system by specifying two of these unknowns. The most common variables to specify are pCO_2, pH, DIC and Alk because these are relatively easily measured. Figure 2.1 shows how the carbon invasion, photosynthesis, and calcifying processes affect Alk, DIC and CO_2 concentrations.

CO_2 invasion and release change DIC and the concentration of CO_2 as carbon atoms are added or removed from the seawater. Alk on the other hand, remains stable because the
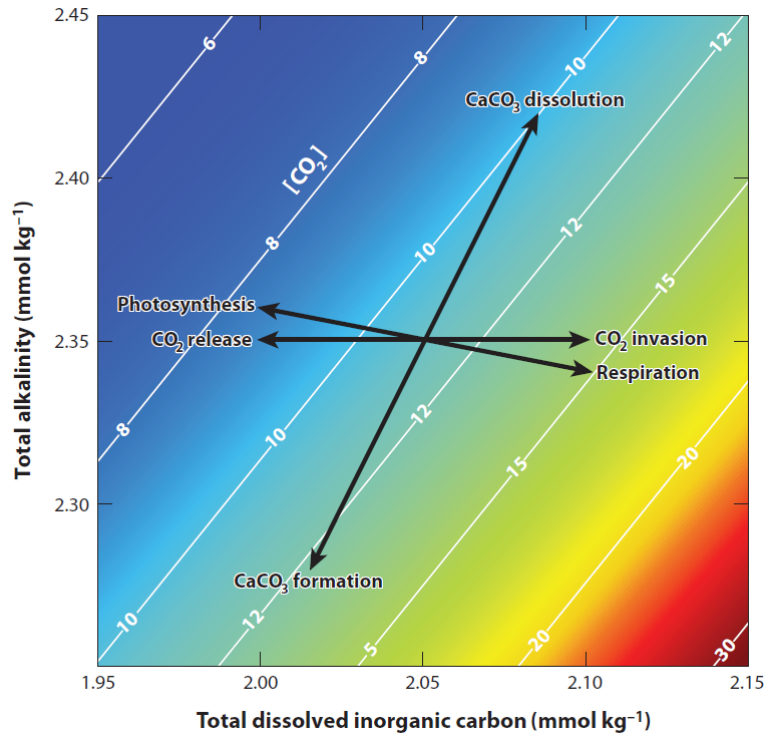
Figure 2.1: The effect of carbon invasion, photosynthesis, and calcifying processes on Alk, DIC and CO_2 concentrations. Alk and DIC are on the y and x axes respectively. CO_2 concentrations in µmol kg−1 are shown as white contour lines. Figure from *Zeebe* (2012)

pure addition or removal of CO_2 does not change the balance of ions. Photosynthesis consumes CO_2, reducing its concentration and thus also DIC. The consumption of nitrate during photosynthesis increases Alk as the total concentration of weak acids is reduced. This increase is not as big as the reduction in DIC so the net effect is a CO_2 reduction. The carbonate pump consumes carbonate ions during $CaCO_3$ production, causing DIC to decrease. In this process, DIC is reduced by one unit and Alk by two. This leads to an increase in CO_2. Due to buffering, the release is much lower than a 1:1 mole ratio. We therefore see a small increase in $[CO_2]$. The change in Alk is 2:1 because the carbonate ion contributes 2 moles for every 1 mole DIC.

Just as the three pumps affect the carbon system differently, they contribute to carbon sequestration in different ways. The soft tissue pump binds carbon into an organic form. Biological matter mainly from the euphotic zone is exported to deeper water through excrement and dead organisms. Most of this is remineralized within the upper 500 m of the water column (*Martin et al.*, 1987). Some of the export reaches the ocean floor where part is remineralized and part is buried in sediments. The process thus draws down carbon. Yet, a nearly equal amount is returned to the surface via vertical transport of remineralized inorganic carbon. This occurs via upwelling or via deep mixing. The soft tissue pump is therefore regarded as a steady-state background process in terms of long-term sequestration of carbon (*Sarmiento and Gruber*, 2006). It is, however, a main driver of seasonal pCO_2 signals in the surface ocean.

The carbonate pump also causes export of biological matter to the ocean interior. However, the weight of the organisms' aragonite and calcite shells cause a rapid descent, inhibiting

remineralization. This leads to higher sedimentation rates. Since the production of $CaCO_3$ at the surface releases CO_2, this process is also called the calcium carbonate counterpump. On geological timescales, $CaCO_3$ dissolves to release carbonate ions which are essential in removing the excess CO_2 in the ocean.

As mentioned in Chapter 1, the solubility pump causes CO_2 invasion if the partial pressure of CO_2 in the ocean is lower than that of the atmosphere, and evasion if $pCO_2^{oc} > pCO_2^{atm}$. The atmospheric CO_2 is absorbed in the surface and mixed into the surface layer. Since the biological pump (the sum of the soft tissue and carbonate pumps) is assumed to be a steady state process and is limited by the availability of nitrate, not CO_2, it is largely unaffected by changes in pCO_2. Ocean circulation and biology redistribute carbon within the ocean interior. Only air-sea gas exchange can change the carbon inventory of the ocean through uptake or release of CO_2. This is why it is essential to understand the mechanisms driving air-sea gas exchange.

2.1.1 Air-sea gas exchange

As briefly stated in the previous section, CO_2 uptake by the surface ocean depends on the difference in pCO_2 between the water and the atmosphere. For a nonreactive, slightly soluble gas, the flux (F) of gas across a liquid boundary layer is given by the following bulk equation

$$F = k(C^{atm} - C^{oc}) \tag{2.8}$$

where k is the gas transfer velocity (length time^{-1}), C^{oc} is the concentration of gas in the bulk liquid layer, C^{atm} is the concentration of gas at the water surface, i.e., in the atmosphere. The concentrations are given in mass volume^{-1} such that F has units in the form mass area^{-1} time^{-1}. In this equation, k represents kinetic forcing and the concentration difference is the thermodynamic forcing. The former is influenced by kinetic factors such as wind speed and boundary layer dynamics. The latter varies with sea surface temperature, transport and biology. For CO_2, the relation is often written in terms of partial pressure:

$$F = kK_0(pCO_2^{atm} - pCO_2^{oc}) \tag{2.9}$$

Here, K_0 is the solubility of CO_2 (mass volume^{-1} pressure^{-1}). pCO_2^{oc} and pCO_2^{atm} are the partial pressure of CO_2 in the water and atmospheric phases respectively, with units in pressure. While measurements of pCO_2 values are relatively easily obtainable and K_0 is estimated using polynomials, k must be parameterized. Most of the components influencing the boundary conditions contained in k are strongly influenced by wind. There is thus consensus in the scientific community that k is wind dependent however the best parameterization is yet to be concluded on. Suggestions range from linear to cubic dependencies (*Liss and Merlivat*, 1986; *Wanninkhof and McGillis*, 1999; *Wanninkhof et al.*, 2009), some with zero-intercepts and others claiming gas-exchange does not reach zero even for zero winds. Several studies do recommend a quadratic, zero-intercept relationship (*Sweeney et al.*, 2007; *Ho et al.*, 2006). A frequently used ^{14}C constrained quadratic parameterization following *Ho et al.* (2006) and *Sweeney et al.* (2007) has been optimized and recommended by *Wanninkhof* (2014):

$$k = 0.251\overline{U^2}\left(\frac{Sc}{660}\right)^{-0.5} \tag{2.10}$$

By convention, k is here expressed in cm h^{-1}. This is a simplification of the original units of cm^{3}cm^{-2}h^{-1}, meaning a unit volume (cm^3) of gas is transferred through a unit area (cm^2) per unit time (hour). $\overline{U^2}$ is the mean squared neutral wind speed at 10 m height (m^2 s^{-2}) and Sc is the non-dimensional Schmidt number of the gas in question. By normalizing Sc to that of CO_2 at 25°C (660), the expression is made applicable to other insoluble gases. 0.251 is the optimization factor calculated by *Wanninkhof* (2014). It has units of (cm h^{-1})(m s^{-1})$^{-2}$. ^{14}C constrained parameterizations of air-sea gas exchange take advantage of ^{14}C introduced to the atmosphere through thermonuclear bomb testing in the 1960s. Knowing the amount released to the atmosphere and the amount taken up by the ocean, global estimates of k are produced. Because of the wind dependence of k, the estimates vary depending on the global wind speed product used for calculations as these have different mean global wind speeds. This is why the correction coefficient is introduced. The above coefficient must be adjusted according to the applied wind speed product to take differences in global mean wind speed into account (*Naegler et al.*, 2006).

^{14}C constrained methods of parameterizing k for CO_2 have the advantage of including the effects of wave breaking without parameterizing these separately. At wind speeds higher than 15 m s^{-1}, however, the above relation is only applicable to CO_2. For less soluble gases such as oxygen, the effects of bubble-enhanced exchange must be taken into account (*Wanninkhof*, 2014; *Koelling et al.*, 2017). As for the parameterization of k, there are several methods for parameterizing the effect of bubbles. The effect is commonly treated additively. Early authors used the effect of partially dissolved bubbles (*Woolf*, 1997; *Woolf and Thorpe*, 1991), while later authors have focused on completely dissolved bubbles (*Vagle et al.*, 2010) or have applied both (*Stanley et al.*, 2009; *Liang et al.*, 2013).

Figure 2.2 shows climatological air-sea flux of CO_2, surface temperature, and nitrate concentrations. Positive values signify net oceanic uptake and negative values indicate outgassing. Note that while the climatology used for CO_2 flux is more recent than those of temperature and nitrate, the general patterns are comparable.
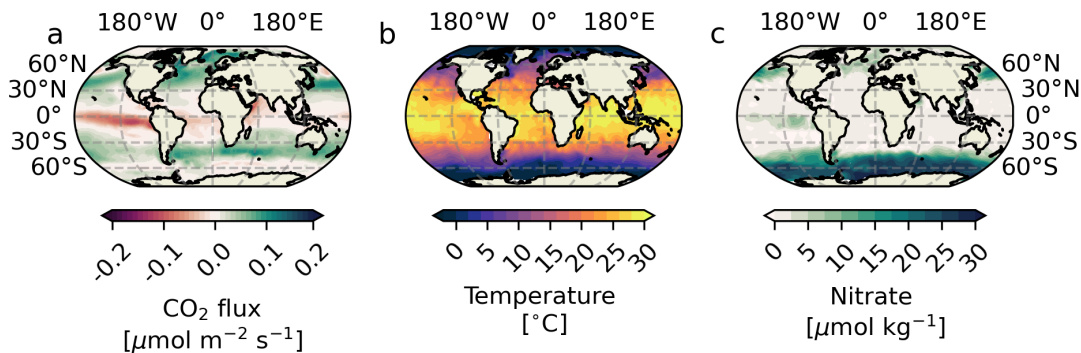
Figure 2.2: a) Global mapped climatology of CO_2 flux (1982-2021) (*Friedlingstein et al.*, 2022; *Landschützer et al.*, 2016). b,c) Global climatologies of surface temperature and nitrogen (1972-2013) (*Lauvset et al.*, 2016).

The dependence of air-sea gas exchange on temperature is apparent when comparing the pattern in Figure 2.2a to b. At low latitudes warm, DIC rich water surfaces. The high temperatures cause low solubility of CO_2 in water, causing outgassing. At high latitudes, water temperatures are colder and gas solubilities high. High-latitude areas also generally experience high wind speeds, further enhancing gas exchange. In large parts of the Southern

Ocean, ice cover blocks air-sea gas exchange in winter. Large amounts of unutilized nutrients (Figure 2.2c) indicate an unexploited potential for biological production which would reduce $f\mathrm{CO}_2$ (and $p\mathrm{CO}_2$) and drive air-sea gas transfer. In the Southern Ocean, there is also upwelling which brings carbon rich water to the surface. This leads to outgassing in some areas of the Southern Ocean. For optimal carbon uptake conditions, the kinetic and thermodynamical forcing must both be strong. These conditions favor areas of strong wind, low water temperature, and strong biological production.

Although large parts of the surface oceans have a net uptake of CO_2, very few regions have conditions allowing for vertical transport of the absorbed carbon into the interior ocean. For long-term storage of carbon deriving from gas exchange, deep mixing must occur. This is a process that requires strong surface heat loss spurring an instability in the water column which leads to mixing. Strong winds coinciding with such conditions enhance the mixing process, leading to mixed layers hundreds of meters deep. The conditions that lead to deep mixing also favour high rates of gas exchange as the cold temperatures of the water increase gas solubility in the water phase and the strong winds intensify the kinetic forcing. To date there are identified 4 areas of deep mixing where carbon uptake occurs: the Weddell Sea, the Labrador and Irminger Seas, and the Greenland Sea.

2.2 The Greenland Sea

The Greenland Sea (as seen in Figure 2.3) is a cyclonic gyre, its centre situated at approximately 0°E, 75°N. Warm Atlantic Water (AW) flows northward along its Eastern boundary, losing heat as cold, dry air from Greenland encounters the warm AW. A branch of AW enters the Arctic Ocean through the Fram Strait while a smaller part turns around to the Western boundary where it meets the fresh, cold polar water (PW) of the East Greenland Current (EGC). As AW is cooled through its path around the Norwegian Sea, it mixes with PW in the surface to produce Arctic Water. When this is cooled further and sinks, it produces very dense water, supplying the Denmark Strait Overflow Water with 39±2% of its water mass (*Brakstad et al.*, 2023). The water mass contributing to this overflow is the Greenland Sea Arctic Intermediate Water. It resides at 500-1000 m depth, but can reach depth of 1600 m (*Jeansson et al.*, 2017). Dense water from the Greenland Sea also constitutes 46±8% of the Faroe Bank Channel Overflow Water. Thus, the Greenland Sea is an important link connecting the Arctic Mediterranean to the subpolar North Atlantic and the rest of the meridional overturning circulation.
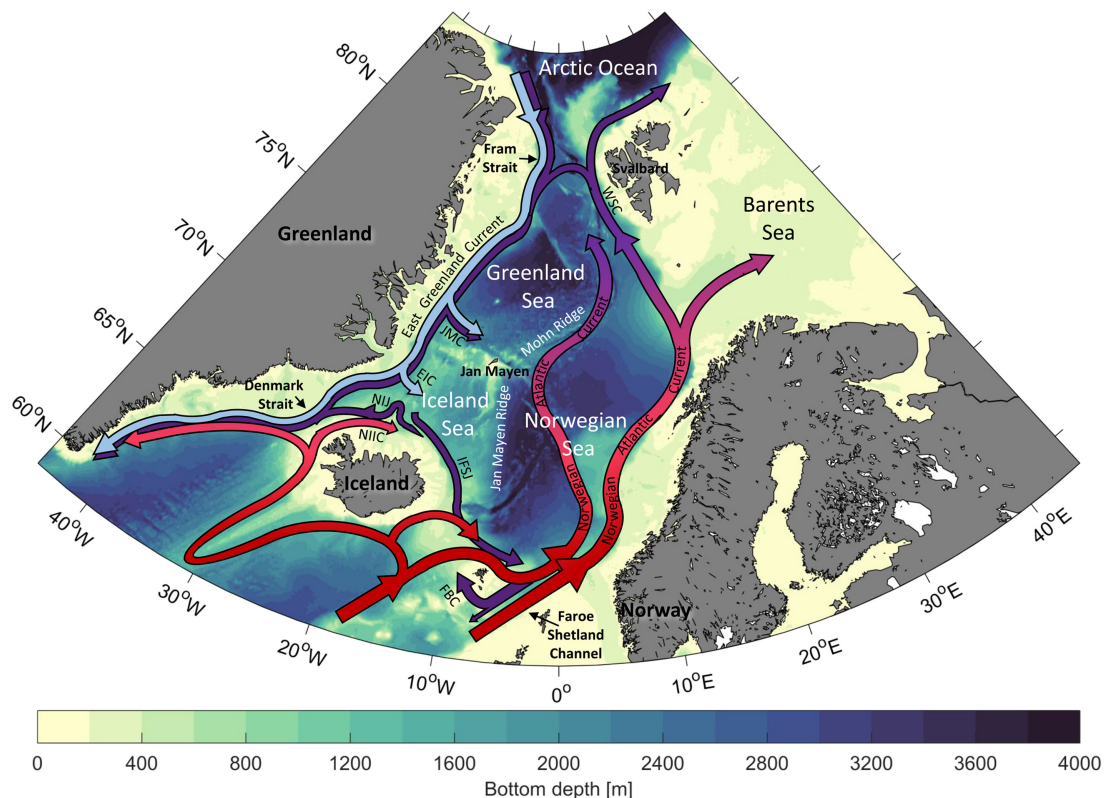
Figure 2.3: Map of the Nordic Seas. Red arrows indicate relatively warm, saline currents. Purple arrows indicate dense water, while light blue arrows are relatively fresh surface Polar Water pertaining to the East Greenland Current. Figure from *Brakstad et al.* (2023).

Figure 2.4 shows the vertical structure of hydrographic and biogeochemical variables in the Greenland Sea, gray-scaled by year of measurement. Surface temperatures in the Greenland Sea range between approximately -2 and 7°C. At depth, the temperature of the water masses is below zero. These cool temperatures contribute to the high density of *e.g.* the GSAIW. Since 1982, the water has become warmer at all depths. Surface water in recent years do not approach seawater freezing temperatures. The warming is evident in Figure 2.4a, and is

reported in literature (*Lauvset et al.*, 2018; *Brakstad et al.*, 2019).

Figure 2.4: Vertical profiles of temperature (a), practical salinity (S$_P$; b), dissolved oxygen (c), nitrate (d), pH (e), potential density anomaly (σ_θ; f), DIC (g), and Alk (h) from 1982 to 2019. The data points are gray-scaled by year of measurement. The updated GLODAPv2 dataset is used (*Lauvset et al.*, 2022).

Salinity is remarkably uniform in the Greenland Sea, as apparent from Figure 2.4b. The near homogeneous vertical salinity structure weakens stratification in the gyre. This is an important mechanism for preconditioning for winter convection, and is a characteristic of the region.

Because of the convective conditions in the Greenland Sea, the water masses are well ventilated. In recent years, convection has intensified after a period of winter mixed layer depths reaching maximum 300 m (*Lauvset et al.*, 2018; *Brakstad et al.*, 2019). Figure 2.4c therefore shows somewhat higher oxygen concentration from the surface to 2000 dbar for later years compared to the late 90's. Below 2000 dbar, this signal is reversed: there is a clear decreasing trend in oxygen from 1982 to 2019. This is due to a larger contribution from deep water in the Arctic Ocean (*Jeansson et al.*, 2023).

Nitrate is the limiting nutrient in the Greenland Sea and is therefore depleted at the surface in the productive season. Concentrations increase with depth due to remineralization.

Like major regions of the global oceans, the Greenland Sea also shows signs of acidification caused by the uptake of anthropogenic carbon. This has been documented in literature (*e.g. Fransner et al.* (2022)) and is also visible in Figure 2.4e. There is a clear decrease in pH with time throughout the water column.

Density in the Greenland Sea is governed by salinity, as evident from Figure 2.4f and b. While

fresh water and heat fluxes contribute to surface variability, density varies little from 500 dbar. Like the uniform salinity profile, this is testament to the weak stratification in the region. It is one of the enabling factors of deep convection.

Figure 2.4g shows an increase in DIC with time at all pressure levels, in agreement with the observed pH decline. The surface concentration is highly variable. This variability is due to biological production, surface dilution by precipitation, mixing from below, and air-sea gas exchange. This variability affects pCO_2, and ultimately the magnitude of carbon uptake in the region. It is therefore essential to evaluate the relative importance of each of the mentioned contributors to the surface DIC variability.

Alk is approximately linear in its relation to salinity. Its vertical structure is therefore very similar to that of S_P. At depth, Alk in the Greenland Sea generally lies around 2300 µmol kg^{-1} while surface concentrations are more variable due to freshwater dilution. As Alk, like S_P, consists of ions it is quite susceptible to the influence of freshwater which has a low ion content. Contrarily, polar water contains relatively high alkalinity because of river runoff rich in dissolved minerals. The reason DIC, which is also composed of ions, is not linear in its relation with salinity, is because it is strongly affected by biology and air-sea gas exchange.

Greenland Sea surface hydrographic and biogeochemical seasonal cycles are shown in Figure 2.5. Note that there are no measurements in the dataset for January, April, or October. There are also more data points for summer months compared to winter, leading to a summertime bias.

Temperatures are generally below zero in spring, reaching positive values in June. The range of values is greatest in summer. This could be due to interannual variations in heat fluxes, and because GLODAPv2 covers a large area which contains spatial variability. In the Greenland Sea, the East is influenced by relatiely warm AW, while in the East, the surface water has cooled and mixed with PW. For years with an anomolously cold spring, restratification would initiate later than usual. This could result in a shallow, warm, June mixed layer with colder water below. For such cases, the cold water would be within the pressure range 0-30 dbar and increase the range seen in Figure 2.5a.

Salinity is far more constant, with median values within the 34-35 span for all months measured. As for temperature, however, the range in surface values is larger in summer. This could be due to advected meltwater, interannual variability in precipitation patterns, and spatial variability. 1982-2016 is a period with very little sea ice in the region (*Brakstad et al.*, 2019). Local sea ice melt is therefore not likely to affect the surface salinity to a great extent, though advection of meltwater from the North may impact surface salinity.

Figure 2.5c shows that the lowest oxygen values are found in winter and fall, while summer concentrations are higher. While oxygen is produced by photosynthesis in the surface layer of spring and summer, the intense biological production also increases remineralization rates below. Winter mixing brings oxygen-poor water masses to the surface where they are re-oxygenated. Maximum oxygen medians do not coincide with the peak productive months as gleaned from nitrate and DIC. This is likely because warmer temperatures decrease solubility, counteracting the effect of photosynthesis.

Despite a lack of observations from February and December (in addition to the aforementioned
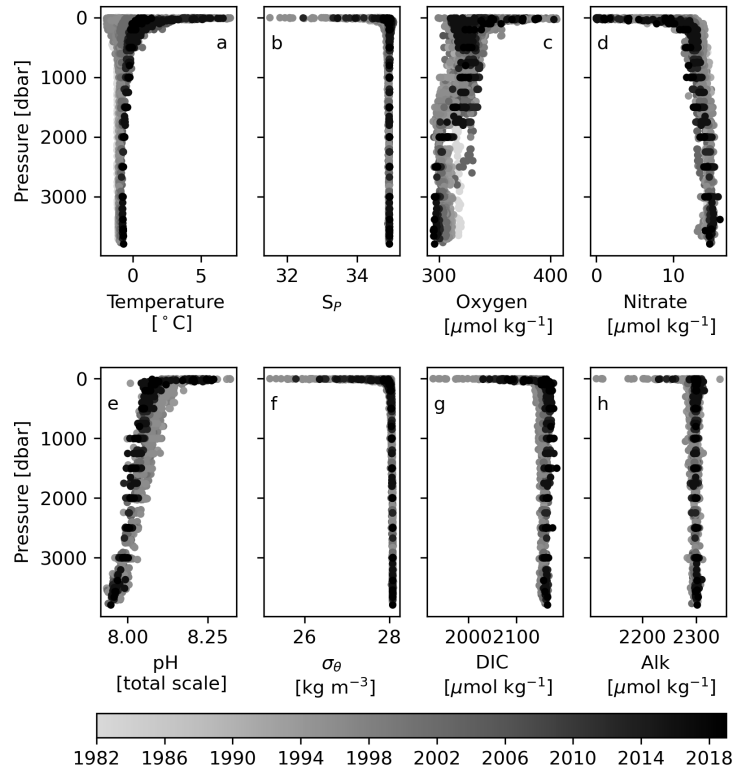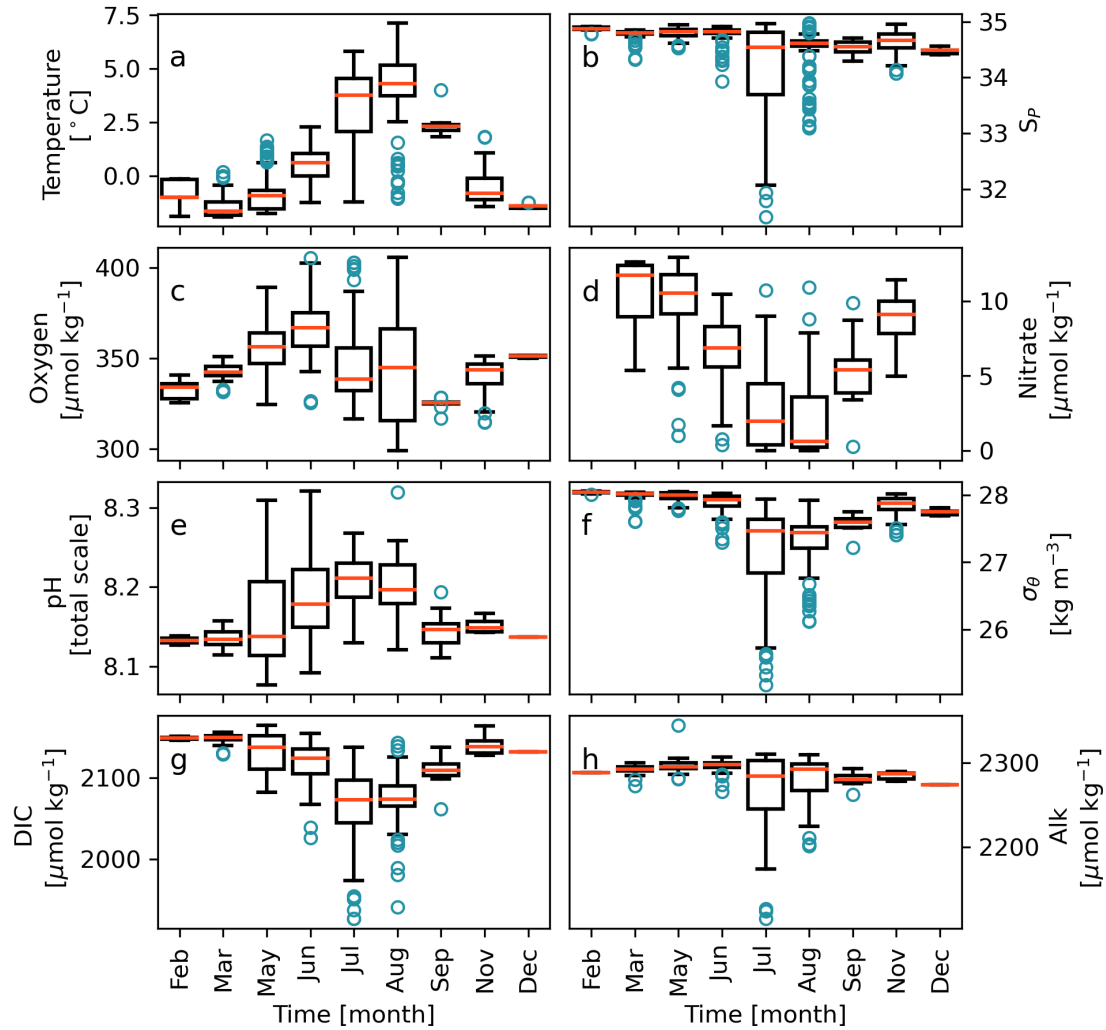
Figure 2.5: Box plot using data from 1982-2019 over 0-30 dbar of temperature (a), practical salinity (S_P; b), dissolved oxygen (c), nitrate (d), pH (e), potential density anomaly (σ_θ; f), DIC (g), and Alk (h). The boxes encompass the interquartile range (IQR) taken as the 1st to 3rd quantiles. The whiskers are 1.5×IQR. The red line shows the median, and the blue-edged circles are data points exceeding the whisker range. The updated GLODAPv2 dataset is used (*Lauvset et al.*, 2022).

data gaps in January, April, and October), the seasonality in nitrate in the Greenland Sea is evident. Concentrations tend towards zero in the productive season July-August. Some years feature abnormally low concentrations already in May and June, indicating earlier onset of phytoplankton blooms.

pH follows an inverse seasonal pattern compared to nitrate and DIC: maximum is reached in the peak production months of July and August. This is due to the consumption of DIC in this period, increasing the pH. As DIC is remineralized in autumn and winter, and air-sea gas exchange replenishes the mixed layer with DIC, pH falls.

As was also evident in Figure 2.4, density closely follows salinity variations. Variability is low, with mean values around 28 kg m^{-3} from February to June. Freshening and warming then result in somewhat lighter water masses and greater variability. In summer, values can reach

densities lower than 26 kg m^{-3}.

The development of DIC in the upper 30 dbar is similar to that of nitrate, as they are both consumed through photosynthesis, remineralized, and returned to the surface by winter mixing. DIC, however, is also affected by air-sea gas exchange which somewhat compensates the biological consumption.

Alk, like density and salinity, is relatively constant through the year. The range of concentrations measured increases in summer, coinciding with the freshening seen in salinity. As commented regarding Figure 2.4, this is due to the low ion content in freshwater.

As an important sink region with unique hydrogrpaphic and biogeochemical characteristics, it is important to monitor the development of the Greenland Sea oceanographic features. There has been a bias towards summer measurements due to challenging winter conditions. With new technology, this is evolving into a challenge of the past.

2.3 Argo floats as an observational method

The Argo program was launched in an effort to fill the data gap existing in areas where shipboard observations are scarce. It is also a more cost-effective observation method than scientific cruises. This allows for more measurements than would otherwise be obtained if ship-based observations was the only possibility of obtaining data. Since the first Argo float was put into the ocean in 1999, several thousand more have been deployed, dramatically increasing both the spatial and temporal resolution of observations in the global ocean. Today, there are 3857 operational floats in the global ocean (*Belbéoch et al.*).
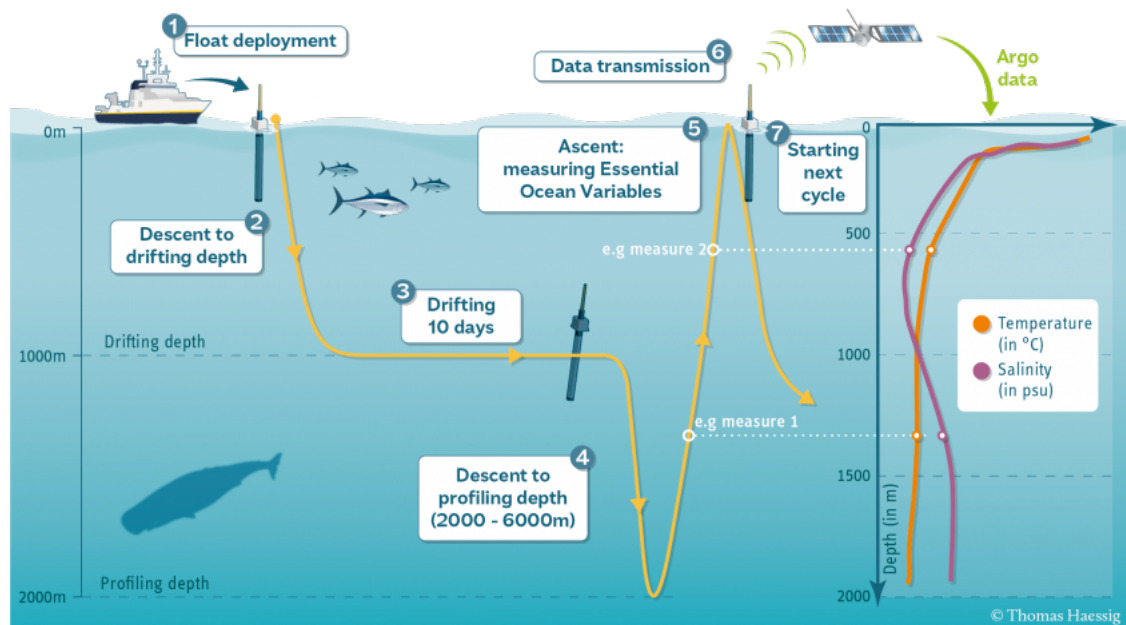

Figure 2.6: Illustration of the Argo float measurement cycle. Figure from Thomas Haessig (https://argo.ucsd.edu/how-do-floats-work/).

Argo floats are autonomous buoys, drifting with ocean currents. Their typical operational cycle is shown in Figure 2.6. The floats contain a bladder which enables them to sink to a "parking" depth, usually of 1000 dbar. They then drift at parking depth for 5-10 days before descending to a set initial profiling depth. Currently, this initial profiling depth is generally set to 2000 dbar due to limitiations in the pressure tolerance of the sensors. Floats specialized for deep profiles may descend to depths up to 6000 dbar. From the initial profiling depth, the floats ascend to the surface, simultaneously taking measurements. At the surface, the float transmits data to satellites before returning to parking depth and restarting its cycle. The data are then transmitted on to data centers where they are converted to human-readable data and quality checked in real-time. Adjusted data may be obtained as soon as 24 h after transmission from the float. However, in-depth quality control, so-called DMQC, requires months to a year to carry out. All data pertaining to the Argo program are freely obtainable online.

With the success of hydrographic observations from Argo floats, a program to add biogeo-chemical sensors was launched in 2016. In addition to traditional CTD observations, BGC-Argo floats measure one or more of the following properties: oxygen, pH, nitrate, irradiance, chlorophyll-α, and optical backscattering from suspended particles. The opportunity to measure these properties continuously in near real-time is a new revolution in the global data coverage. It is especially valuable at high latitudes which have been severely undersampled in the winter season. The Southern Ocean Carbon and Climate Observations and Modeling project (SOCCOM; https://soccom.princeton.edu/) has deployed around 264 floats in the Southern Ocean so far. Each float is able to measure at least two of the following: dissolved oxygen, nitrate, and pH. The success of the SOCCOM project has worked as a catalyst for further deployment of autonomous floats with BGC sensors in other regions.

Today, there are 75 active Argo floats at Northern high latitudes, 44 of which belong to the Norwegian NorArgo project. 7 of these are operative BGC-floats. In the Nordic Seas, the Norwegian NorArgo and NorArgo2 projects have been, and are, major drivers of Argo deployment. The projects are infrastructure projects funded by the Norwegian Research Council. The BGC-Argo infrastructure is a pioneering effort, the scientific results of which are still in their infancy.

2.4 The near-homogeneous mixed layer

The stratified nature of the world ocean is one of the basic features making it dynamic. In oceanography one often encounters the term "the mixed layer", referring to a surface layer that is so well-mixed that we can assume its properties to be homogeneous. This is not entirely true. Within the well-mixed surface layer there may still exist small variations in any of its properties. There may even be small surface inversions or smaller mixed layers within the defined mixed layer itself. This is possible because the definition of the mixed layer is highly subjective and the methods of calculation vary immensely. There appears to be no universal method to determine the mixed layer depth. Instead, several methods have been developed that all rely on there being *relatively* small variations in the properties of a water mass compared to a sharper gradient below, be it the pycnocline, thermocline or halocline.

Methods for mixed layer calculation range from simple threshold methods, through gradient

methods, to more complex methods applying line fits, second derivatives, and more. Threshold methods define the mixed layer depth as the point where the difference in temperature, salinity or density compared to the surface exceeds a given value. The surface reference value of the threshold methods is taken at depths between 0 and 10 m. Temperature thresholds in literature range between 0.1 to 1.0°C, while density thresholds between σ_θ=0.01 kg m^{-3} and σ_θ=0.125 kg m^{-3} have been applied (*De Boyer Montégut et al.*, 2004). Dynamic threshold methods also exist, where the threshold varies with the profile properties, for example:

$$\Delta\sigma_\theta = \sigma_\theta(T + \Delta T, S) - \sigma_\theta(T, S) \tag{2.11}$$

Gradient methods, as the word implies, take advantage of the often present strong gradient at the base of the mixed layer. A gradient threshold is then applied such that the point where, *e.g.*, a density gradient exceeds anything from 0.0005 to 0.05 kg m^{-4} is considered the mixed layer depth. For temperature gradients, 0.025°C m^{-1} is a commonly used value (*Holte and Talley*, 2009).

One of the more complex methods mentioned above, applying the second derivative, is the curvature method developed by *Lorbacher et al.* (2006). In this method, one searches for the first curvature maximum in temperature and density to define the mixed layer depth.

The consideration of mixed layer calculation methods is important because depending on the goal of a given study, different calculation methods may yield drastically different results. Determining the best method, however, is outside the scope of this work. In this application a method suitable for the Nordic Seas is employed.

Chapter 3

Data & Methods

To achieve the goal of elucidating CO_2 dynamics and the drivers of pCO_2 variability, I use a one-dimensional mixed layer model to calculate physical fluxes. To do this, I add BGC tracers and air-sea gas exchange of CO_2 and oxygen, and I reinitialize the model with output from an Argo float. I estimate the path taken by the Argo float between measurement points to facilitate interpolation of atmospheric forcing from external datasets onto the track, as hourly atmospheric forcing is required for the model. Fluxes of vertical transport and air-sea gas exchange are calculated from model output. The amount of drift in the model between each reinitialization is assumed to capture the major physical processes. Biology is then estimated by removing the changes caused by physics from the observations made by the Argo float. Biology is thus the residual of model and Argo output. Applying these methods, I am able to describe the annual cycle of the main drivers of DIC variability, and hence, pCO_2 variability. As far as the author is aware, this is the first time biogeochemistry is added to the PWP model tailored to the Greenland Sea.

3.1   Argo Biogeochemical profiling float

Initial profiles are required to run the PWP model, and to calculate biological fluxes. These were obtained from an autonomous profiling float. A PROVOR CTS4 Argo float with biogeochemical (BGC) sensors was deployed in the Greenland Sea by the Norwegian Institute of Marine Research (IMR) in May 2019. The float was active from May 31st 2019 to January 29th 2021. Its trajectory is shown in Figure 3.1.

Due to significant Southward drift, only the first 75 profiles were retained in this work. The remaining profiles cover slightly more than a full annual cycle: 31.05.2019-03.06.2020. Only data with a quality control flag of 1 were used. Corrected profiles labelled "_ADJUSTED" were used. These were downloaded from the GDAC 'Coriolis'. The float carried an SBE41CP Conductivity Temperature Depth (CTD) with accuracies for pressure, temperature and conductivity of 2.4 dbar, 0.002°C and 0.005 psu respectively. An Aanderaa Optode 4330 was utilised to measure dissolved oxygen at an accuracy of 30 μmol kg^{-1}, a SEAFET transistor measured total pH at an accuracy of 0.025, and nitrate was measured by SUNA_V2 spectrophotometer of 5 μmol kg^{-1} accuracy. The float also carried sensors to measure particle
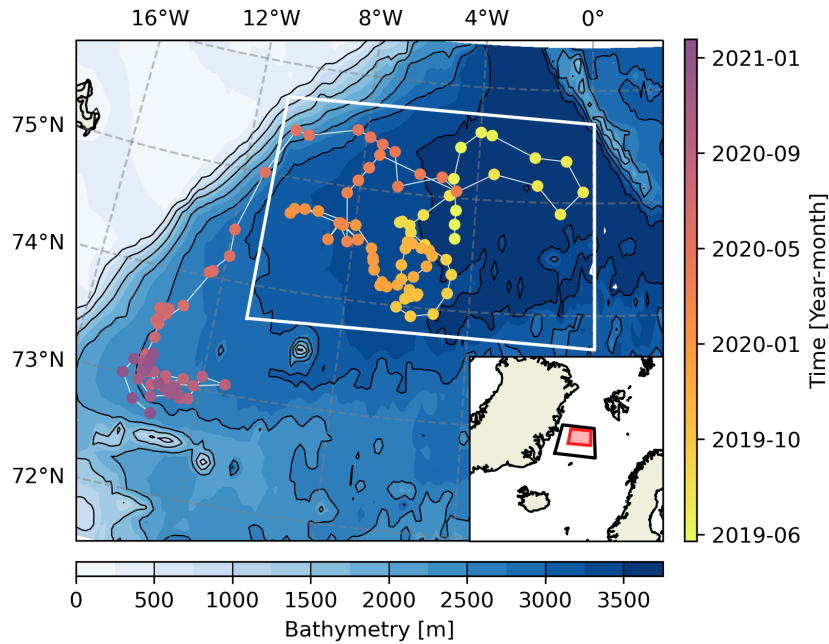
Figure 3.1: Colored circles show the float track from its deployment to end of life. The colorscale of the circles (vertical colorbar) show the date of measurement of each profile. Only the profiles within the white box are used. Bathymetry is indicated by shades of blue, with contour lines every 500 m (horizontal colorbar). The inset map shows the location of the mapped area (black box). The shaded, red box within corresponds to the white box in the main figure. Bathymetric data are from *GEBCO Bathymetric Compilation Group 2022* (2022)

backscattering and chlorophyll-α, but these malfunctioned after around 20 profiles.

Delayed mode quality control (DMQC) is carried out manually by qualified personnel. Properties are evaluated for trends and offsets. Piece-wise linear regression with change point alanysis is applied to trends, splitting a timeseries into sections where different corrections are applied. This ensures that correction is only applied where needed. Segments containing erroneous behavior could otherwise lead to correction of segments that were actually stable (*Wong et al.*, 2023). For temperature, no calibration was necessary. Calibration of salinity and nitrate take advantage of climatologies of deep measurements where variations in these properties should be small. Measured values are compared to those of the climatologies to uncover trends, offsets and discontinuities. In salinity, an offset was found an corrected for using a method by *Owens and Wong* (2009) which is the recommended technique (*Wong et al.*, 2023). The SAGE (SOCCOM Assessmentand Graphical Evaluatio) toolbox is used to calibrate nitrogen and oxygen. The World Ocean Atlas 2018 1800-1900 dbar was used as a reference dataset for nitrate (*Garcia et al.*, 2019). 5 sets of corrections in offset, and 4 in drift were applied by Kjell Arne Mork. New temperature corrections with subsequent updated DMQC for nitrate exist but were not applied due to time limitations (ref. personal correspondence with Kjell Arne Mork). The uncertainty estimate in nitrate was adjusted from 2 to 5 μmol following recommendations by Tanya Maurer as cited by Catherine Schmechtig in personal correspondence with Kjell Arne Mork. Oxygen calibration was carried out by Siv Kari Lauvset using atmospheric data as a reference, as recommended in "Quality Control Procedures for Oxygen and Other Biogeochemical Sensors on Floats and Gliders" (*Bittig et al.*, 2014; *Thierry and Bittig*, 2018). The oxygen sensor tends to drift towards lower values in

the surface, such that a positive drift correction of a few percent is applied. For this Argo float, this would have resulted in a strong positive trend in the deep. The trend was therefore not corrected, but all profiles were adjusted upwards by 6.4 %. pH reference data is calculated from a neural networks algorithm called CArbonate system and Nutrient concentration from hYdrological properties and Oxygen using a Neural-network, Bayesian approach (CANYON-B; (*Bittig et al.*, 2018). CANYON-B is trained using GLODAP data, and takes temperature, salinity and oxygen from the utilized Argo float as input to calculate the reference pH. The reference data was in the 1800-1900 dbar interval. A small offset and drift were corrected for. See *Maurer et al.* (2021) and the cited manuals for further details on calibration procedures.

A 2-D linear interpolation scheme applied to depth and time was used to remove data holes and to transfer the Argo data onto a 1 m vertical grid as required by the PWP model. A point in a given profile is not only dependent on the values directly above and below it. It is also the product of the previous profile and the changes it has been subjected to over 5 days. Likewise, the next profile is a result of this hypothetical given profile. Therefore, the value pertaining to a data gap within a profile is best approximated by interpolating in both time and space.

The Argo float typically measures the first value at 4-5 meters. Common practice is to extend this value to the surface (e.g. *Wolf et al.* (2018); *Codispoti et al.* (2013)). Profiles of alkalinity were calculated from salinity following according to *Nondal et al.* (2009), after which pCO_2^{oc} and DIC profiles were determined using alkalinity and pH as input in a marine carbon cycle solver called CO2SYS for Python (*Humphreys et al.*, 2022; *Lewis et al.*, 1998). See Section 3.3 for more details about the calculation of the marine carbon system.

Argo floats operate in cycles of typically 10 days. The Argo descends to a parking depth of approximately 1000 dbar where it remains for, in this case, 5 days. The short cycle of the float used in this work is unique. Before ascending, it dives down to 2000 dbar. Measurements are taken in ascent (*Carval et al.*, 2019). Hourly Argo float positions were calculated assuming constant, linear movement between each measured point. The float timestamps were rounded to the nearest hour. This led to 118-120 points between each known Argo coordinate, except for one instance of 47 points. The shorter time interval is the interval between the first two profiles. The first cycle is short because it is used to transmit technical data or configuration information.

3.2   External datasets

Atmospheric forcing drives the physics of the PWP model. Mean hourly values of surface net longwave radiation, surface net shortwave radiation, surface sensible heat flux, surface latent heat flux, total precipitation rate, evaporation rate, surface pressure, eastward wind speed at 10 m and northward wind speed at 10 m from the ECMWF Re-Analysis 5 (ERA5; (*Hersbach et al.*, 2018)) dataset. Note that ERA5 is known to have an Arctic warm bias (*Wang et al.*, 2019).

Dry mole fractions of CO_2 in the atmosphere, xCO_2, were obtained from the National Oceanic & Atmospheric Administration Global Monitoring Laboratory Carbon Cycle Greenhouse Gases

dataset (NOAA GML CCGG; (*Dlugokencky et al.*, 2021)). The dataset spanned three sine latitude steps (70.0-80.0°N) in the date range 01.05.2019-01.07.2020. CO_2 is considered meridionally homogeneous. The mole fractions were converted to pCO_2^{atm} using water vapor pressure (*Weiss and Price*, 1980) to account for air moisture as described by *Pierrot et al.* (2009). The ERA5 and NOAA data were interpolated in space and time onto the hourly Argo coordinates (see section above).

Chapter 2 and the comparison of Argo data to historical values in Chapter 4, rely on data from GLODAPv2 (*Key et al.*, 2015; *Lauvset et al.*, 2016, 2022). When used to describe the Greenland Sea, profiles within 73.9-75.7°N and 11-0°W are applied. The location of GLODAPv2 measurements are shown together with Argo profiling points in Figure 3.2.
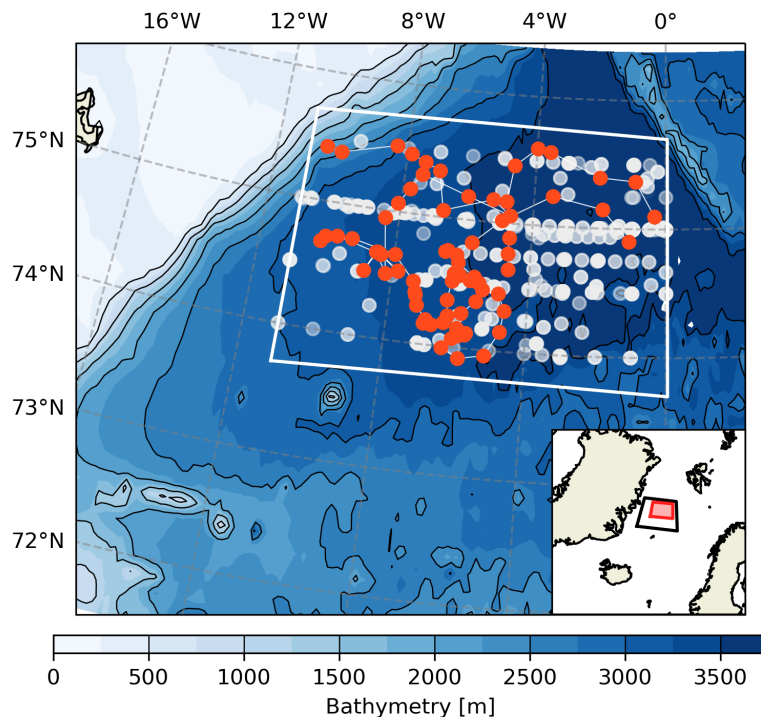
Figure 3.2: Map of the GLODAPv2 (white circles) and Argo stations (red circles) utilized. Bathymetry is indicated by shades of blue, with contour lines every 500 m (see colorbar). The opacity of the white circles indicate measurement density at a location (more opaque indicates more measurements; not quantified). The inset map shows the location of the mapped area (black box). The shaded, red box within corresponds to the white box in the main figure. GLODAPv2 data are from *Lauvset et al.* (2022). Bathymetric data are from *GEBCO Bathymetric Compilation Group 2022* (2022)

3.3 Calculation of marine carbonate system

Having obtained Alk from salinity, and pH from the Argo float, the rest of the marine carbon system is calculated using the marine carbon system solver CO2SYS developed by *Lewis et al.* (1998). For the initial profiles, a Python version is used (*Humphreys et al.*, 2022). As the PWP model is run in Matlab, a Matlab version of CO2SYS is used for calculation of pCO_2^{oc} within the PWP model. CO2SYS uses a pair of carbon properties as well as temperature,

salinity, and pressure to compute the components of the carbon system not used as input. There are various expressions for the dissociation constants involved in the carbon system's equilibrium reactions in literature. In CO2SYS it is possible to choose between some of these. Here, I apply the dissociation constants for carbonic acid, K_1 and K_2, of *Sulpis et al.* (2020), the sulfate dissocitation constants of Dickson *Dickson* (1990), fluoride dissociation constants of *Perez and Fraga* (1987), and borate dissociation constants by *Lee et al.* (2010). K_1 and K_2 from *Sulpis et al.* is appropriate for the cold conditions of the Greenland Sea. The same constants are used in the Matlab and the Python version. For simplicity, pH was not included in the model and is only used to calculate the DIC initial profiles. Within the model, $p\text{CO}_2^{oc}$ is calculated from DIC and Alk instead of pH and Alk. From CO2SYS it is also possible to calculate uncertainties of the output properties. This is described in Section 3.7.

C* is a conservative tracer used to exclude the effect of biological processes on DIC. It was calculated as

$$\text{C}* = \text{DIC} - 7.2[\text{NO}_3] - 0.5(\text{DIC} - [\text{NO}_3]) \tag{3.1}$$

where 7.2 is the C:N Redfield ratio of *Körtzinger et al.* (2001).

3.4 Mixed layer budget

The methods used to evaluate the influence of dynamics on $p\text{CO}_2^{oc}$ are built on a simple mixed layer budget as adapted from *Emerson and Stump* (2010):

$$\frac{\text{d}(\text{h}[\text{DIC}])}{\text{d}t} = \text{F}_\text{H} + \text{F}_\text{Z} + \text{F}_\text{E} + \text{F}_\text{mix} + \text{F}_\text{GE} + \text{B} \tag{3.2}$$

Here, the change in DIC in a mixed layer depth h with time (t) is the sum of horizontal advection (F_H), vertical transport (F_Z), entrainment and mixing from below during said vertical transport (F_E, F_mix), air-sea gas transport (F_GE), and biology (B). For the Greenland Sea gyre one can assume horizontal homogeneity as lateral advection is small compared to the other processes. We therefore neglect F_H. Observations from the Argo float contain all the processes affecting DIC. Removing the physical processes from the observations, biological processes remain. By adding BGC tracers and air-sea gas exchange of CO_2 and O_2, the physical terms in Equation (3.2) may be predicted using the PWP mixing model. The model is initialized at every Argo profile. The development in the model between each profile is then completely abiotic and only represents physical processes. Assuming the model captures these processes adequately, then the net community production (NCP_DIC) is the residual of modelled DIC and observed DIC as follows:

$$\text{NCP}_\text{DIC} = \text{DIC}_\text{obs}^{t=n_0} - \text{DIC}_\text{pred}^{t=n_1-1} \tag{3.3}$$

$\text{DIC}_\text{obs}^{t=n_0}$ is the DIC Argo profile at the time of a given reinitialization, $t=n_0$. $\text{DIC}_\text{pred}^{t=n_1-1}$ is the modelled DIC profile at the timestep immediately before a new profile, n_1, is reinitialized. The idea is that the changes between two Argo profiles in DIC not explained by physics (*i.e.* the model) is the biological component.

3.5 One-dimensional mixed layer model

The physical fluxes in the budget equation detailed above may be estimated by a one-dimensional mixed layer model. One such model that has proved applicable for gyres such as the Greenland Sea (*Moore et al.*, 2015; *Plant et al.*, 2016; *Brakstad et al.*, 2019) is the Price-Weller-Pinkel model (PWP; (*Price et al.*, 1986)). The original model uses initial profiles of temperature, salinity, and density. Heat and freshwater fluxes as well as wind forcing are applied at each timestep. Instabilities caused by these perturbations are evaluated at each timestep, leading to mixing if at least one of three stability criteria are met. The mixing results in a new, stable vertical structure. Several improvements have been made to the PWP model, and a Matlab version by *Glover et al.* (2011) is likely the base of the version I employ here. Further adjustments have been made to include lateral advection of heat (*Moore et al.*, 2015) and salt (*Brakstad et al.*, 2019) specifically tuned for the Greenland Sea. *Brakstad et al.* (2019) also added ice production following *Pickart et al.* (2016). For this work, I employ a Matlab version including the mentioned adjustments. I make the following further improvements:

- **Update the thermodynamic calculation package used from EOS-80 to Gibbs Seawater package TEOS-10.** TEOS-10 utilizes absolute salinity (S_A) and conservative temperature (CT) to calculate the properties such as density. EOS-80 used practical salinity and *in situ* temperature. As TEOS-10 is the new standard, it is now implemented.

- **Introduce biogeochemistry: Alk, nitrate, DIC, and oxygen**. This was necessary to be able to carry out the analysis.

- **Add dilution step for tracers.** The added BGC tracers are diluted when freshwater flux is applied. This must be accounted for. The effect is neglected for nitrate as it is considered very small.

- **Add air-sea gas exchange for CO_2 and oxygen.** This was necessary to be able to carry out the analysis.

- **Add profile reinitialization algorithm.** To be able to adequately capture the development of the DIC annual cycle, the model must be reinitialized for every Argo profile. This is key to calculating biology.

- **Change the mixing algorithm**. The bulk mixing algorithm did not take into account that concentrations are not additive. This is now changed.

- **Change the threshold for mixing in the first mixed layer deepening step**. Changing the mixing algorithm made the model somewhat more sensitive to atmospheric forcing. The stability threshold of the first mixing step is increased to compensate for this effect.

- **Parameterize advection of polar water tailored to the Argo float in use**. At the end of the annual cycle the Argo float was influenced by polar water. The model is not equipped to account for advection. A prescribed freshwater flux was implemented for the duration of 10 days to represent this advection.

The model is run with 1 hr timesteps, a vertical resolution of 1 dbar, and hourly atmospheric forcing. It is reinitialized at every Argo profile, i.e. approximately every 5th day. Table 3.1 shows an overview of the constants used in this model version. To analyse its performance, the model was also run once with no reinitalizations. This run using only one initial profile is referred to as the model running 'free'.

Table 3.1: Overview of the constants applied to the PWP model.

Constant	Value
Heat advection (yearly mean; *Brakstad et al.* (2019))	61.0 W m^{-2}
Salt advection (monthly mean; *Brakstad et al.* (2019))	-4.5 mm month^{-1}
Latent heat of fusion, L_n	300 000 J kg^{-1}
Specific heat capacity of seawater, c_p	4016 J kg^{-1} K^{-1}
Ice density, ρ_{ice}	920.0 kg m^{-3}
Reference density, ρ_0	1027.6 kg m^{-3}
Depth interval, dz	1 dbar
Size of timestep, dt	3600 s
Bulk Richardson number threshold	0.65
Gradient Richardson number threshold	0.25
Tuning coefficient, A_{ex} (*Plant et al.* (2016))	0.77
Tuning coefficient, A_p (*Plant et al.* (2016))	1.02
Tuning coefficient, A_c (*Plant et al.* (2016))	0.16

Figure 3.3 shows an overview of the main steps within the PWP model used in this work. The model is forced using atmospheric forcing data. Initial profiles of temperature, salt, oxygen, DIC, Alk, and pCO_2^{oc} are introduced to start the model. The added reinitialization algorithm introduces a new initial profile of each property every 5th day, *i.e.* when $t_{model} = t_{observed}$. Once the correct input data has been loaded, the model checks the surface box for freezing conditions. This leads to two separate paths through the loop: Case 1, where the surface temperature is higher than the freezing temperature, and Case 2 where the surface temperature is equal to or lower than freezing temperature. In the following I describe how these two cases progress within the model and which improvements I have made.

3.5.1 Case 1: No ice production

3.5.1.1 Applying heat and freshwater fluxes

If the temperature in the uppermost box is higher than the calculated freezing temperature, there is no ice production. In this case, the sum of sensible (Q_{sens}), latent (Q_{lat}) and longwave radiation heat (Q_{lw}) is added to the surface box. Next, freshwater flux, F_{FW}, is added to the same box as

$$S'_A = S_A(1 - F_{FW}) \tag{3.4}$$

where F_{FW} = (precipitation - evaporation), S_A' is salinity after dilution, and S_A denotes the
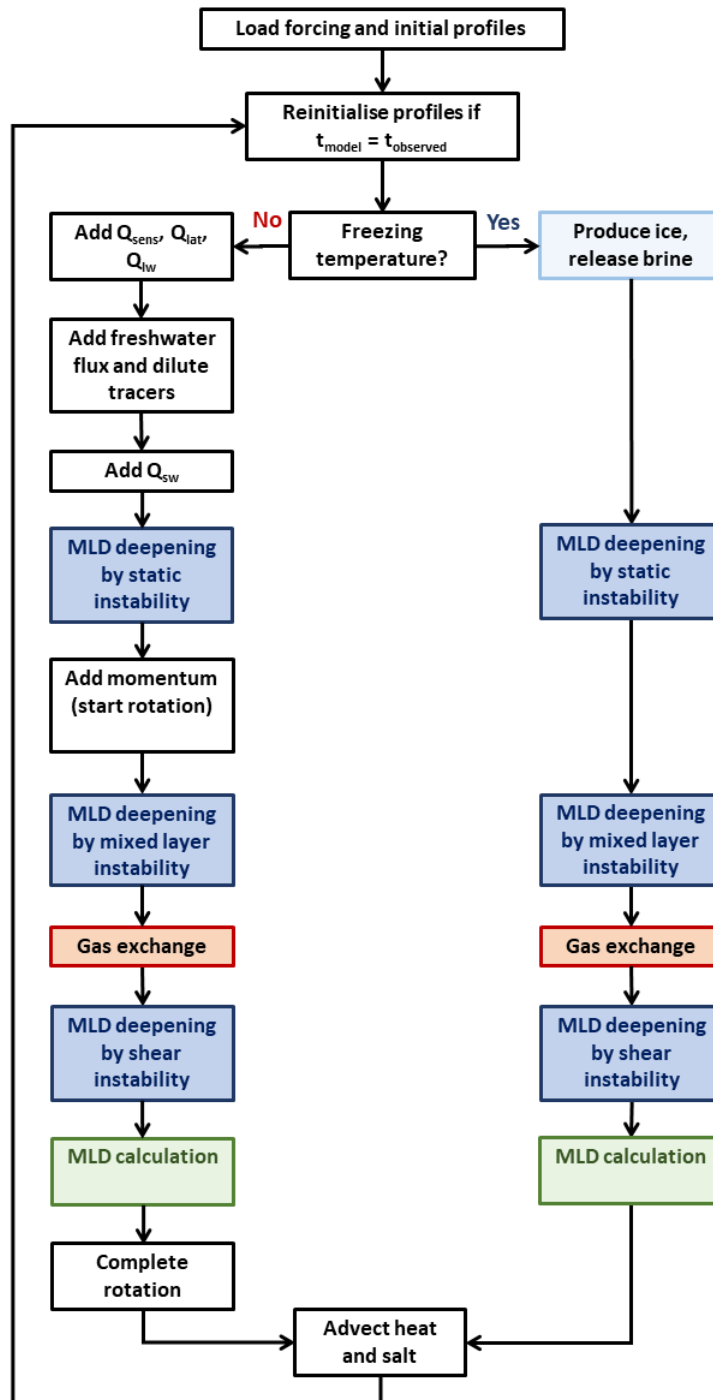
Figure 3.3: Flow chart illustrating the main steps of the PWP model utilized. Atmospheric forcing and initial profiles are loaded once. A routine checks if it is time to initialize with a new profile. The main loop starts by checking for freezing temperature. If $T>T_{freezing}$, heat fluxes and freshwater forcing are applied before mixed layer deepening commences. Wind-induced momentum is added, followed by air-sea gas exchange, a final mixing process, and final mixed layer calculation. More momentum is then added. Finally, heat and salt are advected, and the timestep is over. For freezing conditions, the first step entails ice production and brine rejection. Heat, freshwater fluxes, and momentum are ignored in this case. The remaining processes proceed in the same order as for non-freezing conditions.

original salinity of the surface box. The addition or removal of freshwater causes Alk and DIC concentrations to change. In reality, the nitrate concentration would also change however this effect is negligible due to the relatively low concentration of nitrate (<14 µmol kg^{-1}), and ignored. Here I add dilution of Alk simply by applying its linear relation to practical salinity, S_P (*Nondal et al.*, 2009):

$$\text{Alk} = 49.35 S_P + 582 \qquad (3.5)$$

This relation assumes little to no influence of polar water (PW) which is rich in minerals from river runoff and therefore would lead to a higher intercept (*Nondal et al.*, 2009). The use of this relation is a simplification compared to calculating dilution through a mass balance, but the results is the same. Assuming DIC accounts for the entire change in Alk, I calculate the new concentration of DIC (DIC') as

$$\text{DIC}' = \text{DIC} + \Delta\text{Alk} \qquad (3.6)$$

where ΔAlk is the total change in mass of Alk caused by dilution. The calculation involves converting the units from concentration to mass and back again. For simplicity, this is not shown.

The last step before adjusting the stability in the water column, is adding the shortwave heat flux (Q_{sw}). This is parameterized using the exponential radiation profile of the original model. In this radiation profile, approximately 50% of the shortwave radiation is absorbed in the uppermost meter of the water column whilst the rest is absorbed within the top 20 m. The original model was developed for application in the Pacific at 31°N where both hydrographic and biogeochemical conditions are very different to those in this work. However, it has been used successfully by *Brakstad et al.* (2019) in the Greenland Sea. I therefore leave it as used in their version.

3.5.1.2   Static instability: mixing by free convection

Having accounted for thermal and freshwater forcing, the first of three stability criteria is checked: static instability. The static instability criterion simulates free convection occurring due to thermal heat loss from the surface. Starting from the surface, each model vertical layer is evaluated according to

$$\frac{\partial \sigma}{\partial p} \geqslant 0 \qquad (3.7)$$

where σ is potential density and p is pressure. There is net precipitation during most of the studied annual cycle, which acts to decrease density and increase stratification. For static instability to occur, the heat loss must be strong enough to break through this stratification as heat loss densifies the water. In conditions where the effect of heat loss on density is stronger than that of freshwater, density at the surface will be higher than in some of the vertical layers below. This is the concept of static instability: due to gravity, a denser water parcel cannot lie on top of a less dense water parcel. The denser water mass will sink, mixing with the less dense water mass in the process. The static instability step thus checks each vertical layer from the top for conditions in which there is a density difference above

a certain threshold between the layer in question and the one below. This threshold was changed from 10^{-6} to $10\,10^{-5}$ kg m^{-3} to account for higher sensitivity introduced through a new mixing scheme (see Section 3.5.1.5 for details). To apply an actual threshold of 0 as in Equation (3.7) is inexpedient because all models exhibit some non-zero truncation errors which would lead to constant bottom-reaching convection. The new mixed layer depth is set as the first statically stable vertical layer. A bulk mixing scheme then mixes all tracers within the new mixed layer as detailed in Section 3.5.1.5.

3.5.1.3 Rotation and momentum

While the static instability deepening step is only dependent on heat loss, the two remaining deepening processes are wind driven. Wind forcing causes a transfer of momentum, which is subjected to the Coriolis force. The first step of calculating momentum in a given timestep is therefore to apply rotation. The angle α_{rot} of rotation is dependent on Coriolis (f) at the latitude of the first initial profile:

$$\alpha_{rot} = -0.5 f\, dt \tag{3.8}$$

The factor of 0.5 indicates that only half of the rotation is applied at this time. Rotation is finalized after the remaining deepening processes are run. A matrix of momentum (**UV**) in the water column is multiplied by a rotation matrix based on α_{rot} as follows:

$$\mathbf{UV}_{rot} = \mathbf{UV} \times \begin{bmatrix} \cos(\alpha_{rot}) & \sin(\alpha_{rot}) \\ -\sin(\alpha_{rot}) & \cos(\alpha_{rot}) \end{bmatrix} \tag{3.9}$$

Having completed the first half of the rotation process, X and Y momemtum is applied down to mixed layer depth. The mixed layer depth is taken as the depth calculated by the Nilsen method Section 3.5.1.8, not the depth to which mixing has actually occurred during the static instability deepening process. Ideally, the two depths should not differ greatly. The threshold for calculating mixed layer depth is more lenient in the Nilsen method than the static instability criterion, so mixed layer depth will be somewhat deeper using the Nilsen method. Momentum is added in the X-direction to calculate Ekman transport as

$$\mathbf{U}'_{[0:h]} = \mathbf{U}_{rot[0:h]} + \frac{dt\, \tau_{x[0:h]}(i)}{\rho_0 h} \tag{3.10}$$

Here, **U'**$_{[0:h]}$ denotes the new momentum in the X-direction in the mixed layer ([0:h]). **U**$_{rot[0:h]}$ indicates the rotated momentum of the mixed layer in the X-direction as calculated in the previous step. $\tau_{x[0:h]}(i)$ is the ERA5 wind stress at timestep i where the same value of τ_x is used at each depth of the mixed layer. ρ_0 is a reference density (see Table 3.1), and h is mixed layer depth. The same calculation is applied in the Y-direction, substituting τ_y for τ_x.

Finally, linear drag is applied to the whole water column as

$$\mathbf{UV}'' = \mathbf{UV}' - dt\, 0.05 f\, \mathbf{UV}' \tag{3.11}$$

where **UV"** is the final momentum matrix in this step (but not within the timestep) and **UV'** is the final momentum matrix after applying the previous equation to both X and Y directions.

3.5.1.4 Mixed layer instability: wind induced entrainment

The addition of momentum flux and rotation gives rise to differences in horizontal momentum between the mixed layer and the bulk fluid below, in addition to the preexisting difference in density between the two layers. These disparities cause instabilities evaluated by the Bulk Richardson number criterion, Ri_b:

$$Ri_b = \frac{g\Delta\sigma h}{\rho_0(\Delta\mathbf{UV})^2} \geqslant 0.65 \qquad (3.12)$$

Here, g is the gravitational acceleration, $\Delta\sigma$ is the difference between the density of two neighbouring depth levels, h is the mixed layer depth, ρ_0 is the reference density, and $\Delta\mathbf{UV}$ is the sum of the momentum difference between two neighbouring levels in the X and Y directions. $\Delta\mathbf{UV}$ is driven purely by wind stress. While the static instability criterion was evaluated from the surface down, the Ri_b criterion is assessed from the base of the mixed layer. For every box in which the criterion unfullfilled, the mixed layer is deepened by one box, and the mixing algorithm is run. The new Ri_b value is then calculated and the next box down evaluated. When $Ri_b \geqslant 0.65$, the entrainment process is ended and mixed layer stability is reached.

3.5.1.5 New mixing scheme

A mixing algorithm is applied at the end of the static instability deepening step, and at each deepening step during mixed layer instability deepening. In the model versions used by *Brakstad et al.* (2019); *Glover et al.* (2011), new mixed layer concentrations are simply taken as the mean of a given tracer over the new mixed layer depth. While computationally efficient, it does not represent the mixing process correctly. Firstly, a weighted mean should be used for any component undergoing mixing. Secondly, tracers given in terms of concentrations, *i.e.* mass of solute per unit mass of solvent, cannot be treated additively as is done when taking the mean. The tracers must first be converted to units of mass.

For a deepening of the mixed layer, tracers (c) in units of concentrations are now mixed as follows:

$$c'_{[0:h_1]} = \frac{\Sigma(c_{[0:h_0]}\rho_{[0:h_0]}V) + \Sigma(c_{[h_0:h_1]}\rho_{[h_0:h_1]}V)}{\rho_{[0:h_1]}Ah_1} \qquad (3.13)$$

h_0 and h_1 denote the old and new mixed layer depths respectively. A is the surface area considered, taken as 1 m^2. The mixed concentration c' is then the sum of the total mass of tracer c in the preexisting mixed layer and that in the volume added by deepening, converted back to units of concentration.

For shoaling of the mixed layer, the new concentration is simply the total mass of a tracer in the new mixed layer depth, distributed evenly through the mixed layer depth.

3.5.1.6 Air-sea gas exchange

Wind and heat fluxes strongly affect air-sea gas exchange. I therefore follow *Glover et al.* (2011) in implementing this process after the effects of wind and heat on the mixed layer

have been accounted for. Using a bulk formula the relation is

$$F_{CO_2} = k_{CO_2} K_{CO_2} (pCO_2^{atm} - pCO_2^{oc}) \tag{3.14}$$

where F_{CO_2} is the flux of CO_2 (positive when the transport is directed from the atmosphere into the ocean) in $\mu mol\ m^{-2}\ s^{-1}$. k_{CO_2} is the gas transfer velocity calculated for CO_2. K_{CO_2} is the solubility of CO_2 in seawater calculated using the polynomial and gravimetric constants proposed by *Weiss* (1974), and has units of $\mu mol\ \mu atm^{-1}\ m^{-3}$. pCO_2^{atm} and pCO_2^{oc} refer to the partial pressure of CO_2 in the air and water phase respectively. The partial pressures have units of μatm. pCO_2^{atm} is determined from atmospheric forcing input, while pCO_2^{oc} is calculated at each timestep from salinity derived alkalinity and DIC through the marine carbon chemistry solver CO2SYS as described in Section 3.3 (*Lewis et al.*, 1998). Parameterization of k is a much debated topic in the scientific community. I employ the quadratic dependence of k on wind speed suggested by *Ho et al.* (2006), as recommended by *Wanninkhof* (2014):

$$k_{CO_2} = 0.271 U_{10n}^2 \left(\frac{Sc_{CO_2}}{660} \right)^{-0.5} \tag{3.15}$$

0.271 is a coefficient accounting for the global wind speed product used (ERA5). Because of the quadratic dependence on wind, small differences in wind speed products amount to large inconsistencies in k. A correction coefficient is therefore required (see Section 2.1.1). Here, the coefficient is changed from 0.251 (*Sweeney et al.*, 2007) to the aforementioned value which is taken from *Fay et al.* (2021). The units of this coefficient are $(cm\ h^{-1})(m\ s^{-1})^{-2}$. U_{10n} is the second moment of the neutral wind speed at 10 m height, given in $m\ s^{-1}$. Sc_{CO_2} is the dimensionless Schmidt number. The Schmidt number is dependent on temperature, and is calculated at each timestep using a fourth order polynomial with constants calculated by *Wanninkhof* (2014). 660 is the Schmidt number of CO_2 at $20°C$.

For ^{14}C constrained estimates of k the effect of bubbles is already included. O_2, however, is less soluble. When applying a parameterization for k developed for CO_2 on O_2, we must add terms for partial bubble dissolution (F_p) and complete bubble dissolution (F_c) to the total flux equation separately:

$$F_{O_2} = F_{ex} + F_p + F_c \tag{3.16}$$

Each flux in the equation above has units of $\mu mol\ m^{-2}\ s^{-1}$. The diffusive flux, F_{ex}, of O_2 is parameterized using the difference between the saturation concentration of O_2 ($[O_2]_{sat}$; $\mu mol\ kg^{-1}$) and the *in situ* concentration ($[O_2]_{oc}$; $\mu mol\ kg^{-1}$) as the thermodynamic driver, multiplied by the gas transfer velocity (k_{O_2}; $cm\ h^{-1}$) and a dimensionless tuning parameter A_{ex}:

$$F_{ex} = A_{ex} k_{O_2} ([O_2]_{sat} - [O_2]_{oc}) \tag{3.17}$$

where

$$k_{O_2} = k_{CO_2} \left(\frac{Sc_{O_2}}{660} \right)^{-0.5} \tag{3.18}$$

Thus, the gas transfer velocity for O_2 is a product of the gas transfer velocity of CO_2 and the normalized Sc for O_2, Sc_{O_2}. Sc_{O_2} was calculated using constants from *Wanninkhof* (2014). $[O_2]_{sat}$ in Equation (3.17) is calculated using the TEOS-10 toolbox (*IOC et al.*, 2010) which applies solubility coefficients from *Benson and Krause* (1984) fitted by (*Garcia and Gordon*, 1992, 1993).

To account for the effect of wave breaking at high wind speeds, I use the bubble dissolution terms from *Stanley et al.* (2009) as applied by *Plant et al.* (2016), yielding

$$F_p = A_p 2.3 \times 10^{-3} (U_{10n} - 2.27)^3 \alpha \left(\frac{D}{D_0}\right)^{\frac{2}{3}} \frac{P_b - P_{oc}}{RT} \tag{3.19}$$

$$F_c = A_c 9.1 \times 10^{-11} (U_{10n} - 2.27)^3 \frac{P_a}{RT} \tag{3.20}$$

A_{ex}, A_p, and A_c in Equations (3.17), (3.19) and (3.20) are tuneable parameters set to 0.77, 1.02, and 0.16 respectively, as calculated by *Plant et al.* (2016). These adjust the relative importance of F_{ex}, F_p, and F_c. They tend to be optimized using cost functions. The values used here are optimized for the Ocean Station Papa in the Gulf of Alaska. Tuning these parameters for the Greenland Sea is outside the scope of this work but should be considered in future endeavours. *Plant et al.* (2016) use the optimization results of *Stanley et al.* (2009) as a baseline for their tuning. The constants 2.3×10^{-3} and 9.1×10^{-11} are the coefficients determined by *Stanley et al.* (2009). A_{ex}, A_p, and A_c are then the tuning parameters applied by *Plant et al.* (2016) in addition to Stanley's coefficients. α in Equation (3.19) is the dimensionless Bunsen coefficient of solubility (*Weiss*, 1970). D is the diffusion coefficient of O_2 (*Hayduk and Laudie*, 1974) for which the viscosity of seawater is required and is calculated according to *Qasem et al.* (2021), citing *Sharqawy et al.* (2012b,a). D_0 is a normalisation factor inserted by *Plant et al.* (2016) to simplify units. P_a and P_b are the partial pressures of O_2 in air bubbles. P_{oc} refers to oxygen's partial pressure pO_2 in seawater. The calculation of these pressure terms follows *Stanley et al.* (2009). R is the gas constant (8.31 m^3 Pa mol^{-1} K^{-1}) and T is the temperature in Kelvin. At wind speeds (U_{10n}) below 2.27 m s^{-1}, the effect of bubbles is negligible and F_c and F_p are set to zero.

Previous work in the Labrador Sea (*Koelling et al.*, 2017) has shown relatively small uncertainties applying the bubble parameterization of *Stanley et al.* (2009). As the Labrador and Greenland Seas have similar weather conditions the parameterization is expected to be applicable to the latter as well. Determining the best air-sea gas exchange parameterization method is outside the scope of this thesis but may be worthwhile investigating in future endeavours.

Once the air-sea fluxes of carbon and oxygen are calculated (F_C), they are converted to an hourly timescale and the mass of gas absorbed into the water phase is evenly distributed through the current mixed layer as follows

$$[C]_{[0:h]}^{GE} = [C]_{[0:h]} + \frac{F_C dt}{\rho_{[0:h]} h} \tag{3.21}$$

The new concentration of gas in the mixed layer, $[C]_{[0:h]}^{GE}$, as well as the concentration before gas exchange, are in units of μmol kg^{-1} h^{-1}. dt is the model timestep, in this case set to 1 hr. $\rho_{[0:h]}$ denotes the *in situ* densities of the mixed layer, and h is mixed layer depth. A water parcel within the mixed layer is circulated through the mixed layer water column such that a parcel at the base of the mixed layer will be transported to the surface and *vice versa*. Using the above equation I assume that every parcel within the mixed layer is in contact with the surface and is subjected to the same amount of gas flux, or at the least that the gas injected at the surface is subjected to so much mixing that its final distribution within the timestep is homogeneous. This is a normal simplification, made by *e.g. Glover et al.* (2011).

3.5.1.7 Shear flow stability: wind induced smoothing

The previous mixing step employing Ri_b leads to an unnaturally sharp gradient at the base of the mixed layer. In reality, the transition is much smoother. To account for this, *Price et al.* (1986) added the third and last stability criterion: shear flow stability expressed through the gradient Richardson number, Ri_g. Shear flow stability is attained when

$$Ri_g = \frac{\frac{g\partial\sigma}{\partial p}}{\rho_0\left(\frac{\partial\mathbf{UV}}{\partial p}\right)^2} \geqslant 0.25 \tag{3.22}$$

As evident from the term $\partial\mathbf{UV}$, this too is a wind-induced mixing process. Unlike the mixed layer instability step, however, the whole mixed layer is never mixed. Here, the model searches the stratified depths at the mixed layer base for cells in which $Ri_g \leqslant 0.25$. These are then partially mixed according to

$$c'_j = c_j - \left(1 - \frac{Ri_g}{0.3}\right)\frac{c_j - c_{j+1}}{2} \tag{3.23}$$

$$c'_{j+1} = c_{j+1} + \left(1 - \frac{Ri_g}{0.3}\right)\frac{c_j - c_{j+1}}{2} \tag{3.24}$$

where c is a given tracer and c' is its partially mixed product. j and $j+1$ are two neighbouring vertical layers subjected to stirring. 0.3 is a constant set by *Price et al.* (1986) in their original paper used to accelerate convergence. Upon completion of the stirring process, Ri_g is recalculated and the process is repeated until the stability criterion is reached for the stratified section of the profile.

3.5.1.8 Calculation of final mixed layer depth

The mixed layer has now been altered due to heat loss, entrainment and shear instability. The final mixed layer depth is calculated as the depth where (*Nilsen and Falck*, 2006)

$$\Delta\sigma_\theta = \sigma_\theta(T_0 - \Delta T, S_0) - \sigma_\theta(T_0, S_0) \tag{3.25}$$

σ_θ is potential density (kg m^{-3}). T_0 (°C) and S_0 are the surface temperature and salinity respectively. ΔT is an arbitrary value, found to work well at $\Delta T = 0.2$ °C in the Iceland and Greenland Seas (*Våge et al.*, 2015; *Brakstad et al.*, 2019). Note that this is different from the original value of $\Delta T = 0.8$ °C fit to the more stratified Norwegian Sea (*Brakstad et al.*, 2019). Both *Nilsen and Falck* (2006), and *Brakstad et al.* (2019) use a varying $\Delta\sigma_\theta$ to account for seasonal changes in stratification. This is not applied here due to time limitations. Further work may include consideration of a seasonal $\Delta\sigma_\theta$.

Other methods for mixed layer depth calculation were also tested (*e.g.*(*Lorbacher et al.*, 2006)) however the Nilsen method yielded the best match between model and Argo mixed layer depths when applied to both.

Note that there is no mixing in this final calculation of mixed layer depth. It only represents the depth to which the bulk fluid is *relatively* homogeneous, and is not necessarily the depth to which an exchange of mass or volume has occurred. The calculated mixed layer depth is still useful to calculate in this way, as it is an important metric to assess if the model can accurately predict vertical transport.

After mixed layer calculation, rotation of momentum is completed as per Equation (3.9).

3.5.1.9 Advection

The last steps of the loop are advection of heat and salt. Heat advection in the model follows the approach as *Moore et al.* (2015), using the updated constants calculated by *Brakstad et al.* (2019). They assume a continuous yearly heat loss (61 W m^{-2} y^{-1}) from the surrounding water to the Greenland Sea gyre. This heat is transported into a 1000 m deep water column, which is a typical wintertime mixed layer depth in the region. At each timestep, a fixed amount of the total yearly advected heat is added to the modelled temperature profile. The heat is distributed vertically to reflect the temperature difference between the gyre's interior and the adjacent water masses. This means most of the heat is added at depths corresponding to the exterior mixed layer depth (considered to be half the depth of the mixed layer within the gyre, i.e., 500 m), with an exponential decrease towards the gyre mixed layer depth of 1000 m. Similarly, a constant freshwater removal from the gyre is applied. In this case, salt is removed in the upper half of the gyre's mixed layer to simulate input of relatively fresh polar surface water. Below, the exterior water masses are more saline, leading to an injection of salt in the lower part of the gyre's mixed layer.

The advection in the model refers to transport of water masses from outside the Greenland Sea gyre required to close climatological heat and salt budgets. Horizontal homogeneity is assumed within the gyre such that local lateral advection is neglected.

In addition to local lateral advection, diffusion is neglected. In some versions of the PWP model (e.g.(*Glover et al.*, 2011; *Plant et al.*, 2016; *Briggs et al.*, 2018)), there are three tuneable parameters: heat offset, freshwater offset and the diffusion coefficient K_z. The two former are covered by parameterizations of heat and salt advection, which leaves only K_z as a tuneable parameter for the physics of the model (excluding gas exchange). I follow *Brakstad et al.* (2019) in neglecting diffusion.

Preliminary results showed excessively deep mixed layer depths after profiles 57 and 58 compared to observed mixed layer depths. Examination of the profiles showed that the anomalies could not be attributed to the float's coordinates at the times in question, nor to ice production or ice melt. Inspection of the model forcing revealed reasonable heat loss and precipitation patterns within the timeframe. The observed profiles feature a freshening and cooling of the surface to approximately 8 m and 108 m for profiles 57 and 58 respectively. Since the changes cannot be attributed to increased precipitation, the cause must be advection of polar water.

To account for this, the surface salt difference between profiles 57 and 58 (-0.0239) is added at each timestep until reinitialization. Diluting the tracers at each timestep results in excessively low DIC concentrations and a correspondingly strong gas transfer. To avoid this effect, tracers

are only diluted at the first timestep after initialization of profile 57. I apply the Alk:S relation for polar water rather than Atlantic water here (*Nondal et al.*, 2009).

The salt difference between the next two profiles is significantly higher: 0.0663. Adding the full amount of each timestep yields unreasonably fresh water. Applying half the amount is sufficient. Tracer dilution is parameterized as for profiles 57-58.

Once advection has been applied, the loop restarts.

3.5.2 Case 2: Ice production

In Case 1, wind stress and atmospheric heat fluxes penetrate the surface water. Ice production on the other hand, shields the surface water. Assuming an ice cover of 100%, these forces are neglected. If the surface holds freezing temperature, sea ice is produced and brine is released. The sea ice production rate, P (UNITS), is estimated as (*Pickart et al.*, 2016):

$$P = \frac{Q_{net}}{\rho_{ice}L_n} \tag{3.26}$$

where Q_{net} is the net surface heat loss, ρ_{ice} is the density of sea ice (920 kg m^{-3}), and L_n is the latent heat of fusion (300 kJ kg^{-1}). The effect of thickening ice on ice growth rate is not accounted for. Instead, polynya-like conditions are assumed which immediately transport newly formed ice out of the model domain (*Brakstad et al.*, 2019).

The salt flux F_s resulting from brine release is calculated according to

$$F_s = \rho_{ice}P(S_{sw} - S_{ice}) \tag{3.27}$$

$$S_{ice} = 0.31S_{sw} \tag{3.28}$$

in which S_{sw} and S_{ice} are sea surface salinity and sea ice salinity respectively. The relation of the latter is paramterized following (*Martin and Kauffman*, 1981). As salt essentially is a conglomerate of various ions, brine rejection affects the alkalinity and DIC concentrations. Alkalinity is recalculated in the surface box to account for this (*Nondal et al.*, 2009). As for the effect of freshwater flux described previously, I treat the change in DIC as $\Delta DIC = \Delta Alk$.

At each timestep of ice production, the released salt is added to the upper grid and mixed down until the static stability and Ri_b criteria are met. Gas exchange is then estimated.

In terms of heat and freshwater fluxes, we assume an immediate ice cover of 100% as soon as ice starts forming. This should also lead to a complete block of air-sea gas exchange. Preliminary results and ERA5 ice concentrations however, showed minimal ice production for the 2019/2020 season. Such conditions would likely involve large cracks and dynamics allowing most of the surface water open to air-sea interaction. The brine release from such a small modelled ice production is not enough to impact the physics of the model. I therefore assume 100% gas exchange even for timesteps in which ice production occurs. The effect of this decision is explored in Section 5.1.2.

Following gas exchange, Case 2 proceeds as Case 1, with the exception that there is no rotation step because it is assumed that wind forcing is blocked by the ice.

3.5.3   Sum of changes

In summary, I have added Alk, nitrate, DIC, and oxygen as tracers, and the dilution of these in response to freshwater fluxes. I have added air-sea gas exchange for CO_2 and oxygen, and code to reinitialize the model with every Argo profile. To account compensate for advection of polar water that the model is unable to capture as-is, I have added a parameterization of freshwater flux and subsequent tracer dilution at relevant timesteps. I have also made amendments to existing content within the model. I updated the thermodynamic calculation package used from EOS-80 to the state-of-the-art TEOS-10 Gibbs Seawater package. I change the bulk mixing algorithm to better represent mixing where units of concentration are involved, *i.e.* for salt and BGC tracers. Finally, I increase the threshold for the static instability deepening step. This is to compensate for higher sensitivity in the model following the change in the mixing algorithm.

3.6   Determination of the main drivers of pCO$_2$ variability

Changes in $p\mathrm{CO}_2^{\mathrm{oc}}$ may be broken down into four major contributors: sea surface salinity (SSS), sea surface temperature (SST), DIC, and Alk. Their relative impact on surface $p\mathrm{CO}_2^{\mathrm{oc}}$ can be estimated using Taylor expansion, where the change in $p\mathrm{CO}_2^{\mathrm{oc}}$ due to a given driver is multiplied by the change in the driver itself:

$$\frac{\mathrm{d}p\mathrm{CO}_2^{\mathrm{oc}}}{\mathrm{d}t} = \frac{\partial p\mathrm{CO}_2^{\mathrm{oc}}}{\partial \mathrm{SST}}\frac{\mathrm{dSST}}{\mathrm{d}t} + \frac{\partial p\mathrm{CO}_2^{\mathrm{oc}}}{\partial \mathrm{SSS}}\frac{\mathrm{dSSS}}{\mathrm{d}t} + \frac{\partial p\mathrm{CO}_2^{\mathrm{oc}}}{\partial \mathrm{DIC}}\frac{\mathrm{dDIC}}{\mathrm{d}t} + \frac{\partial p\mathrm{CO}_2^{\mathrm{oc}}}{\partial \mathrm{Alk}}\frac{\mathrm{dAlk}}{\mathrm{d}t} \quad (3.29)$$

The first fraction of each term can be expressed as a sensitivity of $p\mathrm{CO}_2^{\mathrm{oc}}$ to a given driver multiplied by the quotient of mean $p\mathrm{CO}_2^{\mathrm{oc}}$ and the mean of the driver (*e.g.(Metzl et al., 2010)*:

$$\frac{\mathrm{d}p\mathrm{CO}_2^{\mathrm{oc}}}{\mathrm{d}t} = \tau\overline{p\mathrm{CO}_2^{\mathrm{oc}}}\frac{\mathrm{dSST}}{\mathrm{d}t} + \eta\frac{\overline{p\mathrm{CO}_2^{\mathrm{oc}}}}{\overline{\mathrm{SSS}}}\frac{\mathrm{dSSS}}{\mathrm{d}t} + \gamma\frac{\overline{p\mathrm{CO}_2^{\mathrm{oc}}}}{\overline{\mathrm{DIC}}}\frac{\mathrm{dDIC}}{\mathrm{d}t} + \Gamma\frac{\overline{p\mathrm{CO}_2^{\mathrm{oc}}}}{\overline{\mathrm{Alk}}}\frac{\mathrm{dAlk}}{\mathrm{d}t} \quad (3.30)$$

Overbar denotes the mean of a component. τ is the thermodynamic change in $f\mathrm{CO}_2^{\mathrm{oc}}$ with temperature and is $0.0423°\mathrm{C}^{-1}$ (*Takahashi et al.*, 1993). η is 1.0 for cold water (*Takahashi et al.*, 1993), which is slightly higher than the value used by *Metzl et al.* (2010) (0.9). The marine carbonate program "CO2SYS" (*Lewis et al.*, 1998; *Humphreys et al.*, 2022) calculates γ, which is the DIC Revelle factor. A γ of 13.8 is applied here. Γ is the Alk Revelle factor. Γ was not available as an output in the utilized version of CO2SYS. Instead the Alk buffer factor was estimated in CO2SYS and the relation $\gamma{=}\mathrm{DIC}/\beta_{\mathrm{DIC}}$ was assumed applicable also to Alk such that $\Gamma{=}\mathrm{Alk}/\beta_{\mathrm{Alk}}$. The Revelle factor relation for DIC is from *Egleston et al.* (2010). In these equations, β denotes DIC and Alk sensitivities. $\Gamma = $ -13.2 for this application.

Freshwater impacts on DIC are accounted for explicitly as (*e.g. Fröb et al. (2019)*):

$$\frac{\mathrm{d}p\mathrm{CO}_2^{\mathrm{oc}}}{\mathrm{dDIC}} = \gamma\frac{\overline{p\mathrm{CO}_2^{\mathrm{oc}}}}{\overline{\mathrm{DIC}}}\left(\frac{\overline{\mathrm{sDIC}}}{\mathrm{SSS}_0}\frac{\mathrm{dSSS}}{\mathrm{d}t} + \frac{\overline{\mathrm{SSS}}}{\mathrm{SSS}_0}\frac{\mathrm{dsDIC}}{\mathrm{d}t}\right) \quad (3.31)$$

dpCO$_2$/dDIC is the sensitivity of pCO$_2$ to DIC. SSS$_0$ is a reference salinity, taken as 35. sDIC is DIC normalized to this reference salinity, SSS$_0$. The first term in the brackets represents the influence of freshwater. The second term is salinity normalized and therefore excludes freshwater. This means the physical and biological influences remain.

3.7 Quantification of uncertainties

The end result in this work, and the result associated with the highest uncertainty, is F$_{BIO}$. All uncertainties in the underlying calculations are propagated into its uncertainty. To calculate the absolute uncertainty in F$_{BIO}$ would require extensive, time consuming methods such as a Monte Carlo analysis. Due to time limitations, I instead focus on the largest uncertainties through a simple "sum of squares" method. This approach takes the uncertainty in a result as the root of the sums of each underlying uncertainty squared. By squaring each uncertainty, the larger uncertainties are given more weight. For F$_{BIO}$, the total uncertainty σ_{NCP} can be estimated as the root of the squared uncertainty of the model profiles plus the squared uncertainty of a measured Argo profile:

$$\sigma_{NCP} = \sqrt{\sigma_{model}^2 + \sigma_{Argo}^2} \tag{3.32}$$

where σ_{model} is the uncertainty in model profiles and σ_{Argo} is the measurement uncertainty of the property used to calculate NCP (*i.e.* DIC, nitrate, or oxygen). The major uncertainties in the model profiles lie in the uncertainties of the modelled air-sea gas exchange ($\sigma_{F_{GE}}$) and vertical transport (σ_{F_Z}), and in the measurement uncertainty:

$$\sigma_{model} = \sqrt{\sigma_{F_{GE}}^2 + \sigma_{F_Z}^2 + \sigma_{Argo}^2} \tag{3.33}$$

where

$$\sigma_{F_{GE}} = \sqrt{\sigma_k^2 + \sigma_{pCO_2}^2} \tag{3.34}$$

In Equation (3.34), σ_k is the uncertainty in the gas transfer velocity k, and σ_{pCO_2} the uncertainty in pCO$_2^{oc}$. The uncertainty in pCO$_2^{atm}$ is small compared to that of pCO$_2^{oc}$ and k, and is therefore neglected.

σ_{Argo} is the uncertainty in DIC for the main results. DIC is calculated using pH and Alk as input parameters in CO2SYS. Supplying the uncertainties of the input parameters and dissociation constants used, CO2SYS calculates the uncertainties into the output parameters - here, this is both DIC and pCO$_2$. Using the uncertainties listed in Table 3.2, σ_{Argo} and σ_{pCO_2} are 10 µmol kg^{-1} and 12 µatm respectively, corresponding to percentages of 0.5 and 3%. However, pCO$_2$ within the model is calculated from DIC and Alk. The model uncertainty in pCO$_2$ therefore needs to use σ_{DIC} and Alk as input. This results in σ_{pCO_2}=10%. σ_{F_Z} is obtained from a sensitivity analysis detailed in Section 5.1.1 and is 15%. Finally, σ_k is taken as 20% following *Wanninkhof* (2014). With these values, the resulting uncertainties are 22% for $\sigma_{F_{GE}}$, 15% for σ_{F_Z}, and 27% for σ_{NCP}.

For NCP estimates derived from nitrate and oxygen, the concept is the same, however σ_{Argo} changes according to their respective measurement uncertainties (5 and 30 µmol kg^{-1}). Additionally, there is no gas exchange affecting nitrate, while there is added uncertainty

in oxygen gas exchange due to the introduction of bubbles. Bubble uncertainty is 100% (*Nicholson et al.*, 2015). This results in $\sigma_{NCP_{NO3}}$ and $\sigma_{NCP_{OX}}$ of 53% and 104%.

Note that sum of squares method assumes the uncertainties in question are random and independent. Although this assumption is invalid for our application, it gives an idea of the magnitude of errors involved.

Table 3.2: Uncertainties associated with dissociation constants of the marine carbon system.

Constant	σ (fraction)	Component
pK_0	0.002^a	CO_2
pK_1	0.011^b	Carbonic acid K_1
pK_2	0.011^b	Carbonic acid K_2
pK_W	0.01^a	Water
pK_A	0.02^a	Aragonite
pK_C	0.02^a	Calcite
pK_B	0.02^a	Boric acid
TB/S	0.02^a	Total Borate/Salinity

[a] (*Orr et al.*, 2018)
[b] (*Sulpis et al.*, 2020)

Chapter 4

Results

This chapter details the thesis results. It is separated in three sections. First, Argo float measurements are presented and compared to historical data. The second section concerns model performance. Finally, the derived carbon fluxes and their drivers are presented.

4.1 Hydrography and biogeochemistry as observed by an Argo float

The high frequency and vertical resolution offered by Argo floats form the basis of this thesis. To use these as model input, however, we must ensure they are representative of the area and the time - model output quality reflects model input quality. In this section the observations are analysed and compared to historical data from the GLODAPv2 project (*Lauvset et al.*, 2016; *Key et al.*, 2015; *Lauvset et al.*, 2022).

Examination of the retrieved Argo data in potential temperature-salinity (θ-S) space is useful for determination of the water masses present through the measurement period. Figure 4.1 shows a θ-S diagram with GLODAPv2 data overlaid by Argo measurements colored by pressure level. Values above 100 dbar are excluded to avoid the influence of high variability surface water. This excludes the end-member of Polar Water (PW; $\theta < 0$; S<34.4; σ_θ <27.7). There is, however, a mixing line from (-1.7°C, 34.4) presumed to originate in PW. The water masses following this mixing line become warmer and more saline, indicating Atlantic Water (AW; θ >0; S>34.0) influence. Modified Atlantic Water (MAW; 0< θ <1; S<34.92; 27.97< σ_θ <28.02) is a product of mixing between PW and cooled AW. MAW resides some 200 dbar deeper than AW. Following the constant salinity mixing line further, Greenland Sea Arctic Intermediate Water (GSAIW; -1< θ <0; 34.80<S<34.92; 27.97< σ_θ <28.06) is found. This is an intermediate water mass known to occupy the 500-1500 m range (*Brakstad et al.*, 2019). It is the main product of winter convection in the Greenland Sea, produced by the cooling, and subsequent subduction of MAW in winter. Above GSAIW lies Greenland Sea Arctic Water, which is the deepest of the water masses considered to reside in the surface. The middle of the mixing line from GSAIW towards PW is likely this Greenland Sea Arctic Water mixed with PW. At the end of the same mixing line, we find Arctic Water mixed with
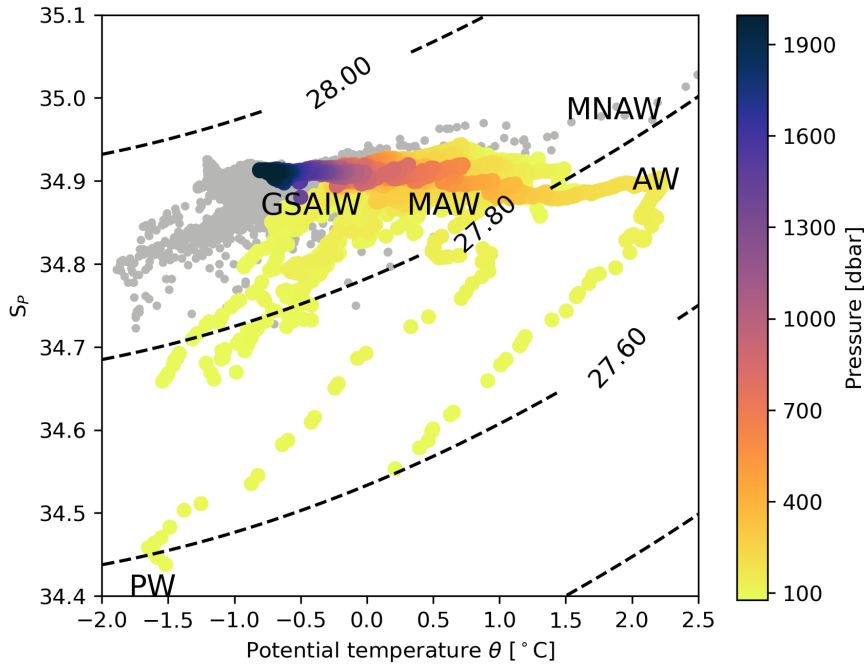
Figure 4.1: Potential temperature-salinity diagram of GLODAPv2 (small, gray, circles) and Argo data (larger, colored circles) from 100 to 2000 dbar. See Figure 3.2 for the GLODAPv2 measurement positions used. Dashed lines indicate σ_θ contours. The approximate position of different water masses in θ-S space are indicated using the following acronyms: PW: Polar Water; GSAIW: Greenland Sea Arctic Intermediate Water; MAW: Modified Atlantic Water; MNAW: Modified Norwegian Atlantic Water; AW: Atlantic Water using definitions from *Wang et al.* (2021)

PW. Compared to historical data, the Argo data exhibits higher temperatures, in line with the known development in the gyre (*Lauvset et al.*, 2018). While there appears to have been some influence of Modified Norwegian Atlantic Water (MNAW; $1< \theta <12$; $34.80<S<35.15$; $27.4< \sigma_\theta <27.97$) in GLODAPv2, this mixing line is not observed in the Argo data.

In addition to hydrographic properties, dissolved oxygen, nitrate, and pH were retrieved for a full annual cycle from the Argo float. Figure 4.2 shows the development of these variables as well as calculated Alk (from salinity), DIC (from Alk and pH), and potential density anomaly (from S_A and CT) in time and depth space.

A clear seasonal development is visible for all properties. The surface layer is warmer and fresher in summer months (June-October; Figure 4.2a). The low surface salinities are also reflected in lower surface concentrations of Alk (Figure 4.2), indicating dilution caused by freshwater input. In this period there are also signs of biological activity: depletion of nitrate and low DIC concentration, as well as increased oxygen and pH (Figure 4.2d, g, c, and e respectively).

Through winter there is a deepening of the mixed layer (solid line). The effect of heat loss cooling the surface waters is clear in Figure 4.2a. The cooling results in denser water masses which sink down, mixing in saltier water from below the thermocline in the process. Thus, as cooling progresses, the mixed layer becomes saltier and more dense as seen in Figure 4.2b and Figure 4.2f. Similar to salinity, oxygen, nitrate, DIC, and Alk are transported into the mixed layer from the bulk fluid below. This is evident from the increased concentrations of
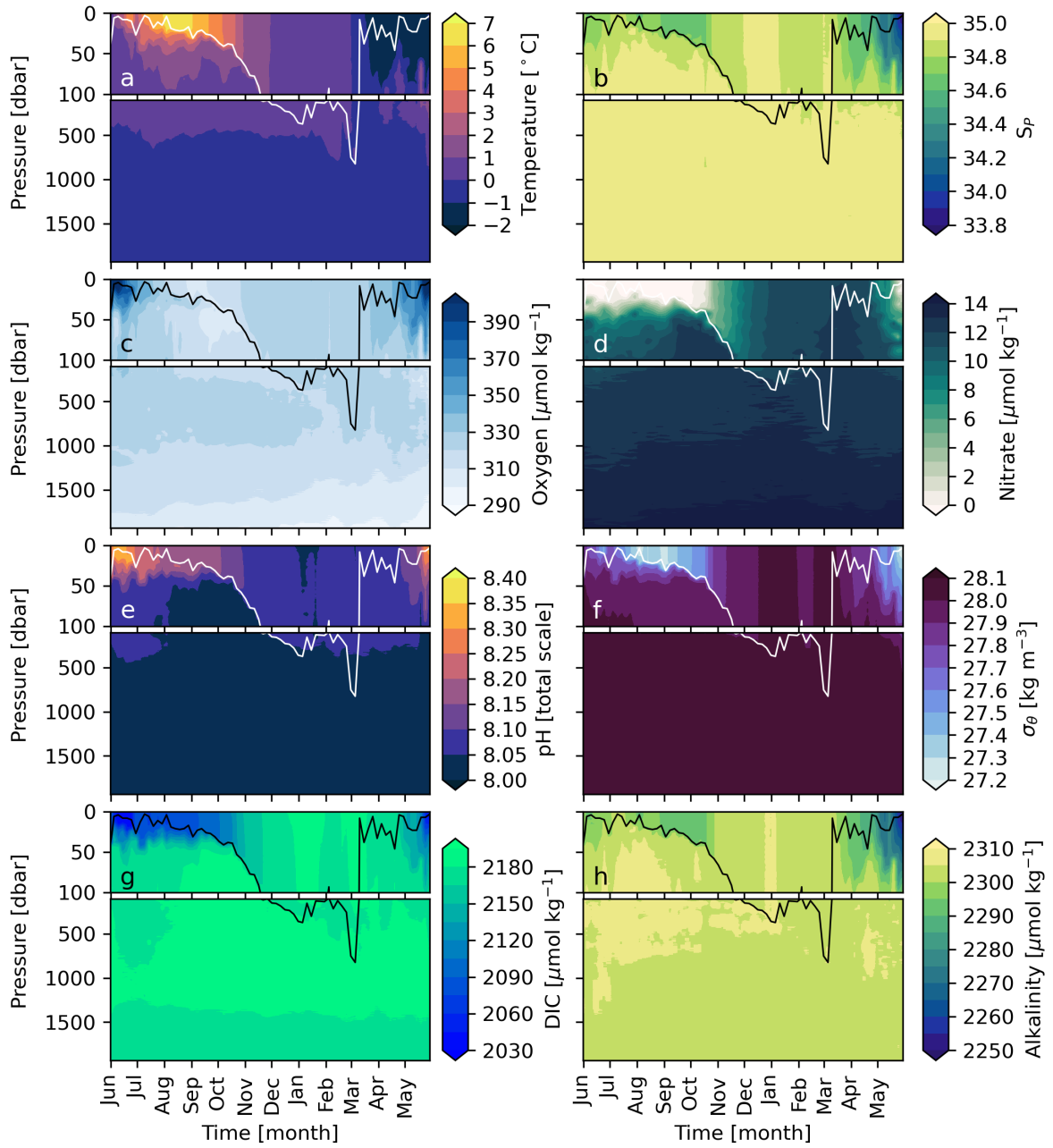
Figure 4.2: Hovmöller diagrams for the period June 2019-May 2020 displaying temperature (a), practical salinity (S_P; b), dissolved oxygen (c), nitrate (d), pH (e), potential density anomaly (σ_θ; f), DIC (g), and Alk (d). Note the different scales of the upper and lower y-axis of each plot. Mixed layer depth calculated using the Nilsen method is shown as a solid line.

these tracers through winter. As a result of the increase of DIC in the mixed layer, pH is reduced.

The increased oxygen and DIC concentrations in wintertime are not only due to mixing. Air-sea gas exchange also transfers these tracers into the mixed layer. At low temperatures, gas solubility in water is enhanced. Combined with strong winds in winter, the process may contribute to the higher concentrations. This is investigated further in Section 4.3.

By December, σ_θ is remarkably uniform. This is a well-known characteristic of the Greenland Sea. In January, the mixed layer depth reaches a maximum of approximately 370 dbar before a freshening event causes a slight shoaling. A second, deeper maximum (823 dbar) is reached in March as sub-zero temperatures are reached. An abrupt shoaling follows due to freshening of the upper 100 dbar of the water column. The surface water temperature at this time is still below zero degree Celcius. Such cold, fresh water could indicate PW influence.

Nitrate and DIC concentrations increase with depth, while oxygen decrease. This is a consequence of remineralization. Note also the oxygen-rich tongue at 500 dbar seen in Figure 4.2c which could be remnants from the previous winter's mixed layer.

Gradients below 500 dbar are small for all variables. This is expected because, as opposed to the surface layer, water masses below mixed layer depth are not affected by the rapid changes in atmospheric forcing. Additionally, there is little biological activity because photosynthesis requires light, and most remineralization occurs in the upper 1000 dbar. High variability at depth could therefore indicate sensor drift.

The large range in the color scale in Figure 4.2 is not suitable to assess sensor stability. To investigate this, values at 500, 1000, 1500, and 1900 dbar are plotted with time for each variable in Figure 4.3.

At 500 dbar water masses are affected by remineralization, and to some extent atmospheric forcing at the surface. The former is seen from increasing DIC and nitrate, and oxygen decreasing through the winter at this pressure level. When the mixed layer is deep, the latter becomes apparent in perturbations not observed at the deeper pressure levels. This is seen *e.g.* in March. In August there is a warming event which coincides with salinification (Figure 4.3b), indicating stronger influence of Atlantic Water at this time. This peak is also seen in Alk, which is natural due to its linear relation with salinity. The AW influence is not evident from any of the other tracers at 500 dbar.

In the end of February, there is a new warming event at 500 dbar caused by warmer surface water being mixed down by winter convection. As the mixed layer shoals, temperatures drop again. Similarly, oxygen in the period rises as waters newly in conctact with the surface are submerged and mixed with the oxygen-deficient water below. For nitrate, the 500 dbar pressure level shows clear signs of remineralization, with increasing values from the productive season through winter. At the time of deepest convection in February/March, nitrate is diluted as it is mixed with nutrient-depleted water from above. This same dilution is seen in σ_θ, DIC, and Alk. The reduction in DIC leads to raised pH values.

From 1000 dbar the seasonal signal and convection influence are no longer evident. Temperature and salinity, and their derivatives σ_θ and Alk, appear nearly constant. However, not all
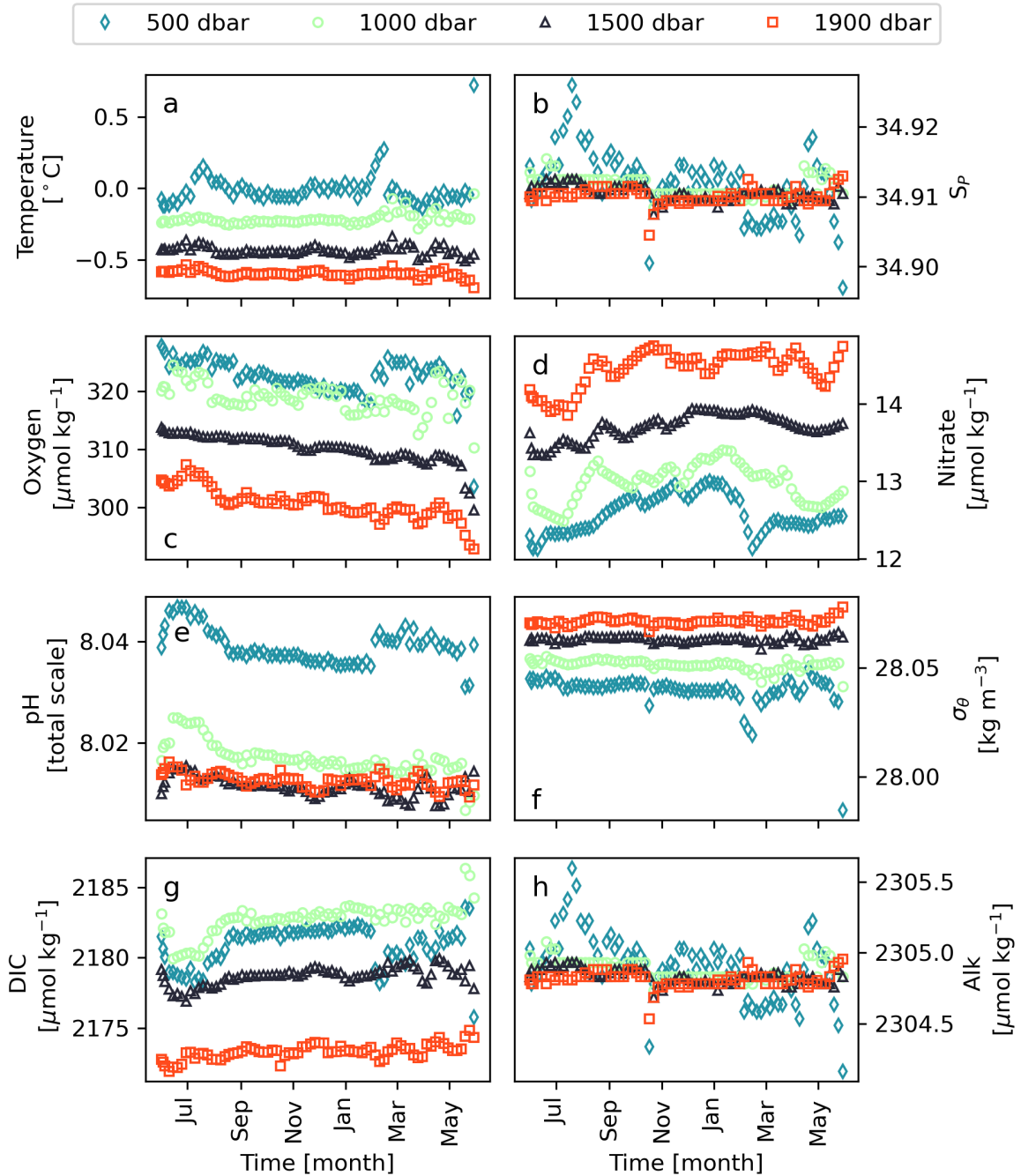
Figure 4.3: Timeseries of temperature (a), practical salinity (b), dissolved oxygen (c), nitrate (d), pH (e), potential density anomaly (σ_θ; f), DIC (g), and alkalinity (h) at 500, 1000, 1500, and 1900 dbar. The pressure levels are shown as blue diamonds, light blue circles, purple triangels, and red squares respectively.

values at these pressure levels are as stable as one would expect. There is a clear negative trend in oxygen of approximately 2%, too strong to be explained by remineralization alone. Remineralization should show some seasonality (more in the productive months), and most remineralization occurs within the upper 500 m of the water column (*Martin et al.*, 1987). The trend could be caused by sensor drift. The drift would propagate to pH and DIC because oxygen is used to validate the pH measurements, and pH is used to calculate DIC. Thus, if the trends are indeed caused by sensor instability, then the trends in oxygen, pH and DIC are all connected. The variability in nitrate, on the other hand, is independent of the oxygen sensor. There is a range of approximately 1.5 μmol kg^{-1} in the observed values between 1000 and 1900 dbar, and considerable oscillations within each pressure level. Additionally, a weak positive trend is seen in values at the two deepest pressure levels. The possibility of sensor drift is explored further in Section 5.2.2.

Thus far, the Argo measurements appear reliable despite some sensor drift. How do they compare to historical data? This is investigated in Figure 4.4, where vertical Argo profiles are plotted with GLODAPv2 bottle data (*Lauvset et al.*, 2022). In addition to the tracers shown in previous figures, apparent oxygen utilization (AOU) is plotted in Figure 4.4i. AOU is a measure of the oxygen consumed during remineralization (AOU = $[O_2]_{sat}$-$[O_2]_{observed}$; (*Sarmiento and Gruber*, 2006)) useful for, among other things, determining ventilation depths. Additionally, the temperature effects on the solubility of oxygen are removed in AOU. This makes it especially useful in areas such as the Greenland Sea where temperatures have increased.

There is good agreement between the Argo and GLODAPv2 data for most variables. The Argo data appears somewhat warmer than the historical data at all depths. This is consistent with current literature stating there has been a warming of the Greenland Sea (*e.g. Lauvset et al.* (2018)).

Salinity does not reach the lower range of historical values (<33.0), but does otherwise not deviate substantially from the GLODAPv2 data. Full overlap in the surface is not expected as there may be large interannual variability in precipitation, evaporation, ice formation, and ice melting. The Greenland Sea salinity is affected by both the North Atlantic Oscillation (NAO) climate mode, and variability upstream in the Arctic Ocean.

Argo oxygen values appear relatively consistent with historical data. Most of the GLODAPv2 data agree with the Argo observations. Below 100 dbar there are some discrepancies in which the GLODAPv2 data are more oxygenated than the Argo values. A possible explanation is reduced solubility compared to GLODAPV2 data resulting from the observed temperature increase in Figure 4.4a. At first glimpse, this may seem at odds with the work of *Lauvset et al.* (2018) who found that total oxygen inventory in the Greenland Sea has increased since the turn of the century. However, the reason for this increased oxygen inventory is that the depth of the well-ventilated water masses has increased. Most likely, the upper range of oxygen values seen in the GLODAPv2 data is an expression of eddy activity. Eddies can lead to high oxygen concentrations down to 2200 m in the Greenland Sea (*Gascard et al.*, 2002).

Nitrate concentrations measured by Argo fall into the lower range of GLODAPv2 values, consistent with the recent GLODAPv2 concentrations seen in Figure 2.4.

Figure 4.4e clearly shows the effect of anthropogenic carbon on pH: the Argo measurements
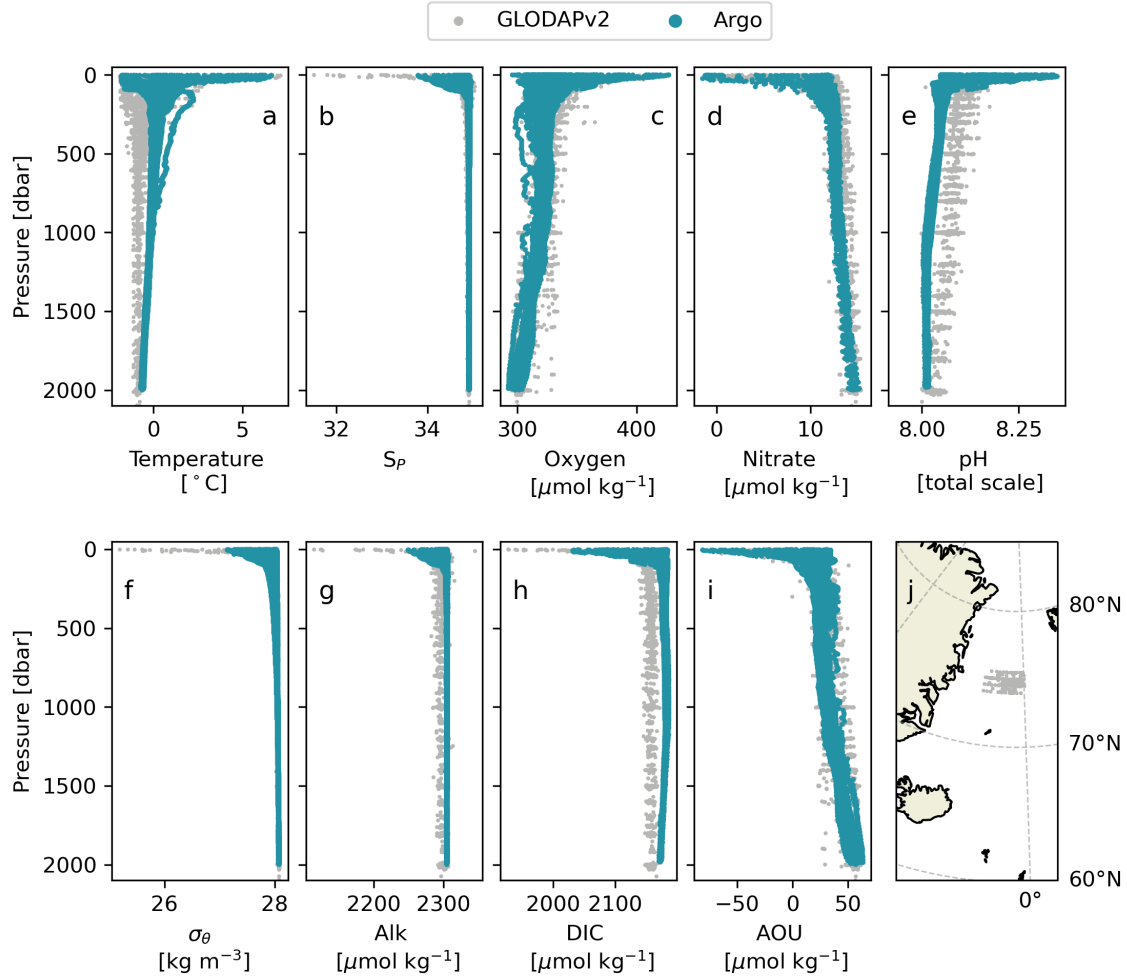
Figure 4.4: Vertical profiles of temperature (a), practical salinity (S_P; b), oxygen (c), nitrate (d), pH (e), potential density anomaly (σ_θ; f), alkalinity (d), DIC (e), and AOU (f) for Argo (blue dots) and GLODAPv2 (gray, smaller dots) data from the Greenland Sea. GLODAPv2 measurent locations are mapped in j and span 1982-2019 (see Chapter 3 for further details; (*Lauvset et al.*, 2022)).

are significantly lower than those from GLODAPv2, indicating increased ocean acidification. A corresponding positive deviation is seen in DIC in Figure 4.4h, reflecting the increased concentration of anthropogenic carbon. As the included historical data spans from 1982 to 2019, there is a slight overlap with the Argo measurements of this work. However, most of the GLODAPv2 data is from 2000-2010, and even earlier for the Western part of the gyre studied here, which explains some of the discrepancies. Another likely cause is incoherences between measured and calculated properties of the carbon system. In the Argo data, the only directly measured carbon system parameter is pH. Alk and DIC are calculated. For GLODAPv2, on the other hand, most Alk and DIC values are measured ones while pH is typically calculated. Discrepancies between calculated and measured carbon system properties have been declared an important challenge needing resolve within the ocean carbon chemistry community (*Álvarez et al.*, 2020; *García-Ibáñez et al.*, 2022).

The comparison is further complicated by the use of different carbonate system dissociation constants and software. GLODAPv2 applies the K_1 and K_2 of *Lueker et al.* (2000), total boron to chlorinity ratio of *Uppström* (1974), and the 1990 sulfate constant of Dickson

Dickson (1990). Here, I use *Sulpis et al.* (2020) for K_1 and K_2 to account for the cold temperatures intrinsic to the Greenland Sea. For boron to chlorinity, I apply constants from *Lee et al.* (2010), leaving only the sulfate constants parameterized using the same constants.

Also present in both pH and DIC is the changing slope with depth from aound 1200 dbar in the Argo data not found in the historical data. In addition to the aforementioned differences in carbon system properties between Argo and GLODAPv2 data, it is possible that a portion of the observed differences is connected to sensor instability.

High-latitude density is governed by salinity. This is mirrored in the σ_θ profiles (Figure 4.4f). The influence of salinity on other tracers is also evident in Figure 4.4g where Alk profiles are shown. Although Alk (Figure 4.4d) is linearly related to salinity, it shows a clear increase compared to historical values. This could be related to increased salinity reported in the region. This is also seen in Figure 4.5.

AOU reflects the oxygen concentration change relative to 100% saturation. Negative values, as seen at surface level in Figure 4.4i, thus indicate biological production as observed oxygen concentrations are greater than saturation concentration. Conversely, positive AOU signifies undersaturated water masses indicative of remineralization and a lack of contact with surface water. Argo AOU lies around 20 µmol kg^{-1} in the 250-1000 dbar range before increasing towards concentrations exceeding 50 µmol kg^{-1} at 1900 dbar. The lower values at mid-depth indicate there could be ventilation down to around 1000 dbar for the 2019/2020 winter season, in line with the mixed layer depth maximum of around 800 dbar calculated for the Argo data (Figure 4.2). The values are consistent with values of 19.5±2.2 in GSAIW (500-1000 m) and 54.5±4.2 in GSDW (2000-3000 m) as calculated for the 2010s by *Jeansson et al.* (2023). Some instances of lower GLODAPv2 AOU even at 1900 dbar demonstrate events of deep convection and/or eddy activity in the past.

As signs of possible sensor drift were seen in Figure 4.3, it is instructive to compare Argo values at depth to GLODAPv2. In Figure 4.5, temperature, salintiy, oxygen, nitrate, pH, σ_θ, Alk, DIC, and AOU are therefore plotted from 1000 to 1933 dbar for both Argo and GLODAPv2 data.

Argo temperatures decrease with depth at a rate unlike the gradient seen in most of the GLODAPv2 data. For GLODAPv2, there is a moderate gradient for 2018-2019, indicating that this could be a new development of the temperatures in the gyre rather than measurement errors. Also notable is the elevated Argo temperature compared to GLODAPv2 values from the 1980s and 1990s. As noted above, this is an expression of the known warming of the Greenland Sea gyre.

Salinity is uniform through the selected pressure levels for both Argo and GLODAPv2. Argo values are somewhat greater than the historical data. As for temperature, this is in line with the aforementioned warming and salinification of the region.

Oxygen Argo concentrations decline with depth. From 1200 dbar, GLODAPv2 values for more recent years are higher than Argo values. It is possible that this is an artifact related to sensor instability, whereby sensor drift increases with pressure. Alternatively, it could be caused by remineralization and lack of ventilation. AOU is helpful for assessing the latter and is discussed below.
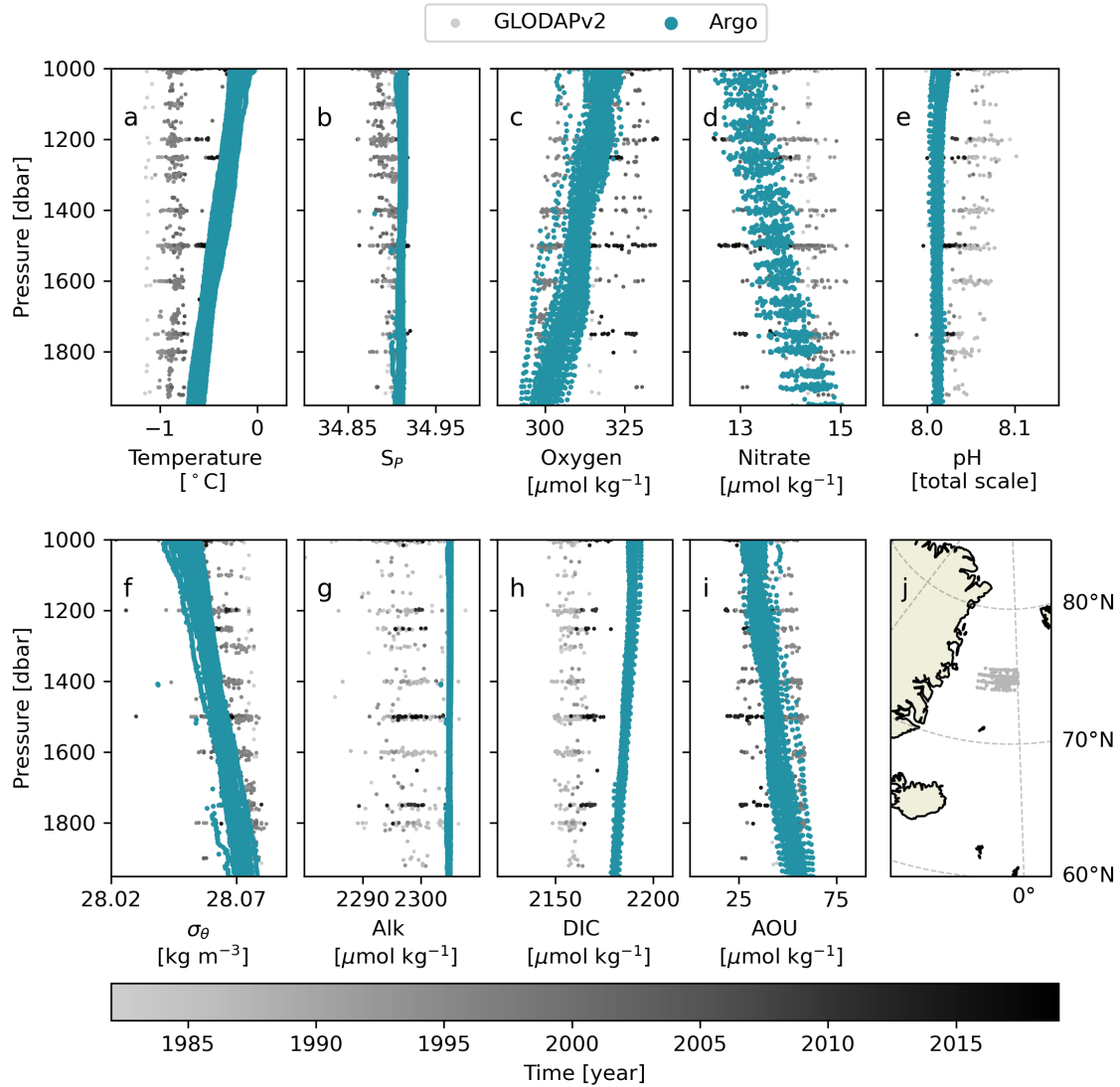
Figure 4.5: Vertical profiles of temperature (a), practical salinity (S_P; b), potential density anomaly (σ_θ; c), alkalinity (d), DIC (e), pH (f), oxygen (g), and nitrate (h) for Argo (blue dots) and GLODAPv2 (gray, smaller dots) data 1982-2019 from the Greenland Sea (*Lauvset et al.*, 2022).

Figure 4.5d shows increasing nitrate with depth in the Argo data, whereas GLODAPv2 is relatively constant with depth. Gradients in the 1200-1900 dbar range are expected because these depths have been more ventilated in recent years. The range represents the divide between newer GSAIW and old deep-water. As this divide deepends with time, gradients arise. The gradient is not seen in the GLODAPv2 data because, as mentioned previously, this dataset is not heavily sampled in the West Greenland Sea, and most of the data is from the early 2000s.

As was seen in Figure 4.4, pH is lower for Argo data than GLODAPv2 due to anthropogenic carbon invasion. In Figure 4.5e, the difference in vertical structure at depth is seen more clearly. While GLODAPv2 features a negative gradient from 1000 to 2000 dbar, Argo pH is nearly uniform with pressure. As previously hypothesized, this incoherence in vertical structure could be explained by the method by which the pH data is obtained. Additionally, pH is expected to decrease more in the upper part of the water column because the anthropogenic

carbon is injected at the surface. It takes time for the anthopogenic carbon to sink to the depths shown in Figure 4.5.

σ_θ at depth appears to be governed by temperature, as is expected due to the uniform salinity in the selected pressure range. The result is a somewhat stronger vertical gradient than seen in the historical data.

The linear dependence of Alk on salinity appears robust also at depth: both GLODAPv2 and Argo concentrations are uniform with depth. Argo Alk is higher than historical data due to the salinification of the gyre.

The quite a bit higher DIC concentrations calculated from Argo data compared to GLODAPv2 measurements was debated in connection with Figure 4.4. As for pH, the discrepancy becomes more evident when examined in the 1000-2000 dbar range. Although there is an increase in GLODAPv2 measured concentrations with time, the values from the most recent years are not as high as the Argo calculated levels. Nevertheless, the vertical structure seen in Argo pH is mirrored in DIC. This is expected since pH was used to calculate DIC.

AOU in the 1000-2000 dbar range shows possible signs of convection down to 1000-1200 dbar, where values lie around 30 μmol kg^{-1}. Towards 2000 dbar, increasing values indicate oxygen consumption in line with the observed gradients in oxygen and nitrate in Figure 4.3c and d. However, this interpretation must be treated with care in light of the possible sensor drift seen in oxygen. A drift towards lower concentrations in oxygen would appear as a false remineralization signal.

AOU is not only useful for evaluating ventilation and oxygen consumption, but also for evaluating other components pertaining to the biological system. Another valuable property in this regard is C*. C* is a conservative tracer where the biological effects on carbon are removed (*Gruber and Sarmiento*, 2002). Changes in C* with time are thus driven by mixing and air-sea gas exchange, and therefore more strongly reflect the uptake of anthropogenic carbon. Figure 4.6 shows how nitrate (Figure 4.6a), DIC (Figure 4.6b), C* (Figure 4.6c) and DIC-C* (Figure 4.6d) change with increasing AOU for Argo data and historical values below 100 dbar. The exclusion of data above 100 dbar is to avoid the strongest effect of seasonal variation.

As expected, there is a positive linear relationship between AOU and nitrate as oxygen is consumed and nitrate produced during remineralization. Both nitrate and AOU are thus lower closer to the surface, and increase towards 1900 dbar. Since values above 100 dbar are excluded, nitrate is not depleted. Visually, the slope and intercept of the Argo data harmonise well with historical values. This is clearly not the case for DIC where both the slope and intercept differ significantly from the GLODAPv2 values. To explain this deviation, it is useful to decompose the DIC signal into its physical and biological parts using C*.

The convenience of C* as a proxy for uptake of anthropogenic carbon is clear from Figure 4.6c. Here, we see an increase in historical C* with time. The increase with time is caused by absorption of anthropogenic carbon. Without the biological influence, carbon (C*) is negatively correlated to AOU. Water in recent contact with the atmosphere have higher values of anthropogenic carbon, increasing total carbon content, *i.e.* DIC. Newly ventilated water is near saturation with respect to oxygen, and therefore has lower AOU. As seen
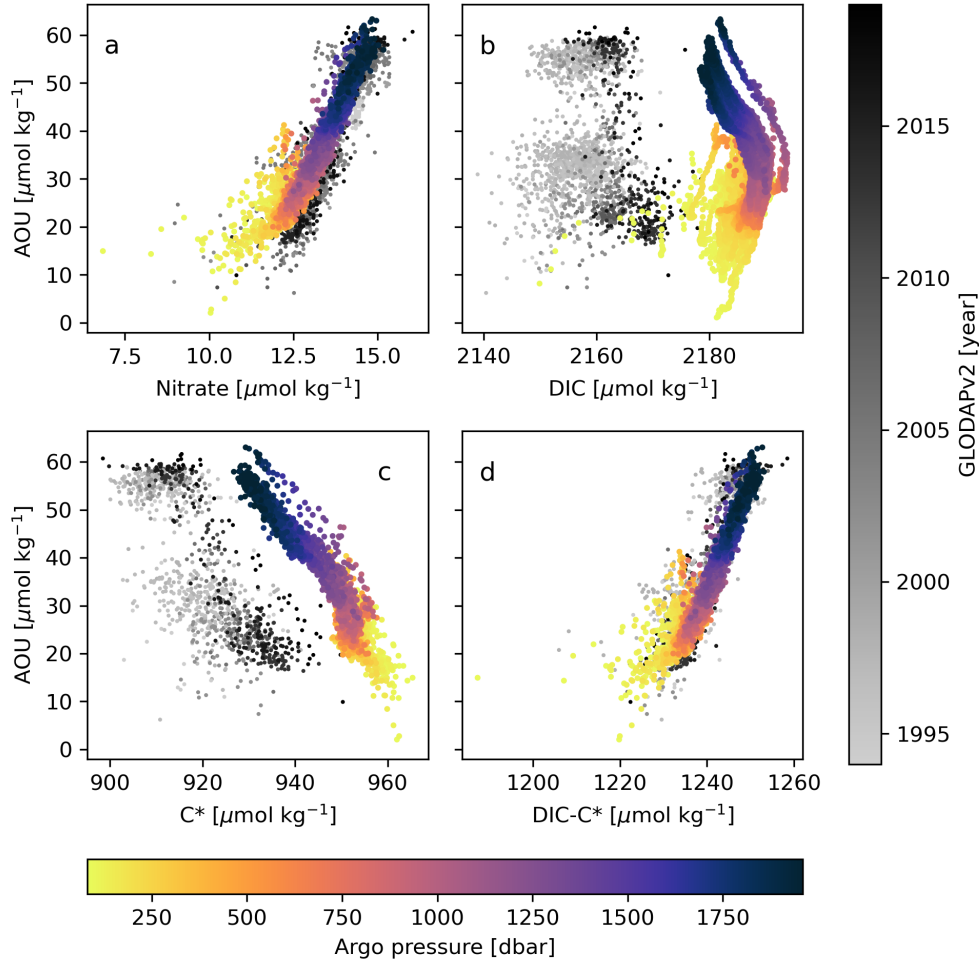
Figure 4.6: AOU plotted against nitrate (a), DIC (b), C* (c), and DIC-C* (d) for Argo (yellow-to-purple dots scaled by pressure level) and GLODAPv2 (smaller dots grayscaled by year of measurement; (*Lauvset et al.*, 2022)).

throughout this chapter, Argo DIC is overestimated. There should be an overlap for both C* and DIC values between the newest GLODAPv2 values from 2019 and those of the Argo float employed in this work, which were obtained in 2019-2020. However, this is not evident. In part, this is likely both because of spatial variabiliy, and a lack of winter data in GLODAPv2. Also notable is the AOU range of 20-30 μmol kg^{-1} where C* is near constant with increasing AOU. It is possible that this is an artifact caused by earlier mentioned sensor drift.

Subtracting C* from DIC, we are left with the biological component. This parameter, like nitrate *vs.* AOU, is independent of anthropogenic carbon influence and therefore coincides with the historical values. It mirrors Figure 4.6a because it essentially shows R×[NO$_3$] *vs.* AOU.

Figure 4.6b reflects both the effects of both biology and air-sea gas exchange. Biology dominates at 100-500 dbar, following a positive gradient also seen in Figure 4.6a. In this range organic matter is remineralized, increasing both DIC and AOU. In the deep, there is little matter left to remineralize and the water masses are old. The slope therefore changes direction, matching that of Figure 4.6c. Here, the anthropogenic carbon signal dominates. From the GLODAPv2 data, one might expect the DIC:AOU relation to follow a more vertical

pattern. This is not the case for the Argo data. Between 500 and 1000 dbar, values slope towards a DIC maximum. Remnants of this shape is also seen in the C*:AOU relation. The region indicates that there is a layer of DIC-rich water far removed from the surface. It is likely GSAIW as this is the dominating water mass in the pressure range. GSAIW is produced by convection. It has therefore been in contact with the surface recently compared to the water masses below. This explains its rich DIC content. This signal of high DIC at 500-1000 dbar is not picked up by GLODAPv2 because nearly all the data is from summer cruises. It is possible that some of the discrepancy between Argo and GLODAPv2 observed here relates to the differences between calculated and measured DIC.

Recall, however, the inconsistencies in the DIC vertical profiles at pressures between 500-1500 dbar seen in Figure 4.4e. These do affect the slopes of the discussed figures to some extent, yet the overall agreement with historical data is considered good.

4.2 Model validation

After adding relevant processes and tracers (see Chapter 3), the PWP model was run with hourly forcing using gridded vertical profiles from the first Argo station as initialisation conditions. Figure 4.7 shows the development of important tracers in the upper 30 m as well as the mixed layer depth, when the model was "run-free" after the first initialisation (*i.e.* only profiles from the first Argo station are used and the model is not adjusted by further reinitializations through the run).

In general, the free-run model performs within the range one could expect from a one-dimensional model. It resolves temperature quite well, with a clear September peak and subsequently dropping values not dramatically different to those observed. A later onset of mixed layer deepening in the model than estimated for the Argo data results in somewhat colder modelled values in January-February. From March and onwards, the Argo float was influenced by advection of colder, fresher polar water. Naturally, this development is not captured by the model, resulting in a warm bias in this period.

Oxygen in an abiotic model is governed by its solubility in periods when there is little vertical mixing. This is reflected in the development seen in Figure 4.7b, where oxygen concentrations decrease along with increasing temperatures from June to September. As temperatures then drop, solubility and air-sea gas exchange of oxygen is strengthened, leading to higher concentrations. In the modelled cold-spell of January-February, oxygen is overestimated. In reality, the warmer temperatures mixed up at this time leads to a weak increase towards the productive season starting in April/May. The elevated Argo concentrations at the end of the time series are both due to biological production of oxygen, and to increased solubility caused by lower temperatures as the Argo float encountered cold PW. Neither biology nor advection of water masses are included in the model, leading to more moderate modelled concentrations at the end of the run.

Surface salinity is underestimated from September to February. As the Argo mixed layer deepens from the end of October, salt is mixed up to the surface. In the model, however, the later onset of mixed layer deepening causes freshwater from precipitation to accumulate, leading to lower salinities. This freshening further delays mixed layer deepening as it increases
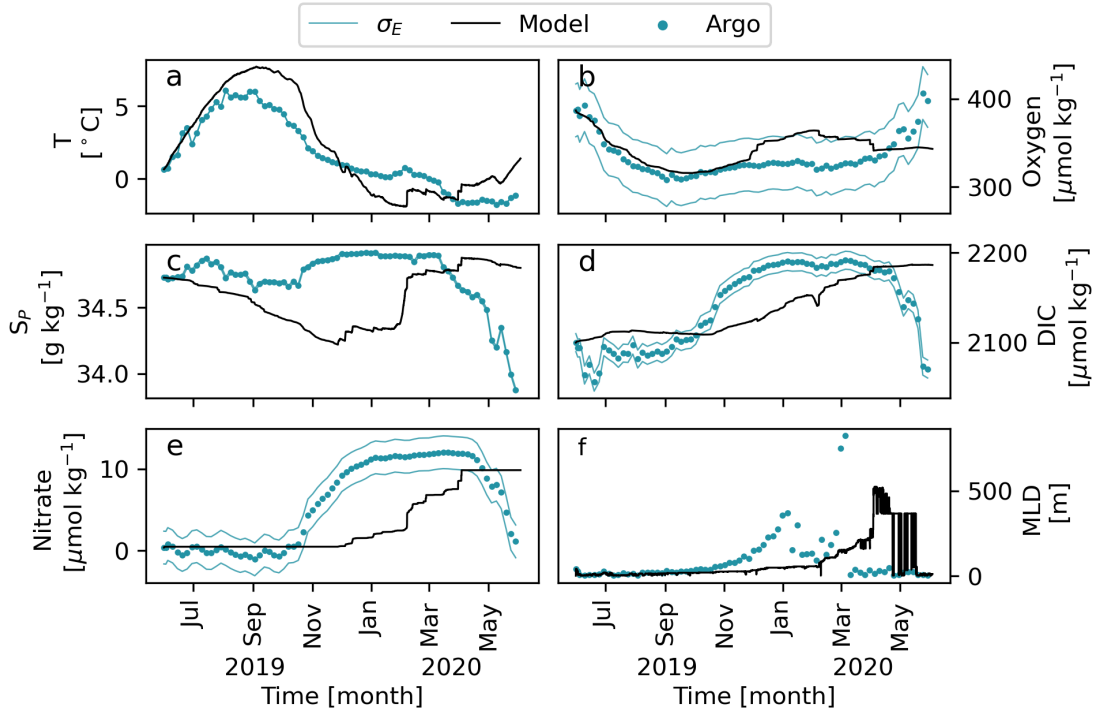
Figure 4.7: Mean surface values (upper 30 dbar) of temperature (T; a), oxygen (b), practical salinity (S_P; c), DIC (d), and nitrate (e) for Argo (blue dots) and model (black line) data. Blue, thin lines indicate upper and lower bounds of measurement uncertainty (σ_E) for each property. Panel f shows mixed layer depths calculated using the Nilsen method for the same datasets. The x-axis shows dates in months.

stratification, enabling the cooling mentioned in January-February. The cooling densifies the water mass sufficiently that the model mixed layer may start deepening from February. In turn, this increases surface temperatures and salinity as warmer, saltier water masses are mixed upwards. From March, the aforementioned polar water influence on the Argo data leads to significantly lower salinity in the Argo data than salinities predicted by the model.

Modelled DIC is greater than Argo DIC from the start of the timeseries until September as the effect of biological consumption is not accounted for in the model. From November, mixing, and possibly air-sea gas exchange, increase Argo DIC surface concentrations. Modelled DIC starts increasing from February due to vertical mixing and air-sea gas exchange. Since there is no biological consumption, DIC continues to increase in the model. In the Argo data, however, concentrations drop rapidly from March as the phytoplankton bloom starts.

As the initialisation profile is a summer profile, modelled nitrate values are low until the mixed layer starts deepening and nitrate is mixed to the surface. The delayed mixed layer deepening in the model results in a large deviation in nitrate concentrations between Argo and predicted values from November when mixing in reality starts. As the modelled mixed layer deepens, nitrate increases. It never reaches the maximum measured value seen in the Argo data. This is possibly due to some remineralization captured in the Argo data not resolved in the model. As seen for DIC, Argo nitrate is drastically reduced as the blooms start while the abiotic model results in continously high values until the end of the run.
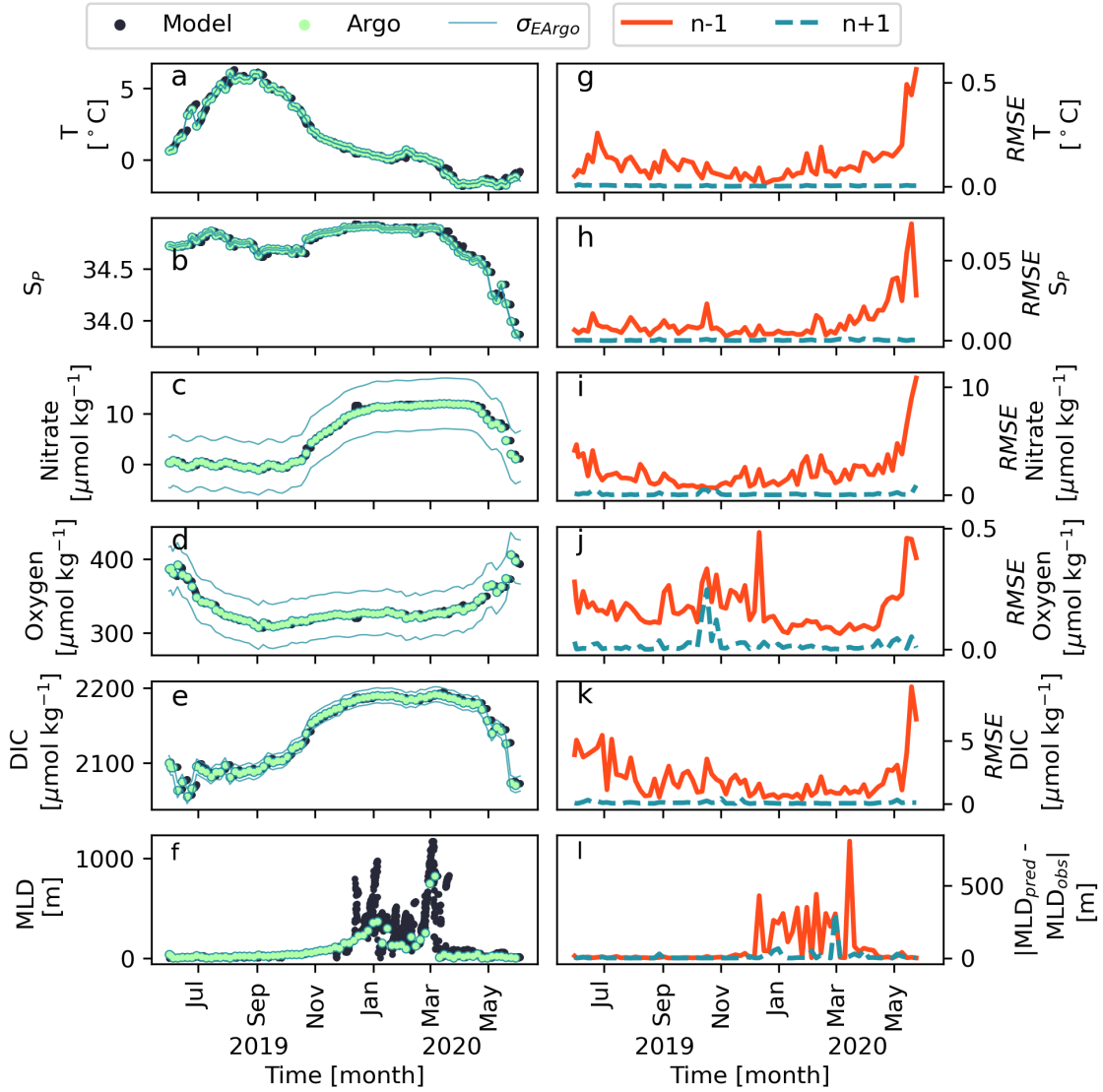
Figure 4.8: The left panels (a-e) show mean surface values (upper 30 dbar) of temperature, S_P, nitrate, DIC, and oxygen respectively. Light green circles are Argo measurements and black dots show modelled values. Thin, blue lines indicate upper and lower bounds of Argo measurement uncertainties. The right panels (g-k) show root mean square error (RMSE) between model and Argo values over the entire measured depth (1933 dbar) for the same tracers as the left panel. RMSE is evaluated at the time step before (n-1; solid red line) and after (n+1; dashed blue line) reinitialization of the model. The bottom panels show calculated mixed layer depth (MLD) using the Nilsen method for observations and model results (f), and the absolute difference in MLD estimates evaluated at the same timesteps as the other tracers (l).

Model performance is increased significantly when it is reinitialized at every Argo station. This is evident from Figure 4.8, where a-f show mean values in the upper 30 dbar, and g-l show the root mean square error (RMSE) between the model and Argo data for the full water column at the timesteps before (n-1) and after (n+1) reinitialization. Note that for mixed layer depth, the absolute difference is used.

Compared to the free run the surface development is reproduced very well by the model, although it generally produces a deeper mixed layer than observed by Argo in winter (Figure 4.8f). The model also generates deeper mixing at the end of January compared to the Argo data. The additional mixing event causes no notable discrepancy in the surface values visible at the displayed scales.

RMSE(n-1) is a measure of the difference in modelled values at the timestep immediately before model reinitialization compared to the Argo value of the next reinitialization. This reflects the maximum error in modelled *versus* measured values. RMSE(n+1) is the error calculated by comparing the timestep immediately after reinitialization to the values of the newly initialized profile. RMSE(n+1) thus represents the minimum error in the model.

RMSE(n+1) shows very little model drift, with values on the order of 10^{-2} for nitrate, oxygen, and DIC (Figure 4.8c-e). RMSE(n+1) is even lower for temperature and salinity - on the order of 10^{-3} and 10^{-4} respectively (Figure 4.8a-b). This is expected, as these errors represent the model drift merely one hour after reinitialization. Conversely, RMSE(n-1) represents errors after approximately 5 days. Naturally, these values are somewhat higher. Here, we also see the effect of polar water advection from March in temperature and salinity leading to significantly higher RMSE at these late stages. For nitrate, oxygen, and DIC RMSE(n-1) is higher at both ends of the timeseries due to the abscence of biology in the model. This model drift caused by biological processes being captured in the Argo data but not in the model is the basis of NCP calculations later in this chapter. It is what enables us to separate physical and biological influence on DIC. Note that while biology is the main driver of the relatively high RMSE(n-1) in spring 2020, the polar water advection likely has some influence on these biogeochemical tracers as well. In oxygen, there is also an event of higher RMSE(n-1) in November-January. The event coincides with discrepancies in mixed layer depth (panel f) over time leading to more mixing of oxygen-poor water in the model than in reality between an initiated profile and the next.

Though several sources cite the PWP model as successful in predicting mixed layer depths for oceanic gyres (*Moore et al.* (2015); *Våge et al.* (2008)), only a few report concrete model validation metrics.*Briggs et al.* (2018) applied the PWP model to Argo data from the Ross Sea sea ice zone in the Southern Ocean. Although vastly different areas, their RMSE evaluation is a valid comparison as the magnitude of model-observation deviations should lie within the same thresholds regardless of location. Table 4.1 shows their validation results for temperature, practical salinity and mixed layer depth. The same metrics are shown for this work in addition to RMSE for DIC, nitrate, and oxygen. For their optimal model, *Briggs et al.* (2018) obtained RMSE values for the total water column of 0.089°C, 0.018 and 5.1 m for temperature, practical salinity and mixed layer depth respectively. In this work, the corresponding RMSE was 0.111°C, 0.011, and 39.5 m. The discrepancies are thus of similar magnitude, however RMSE for mixed layer depth is significantly higher for our application. This is not unexpected as the weak stratification of the Greenland Sea makes it challenging

to model winter convection depths. For the biogeochemical components, RMSE constitutes 0.1, 1.3, and 0.7% of the respective mean values for DIC, nitrate and oxygen. Due to their participation in biological processes, a larger RMSE is expected for these than for temperature and salinity.

Table 4.1: Root mean square errors (RMSE) over the whole water column. The comparison is executed for model predictions at the timestep before model reinitialisation compared to observations at the next reinitialised profile. Units are printed below each header.

$RMSE_T$ [°C]	$RMSE_{S_p}$	$RMSE_{DIC}$ [µmol kg^{-1}]	$RMSE_{NO3}$ [µmol kg^{-1}]	$RMSE_{OX}$ [µmol kg^{-1}]	$RMSE_{mld}$ [dbar]	Source
0.111	0.011	2.021	0.170	2.193	39.5	This work
0.089	0.018				5.1	*Briggs et al.* (2018)

RMSE is useful for quantifying errors, but does not show the sign of these errors. Plotting key variables predicted by the model at the timestep prior to reinitialization (subscripted *pred*) against observed values of the same variable (subscripted *obs*), we can determine if the model under- or overestimates certain variables. By using model values at the last timestep before reinitialization, we capture the greatest amount of error. This is shown in Figure 4.9. The value of the slope is used as a performance metric. A slope of 1.0 signifies perfect prediction by the model. For slope < 1.0 (slope > 1.0), the model overestimates (underestimates) the predicted values.

The slopes of the plotted tracers all lie within the range 0.979-1.006, indicating excellent prediction skill. However, the model strongly overestimates mixed layer depth (slope=0.767). The largest spread is seen at pressures lower than 500 dbar, as is expected due to the naturally high variability in surface waters which is difficult to capture perfectly in a model. The deepest mixed layers are underestimated by the model.

The model slightly underestimates temperature and salinity values overall, with slopes of 1.005 and 1.006 respectively. At high salinities, the predicted values are overestimated due to freshwater influence. Part of the overestimation in temperature and salinity is associated with the polar water advection from March seen in Figure 4.8.

For oxygen, nitrate and DIC, deviations from the observed values are expected due to biological processes. These are indeed overestimated as the model does not take into account consumption of nitrate and DIC in the productive season. Note that although nitrate visually appears to have the greatest spread, this is a visual artifact caused by its small concentrations in seawater. Spread in DIC, which has much higher concentrations in seawater, appears smaller in comparison yet the values of the slopes show that this is not the case.

As was seen in Figure 4.8, the difficulty in predicting mixed layer depth does not significantly influence the model's ability to predict tracer concentrations and to respond to the applied forcing.
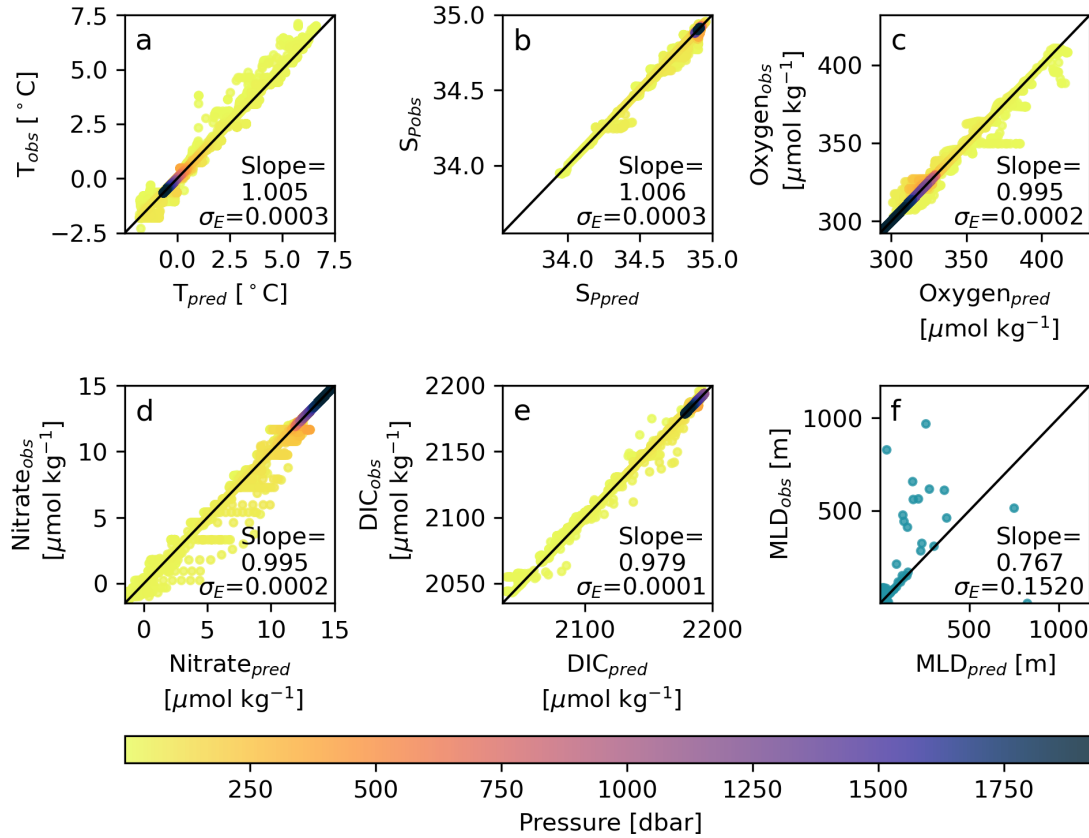
Figure 4.9: Predicted *versus* observed values of CT (a), S_A (b), oxygen (c), nitrate (d), DIC (e), and mixed layer depth (MLD; f). The model (predicted) values are taken at the last time step before reinitialisation and the observed values are taken as the next initialised Argo profile. Linear regression was performed on each set of values. The resulting slope and its and standard deviation (σ_E) is printed at the bottom of each plot. Black diagonal lines indicate the 1:1 slope. Tracers are colored by pressure level as indicated in the colorbar.

4.3 Carbon fluxes

Influences on surface pCO$_2$ may be broken into four main drivers: changes in temperature, salinity, DIC and Alk. These were quantified applying a Taylor expansion approach (see Chapter 3; *e.g. Metzl et al.* (2010)) where the change in each variable was taken as the difference of the surface value at a given Argo station and that of the previous station. The mean monthly changes in pCO$_2$ (dpCO$_2$) and its sensitivity to the 4 drivers are shown in Figure 4.10. In said figure, d$_{SST}p$CO$_2$, d$_{SSS}p$CO$_2$, d$_{DIC}p$CO$_2$, and d$_{Alk}p$CO$_2$ represent the sensitivity of pCO$_2$ to changes in temperature, salinity, DIC, and Alk in the surface ocean.

The variations in pCO$_2$ broadly follow a seasonal pattern, with drawdown of carbon in the productive season and increased pCO$_2$ in autumn and winter. This development is well documented (*Skjelvan et al.*, 1999; *Nakaoka et al.*, 2006; *Anderson et al.*, 2000; *Takahashi et al.*, 1993). It is generally attributed to consumption of carbon through photosynthesis in summer and spring, and subsequent increase in pCO$_2$ through fall due to mixing with carbon-rich waters from below. In line with these previous studies, it is clear from Figure 4.10 that dpCO$_2$ is governed by d$_{DIC}p$CO$_2$. Negative d$_{DIC}p$CO$_2$ in spring and summer is reflected in decreasing pCO$_2$ Figure 4.10a. The change in pCO$_2$ in these months is somewhat moderated
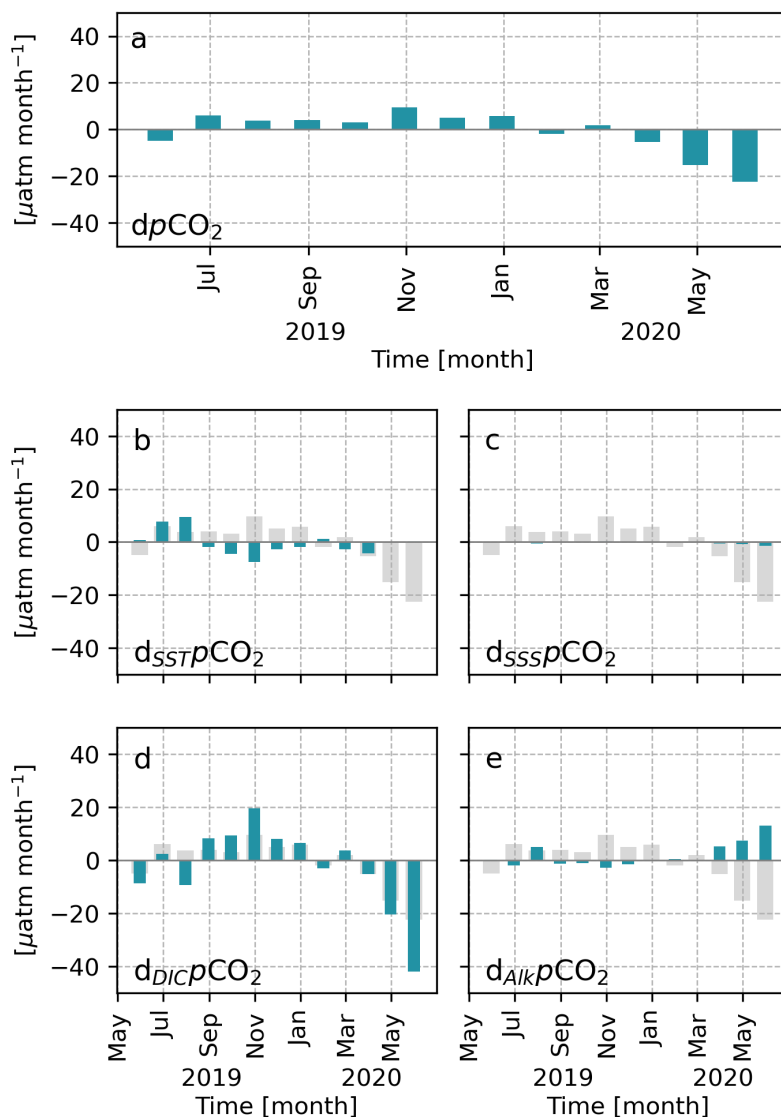
Figure 4.10: Observed monthly change in pCO_2 ($dpCO_2$) (a) and its main drivers: changes due to variations in temperature ($d_{SST}pCO_2$; b), salinity ($d_{SSS}pCO_2$; c), DIC ($d_{DIC}pCO_2$; d), and alkalinity ($d_{Alk}pCO_2$; e). $dpCO_2$ is shown in light gray in b-e for easy comparison.

by positive $d_{SST}pCO_2$ and $d_{Alk}pCO_2$.

The thermodynamic influence of temperature variations on $dpCO_2$ features a clear seasonal pattern caused by increasing temperatures in the summertime before surface waters cool from September to January. From March and onwards one would expect $d_{SST}pCO_2$ to be positive and counteract the presumably biologically driven drawdown in DIC. However, due to the influence of cold, fresh polar water advected in, we instead see a negative effect on $dpCO_2$.

Alk appears to have little influence on $dpCO_2$ during most of the annual cycle. As polar water rich in dissolved minerals is advected in, and phytoplankton blooms commence, Alk increases. The consumption of nitrate during photosynthesis increases Alk as the total concentration of weak acids is reduced. This also increases the water's capability to hold CO_2, leading to positive values of $d_{Alk}pCO_2$.
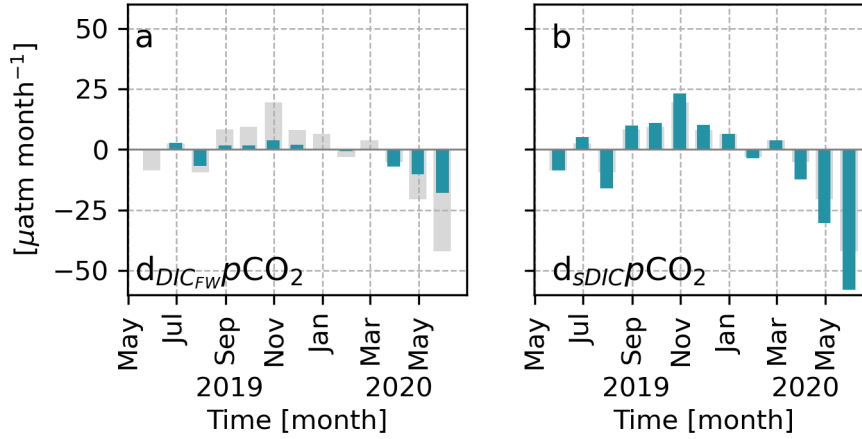
Figure 4.11: Expected change in $p\mathrm{CO}_2$ caused by freshwater effects on DIC (a; $\mathrm{d}_{\mathrm{DIC_{FW}}}p\mathrm{CO}_2$) and physical and biological effects on DIC (b; $\mathrm{d}_{s\mathrm{DIC}}p\mathrm{CO}_2$). Total expected change in $p\mathrm{CO}_2$ caused by DIC is shown in light gray.

The impact of salinity is negligible compared to the other drivers. The small expected impact of salinity on surface $p\mathrm{CO}_2$ has also been found for other areas such as the East Greenland Current, Irminger Basin, Iceland Basin, the North Sea (*Olsen et al.*, 2008), and the North Atlantic Subpolar Gyre (*Metzl et al.*, 2010; *Fröb et al.*, 2019).

Of the four main drivers, *Takahashi et al.* (1993), like this work, found that temperature and DIC variability were the main drivers of $\mathrm{d}p\mathrm{CO}_2$ in the Greenland Sea. The temperature dependence is well established (*Takahashi et al.*, 1993). Thus, to uncover the full set of drivers of $\mathrm{d}p\mathrm{CO}_2$ it is necessary to decompose $\mathrm{d}_{\mathrm{DIC}}p\mathrm{CO}_2$ into its underlying forcings: changes in salinity ($\Delta\mathrm{DIC_{FW}}$), biology ($\Delta\mathrm{DIC_{F_{BIO}}}$), vertical transport ($\Delta\mathrm{DIC_{F_z}}$), and air-sea gas exchange ($\Delta\mathrm{DIC_{F_{GE}}}$).

Freshwater impacts on DIC can be accounted for explicitly using Taylor expansion as above. This method entails splitting $\mathrm{d}_{\mathrm{DIC}}p\mathrm{CO}_2$ into a component reflecting changes in salinity ($\mathrm{d}_{\mathrm{DIC_{FW}}}p\mathrm{CO}_2$) and a salinity normalized component ($\mathrm{d}_{s\mathrm{DIC}}p\mathrm{CO}_2$; reference salinity $= 35$), as previously done by *e.g.* *Fröb et al.* (2019). $\mathrm{d}_{\mathrm{DIC_{FW}}}p\mathrm{CO}_2$ contains the effect of dilution by precipitation and other processes. $\mathrm{d}_{s\mathrm{DIC}}p\mathrm{CO}_2$ is the remaining change caused by physics and biology, *i.e.* the sum of the effect of $\Delta\mathrm{DIC_{F_{BIO}}}$, $\Delta\mathrm{DIC_{F_z}}$, and air-sea gas exchange $\Delta\mathrm{DIC_{F_{GE}}}$ on $p\mathrm{CO}_2$. See Chapter 3 for details on the calculation of these.

The monthly contribution of $\mathrm{d}_{\mathrm{DIC_{FW}}}p\mathrm{CO}_2$ and $\mathrm{d}_{s\mathrm{DIC}}p\mathrm{CO}_2$ is show in Figure 4.11. $\mathrm{d}_{\mathrm{DIC_{FW}}}p\mathrm{CO}_2$ contributes to $\mathrm{d}p\mathrm{CO}_2$ on a scale comparable to Alk (Figure 4.10e), though in the opposite direction. It is evident that the physical and biological processes represented by $\mathrm{d}_{s\mathrm{DIC}}p\mathrm{CO}_2$ govern the DIC variability influencing $\mathrm{d}p\mathrm{CO}_2$. The effect of freshwater is therefore neglected when considering the drivers of $\mathrm{d}_{\mathrm{DIC}}p\mathrm{CO}_2$. The total change in surface DIC ($\Delta\mathrm{DIC}$) is then reduced to

$$\Delta\mathrm{DIC} = \Delta\mathrm{DIC_{F_z}} + \Delta\mathrm{DIC_{F_{GE}}} + \Delta\mathrm{DIC_{F_{BIO}}} \tag{4.1}$$

These components are further explored in the following subsections.

4.3.1   Vertical transport of carbon: ΔDIC_{F_z}

Vertical transport in the PWP model is split into three processes: mixed layer deepening by static instability (StIn), by bulk Richardson number relaxation (BRi), and by gradient Richardson number relaxation (GRi). Each process mixes up tracers from the bulk fluid below. StIn looks for static instability starting at the surface box of the model. For each statically instable box it encounters, the mixed layer is deepened by one box and density is mixed. The deepening stops once a statically stable box is reached, at which point all the other tracers are mixed according to a bulk mixing formula. BRi represents wind driven deepening of the mixed layer. This mixing step starts at the base of the mixed layer and uses the velocity differences between the bulk mixed layer and the region below to determine mixed layer instability. A bulk Richardson number threshold is used to determine if stability is reached. For each unstable box, the mixed layer is deepened by one box and all tracers are mixed according to the same method applied to StIn. Finally, GRi smooths the sharp gradient at the base of the mixed layer produced by BRi. This process starts in the transition region at the base of the mixed layer. Like BRi, it is a wind driven process whereby shear is used to determine instability. Here, only partial mixing occurs in the boxes determined to be unstable. More details on the mixing processes are found in Section 3.5.

The total vertical transport into the mixed layer is governed by StIn (*i.e.* free convection). In total, StIn accounts for 12.4 of 15.1 g C m^{-2} y^{-1}. BRi and GRi contribute 2.1 and 0.6 g C m^{-2} y^{-1} respectively, with uncertainties of 15%. Qualitatively, this agrees well with previous work on the Greenland Sea (*Brakstad et al.*, 2019). The total vertical flux is somewhat higher than the 11 g C m^{-2} y^{-1} estimated by *Anderson et al.* (2000) using a box model.

Figure 4.12a-c show the change in mean daily inventory of DIC (ΔDIC) associated with each mixing process, and the sum of these (Figure 4.12d). ΔDIC is shown both for the surface box (p=0 dbar) and integrated over mld$_{mix}$ (Σmld). The surface box is one meter deep, and the inventories correspond to concentions (1 mmol m^{-3}==1 µmol kg^{-1}). Figure 4.12e-h show the mean daily mixed layer (mld$_{mix}$) in terms of the deepest point of mixing associated with each mixing process. This is not the same as the mixed layer depth as calculated by the Nilsen method, which calculates mixed layer depth as the region of relative homogeneity and does not reflect which depths actually partake in mixing. For each timestep, mld$_{mix}$ is taken as the deepest point at which a change in mass has occurred due to one of the three mixing processes. The dotted line in Figure 4.12h is the calculated mixed layer depth of the model when calculated from the T and S profiles using the Nilsen method.

The total transport of DIC into the mixed layer is almost always positive (Figure 4.12d), but there is an instant of negative total Σmld in December. The negative flux coincides with the start of the convective season when the water has cooled sufficiently to mix significantly deeper than before. It is caused by BRi, indicating the transport occurs at the base of the mixed layer. The negative value must be caused by lower concentrations of DIC being mixed up. Vertical transport only leads to a net increase in mixed layer carbon content in the months December to late February. This is the period of deepest mixing. For periods of shallow mixing there is no net change in carbon content caused by vertical transport.

StIn draws small amounts of carbon out of the surface box through most of winter. Since Σmld is positive, however, the fate of this subducted carbon must be within the mixed layer. The same is true for BRi. BRi has a stronger influence on surface ΔDIC than GRi. This is
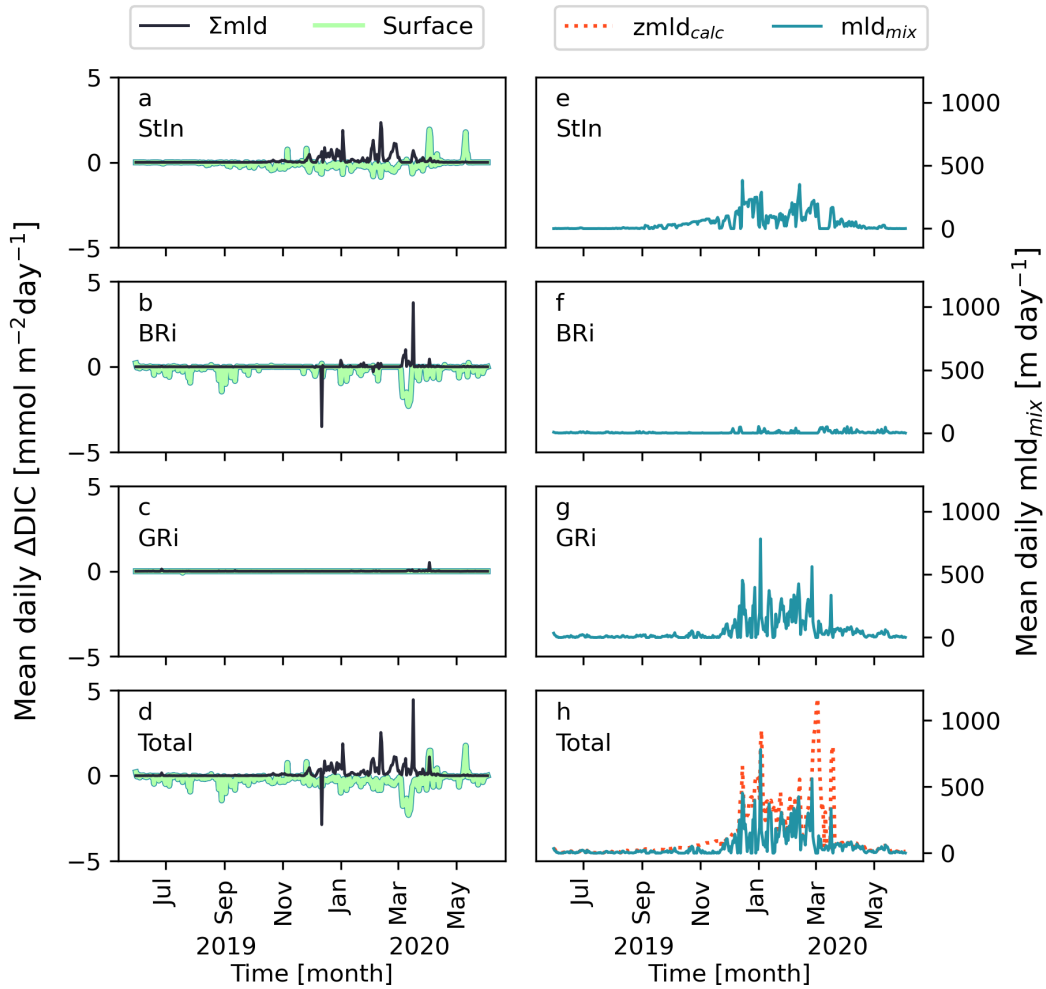
Figure 4.12: Mean daily change in DIC as a result of vertical transport induced by static instability (StIn; a), bulk Richardson number instability (BRi; b), gradient Richardson number instability (GRi; c) and the sum of the three (Total; d) are displayed on the left hand side. The values are calculated for the surface box (light green line) and summed over the mixed layer (black line). The right hand side (e-h) shows the mean daily mixing depth caused by the same mechanisms. Panel h also shows the mixed layer depth calculated by the Nilsen method (zmld$_{calc}$; dashed red line). Mixing depth is the depth to which actual mixing occurs, while the mixed layer depth calculated by the Nilsen method is the depth of the near-homogeneous mixed layer as defined in Section 2.4.

due to a step in the model algorithm which mixes the entire mixed layer. This step does not exist for GRi as it merely smooths the base gradient and therefore only affects the surface if the mixed layer is extremely shallow. One would assume that there is a positive flux into the surface in winter as DIC-rich water is mixed up from below the pycnocline.

The mixing depths (mld_{mix}) show that StIn causes mixing down to 300-400 dbar. The BRi deepening process starts at the base of the mixed layer. It appears to work mostly at shallow depths. The GRi mixing process also starts at the base of the mixed layer. From Figure 4.12g it is clear that this process is most active when the mixed layer is deeper. As it works to smooth the gradient at the base of the mixed layer created by the StIn and BRi mixing processes, it is expected that mixing in this process occurs at the deepest pressure levels. It is also expected that this process contributes the least to transport of DIC both into the mixed layer, and into the surface box.

It is important to note the difference between mld_{mix} and $\text{zmld}_{\text{calc}}$. The latter is only used to calculate the mixed layer depth as defined by the Nilsen method using temperature and salinity from the model profiles. When calculated within the model it never invokes mixing - it is always calculated at the end of a timestep. As such, it represents the concept of a *relatively* homogeneous layer as discussed in Chapter 2. mld_{mix} reflects the depth to which mixing actually occurs in the model. It is shallower than $\text{zmld}_{\text{calc}}$ because concentrations below mld_{mix} are homogeneous enough that variations are within the threshold set by the Nilsen method. Yet, there are variations above $\text{zmld}_{\text{calc}}$ that exceed the instability thresholds of the model's mixing criteria. It can therefore be argued that while $\text{zmld}_{\text{calc}}$ is a good metric for model validation, it is not necessarily a correct indication of the actual depth to which mixing takes place.

4.3.2 The effect of air-sea gas exhange on DIC: $\Delta\text{DIC}_{\text{F}_{\text{GE}}}$

While the vertical transport of carbon redistributes the element through the water column, air-sea gas exchange is a source or sink of oceanic carbon. As described in Chapter 2, gas exchange is strongly dependent on wind speed, $\Delta p\text{CO}_2$, and solubility (*i.e.*, temperature). The mean daily flux of CO_2 from air-sea gas exchange (F_{GE}) is presented with these drivers in Figure 4.13.

Air-sea gas exchange is directed into the ocean during most of the annual cycle. Strong uptake of carbon in summer and fall is explained by the DIC deficit caused by biological production, leading to a strongly undersaturated water phase. This is clear from the large $\Delta p\text{CO}_2$ in Figure 4.13b.

Between November and March there is some outgassing, despite low temperatures and strong winds. This is because $p\text{CO}_2^{\text{oc}}$ has increased sufficiently that the surface water is supersaturated. Air-sea gas exchange is relatively constant through autumn because the reduction in undersaturation (Figure 4.13b) is compensated by increasing wind speed (Figure 4.13c).

Carbon outgassing in winter despite strong forcing should indicate a positive vertical transport increasing surface $p\text{CO}_2^{\text{oc}}$ and reducing the air-sea $p\text{CO}_2$ gradient. However, as seen in the previous section, this does not appear to be the case. There is a net positive transport of carbon into the mld in winter, yet a net loss from the surface. From the development of
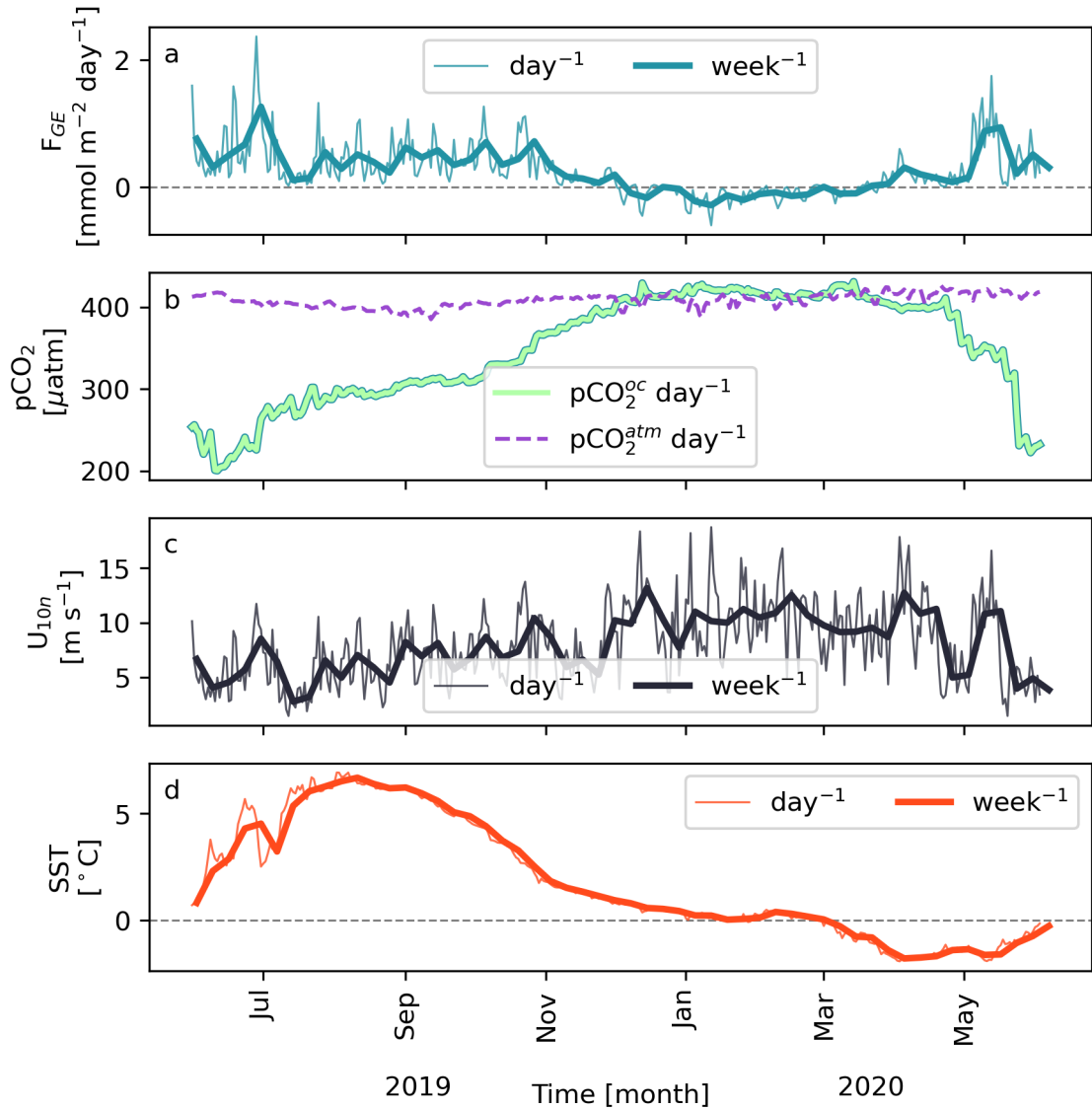
Figure 4.13: Mean daily (thin lines) and weekly (thick lines) values of air-sea flux of CO_2 (a; positive gas fluxes are directed into the ocean, indicating CO_2 uptake), pCO_2^{oc} and pCO_2^{atm} (b), second moment of 10 m neutral winds (c), and sea surface temperature (SST) (d).

pCO_2^{oc} in Figure 4.13b it is evident that the negative transport out of the surface must be so small that the increasing pCO_2^{oc} introduced by each reinitialization in the model is not counteracted.

The total yearly air-sea gas transfer for the time period was 27±27% g C $m^{-2}y^{-1}$. It is displayed in Table 4.2 together with values obtained in other studies, their study period, and the number of winter observations included in their studies. F_{GE} is within the lower range of estimates found in literature, comparable to the 27±10 and 25-50 g C $m^{-2}y^{-1}$ calculated by *Arrigo et al.* (2010). Others have obtained fluxes in the range 48-55 g C $m^{-2}y^{-1}$ (*Hood et al.*, 1999; *Anderson et al.*, 2000; *Nakaoka et al.*, 2006; *Yasunaka et al.*, 2016), and even up to 71 g C $m^{-2}y^{-1}$ (*Skjelvan et al.*, 1999). *Manizza et al.* (2013) obtained a value of 10 g C $m^{-2}y^{-1}$. There are several possible reasons for these differences: gas exchange parameterization, biases towards summer measurements, and definitions of the Greenland

Sea.

Table 4.2: Yearly CO_2 flux into the surface ocean of the Greenland Sea as calculated by previous authors and this work.

Source	Yearly CO_2 flux [g C m^{-2}y^{-1}]	Study period	No. of winter observations	Method
Hood et al. (1999)	55	1996-1997	0 (0%)	Drifting buoy and regression analysis
Anderson et al. (2000)	53±4	1993-1997	2 (14%)	Cruise data and box model
Nakaoka et al. (2006)	52±20	1992-2001	1 (20%)	Unknown number of profiles, 5 cruises in total.
Arrigo et al. (2010)	27±10	1998-2003	-	Remote sensing and model
Manizza et al. (2013)	10	1996-2007		Biogeochemical 3-D model
Yasunaka et al. (2016)	48	1997-2013	-	Self-organizing map
This work	27±27%	2019-2020	21 (28%)	Autonomous profiler and 1-D model

The choice of gas transfer velocity parameterization and wind speed products can influence the gas flux estimates. The authors cited from 2006 and earlier employ a parameterization by *Wanninkhof* (1992) in which ^{14}C estimates were higher. It assumes k is proportional to $0.31U^2$. Now, the recommended parameterization is based on lower global ^{14}C inventories and an optimized coefficient scaled to account for differences in wind speed products. The calculated fluxes of *Hood et al.* (1999), *Anderson et al.* (2000), and *Nakaoka et al.* (2006) may therefore be too high. *Arrigo et al.* (2010) and *Yasunaka et al.* (2016) both employ the revised parameterization, as in this work. Because the wind product chosen is accounted for within the k parameterization, differences between their results and this work should not be caused by different wind speed products. *Manizza et al.* (2013) cite a bulk parameterization by Large and Yeager (2004), the contents of which this author is unaware. It is likely that this parameterization causes some of the discrepancies between their results and others, as is is published before the work of *Sweeney et al.* (2007) and *Naegler et al.* (2006), and thus prior to the *Wanninkhof* (2014) revision.

There is a general lack of wintertime data in the cited works. (*Hood et al.*, 1999) built a flux map from buoy measurements with no wintertime data. Winter measurements are also underrepresented in *Anderson et al.* (2000),*Nakaoka et al.* (2006),*Manizza et al.* (2013), and *Yasunaka et al.* (2016). *Arrigo et al.* (2010) used model output and satellite data as a basis for calculating their pCO$_2^{oc}$. They do not report temporal bias in this underlying data. Thus, only this work, and possibly *Arrigo et al.* (2010), capture the development of pCO$_2^{oc}$ in winter.

If flux maps are created based on summer-biased data, such as in *Hood et al.* (1999), *Nakaoka et al.* (2006), and *Yasunaka et al.* (2016), it is possible that the increased surface$p$CO$_2^{oc}$ due to wintertime mixing is not captured to a sufficient extent. This could explain the fact that these authors found the strongest air-sea gas fluxes in winter, and that their estimates are higher than those obtained in this work. On the other hand, neglecting spatial variability as in this work, also leads to inconsistencies. This is evident from the end of the time series observed in *e.g.* Figure 4.2 where the intrusion of polar water is clear. This advection has ramifications for the results herein, and shows the fragility of assuming horizontally homogeneous conditions with no lateral advection.

The low value obtained by *Manizza et al.* (2013) could be related to their definition of

the Greenland Sea, as they included the entire Nordic Seas and the Irminger Sea. Spatial variations within this zone could lead to a falsely low air-sea flux. *Arrigo et al.* (2010) used a similar definition. While their estimate is in the lower range of the cited works, it is not as extreme as that of *Manizza et al.* (2013). *Yasunaka et al.* (2016) also expanded the traditional definition of the Greenland Sea. They included the Norwegian Sea. They found lower pCO_2^{oc} in the Greenland Sea than the Norwegian Sea. Their total flux of 48 g C m^{-2}y^{-1} for the combined regions is therefore probably a little lower than it would be for only the Greenland Sea.

Interannual variability in wind speed, mixed layer depth, and sea ice cover will also vary between the sources cited. The range of methods used gives emphasis to the challenge involved with estimating air-sea gas exchange.

4.3.3 Biologically induced changes in DIC: $\Delta DIC_{F_{BIO}}$

Argo observations capture both the physical and biological processes affecting DIC variability. The PWP model isolates the physical processes. Thus, biology may be calculated as the differencec between the two datasets. As this difference captures all biologically induced changes in DIC, it is taken as a measure of net community production (NCP). The evolution of DIC derived NCP is shown in Figure 4.14. Maximum and minimum NCP were 4.6 and -5.8 mmol C m^{-3} day^{-1} respectively, however the figure is adjusted to better illustrate the variability in the more typical values. Positive values indicate biological production and negative imply remineralization.
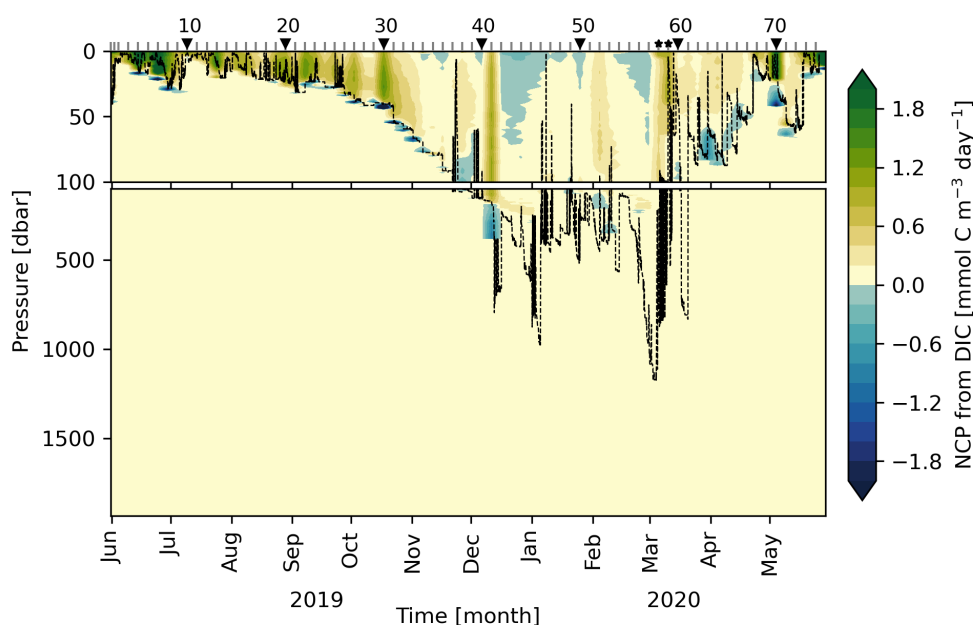

Figure 4.14: Hovmöller diagram of NCP calculated from the DIC model drift compared to Argo measurements. The dashed black line is the modelled mixed layer depth. The black, numbered triangles indicate every 10th Argo profile. Gray, vertical lines indicate reinitializations. Negative values (blue scaled) indicate remineralization, positive values (yellow to green scaled) indicate biological production. Two stars show where freshwater was added to account for polar water advection.

The seasonal pattern is well resolved, with strong production in the upper 20 dbar from June to August 2019. From mid-March, production slowly intensifies towards the end of the timeseries. NCP below the mixed layer is constantly low and positive, around 0.06 mmol C m^{-3} day^{-1} . It is not realistic for production to occur at these depths. Here, one would instead expect some remineralization, but the values are well within the range of uncertainty. The constant positive values could be a numerical artifact, or caused by drift in the pH sensor. At the base of the mixed layer, some instances of negative NCP occur. These may be caused by internal waves or eddies which vertically displace the density surfaces the Argo floats through, leading to oscillations in the measured values. Alternatively, they could be real signs of remineralization. The possible presence of internal waves or eddies is explored in Section 5.2.4.
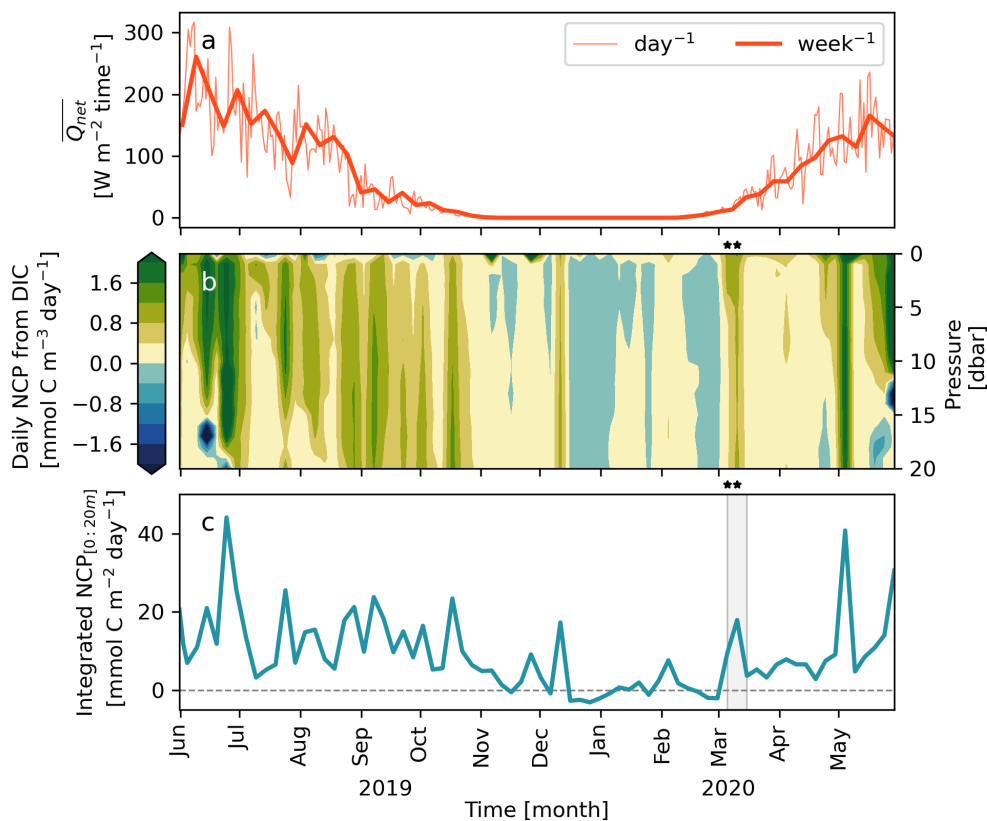

Figure 4.15: a) Mean shortwave radiation ($\overline{Q_{net}}$) over a day (thin line) and a week (thick line). b) Daily NCP in the euphotic zone (0-20 dbar). Positive values (yellow to green) indicate biological production and negative values (shades of blue) show remineralization. c) NCP depth-integrated over the euphotic zone (upper 20 dbar). The two stars above b and c show reinitializations after which additional freshwater has been added to simulate advection of polar water. The shaded region in c shows the same.

To avoid the influence of overestimated NCP at depth and the possible influence of internal waves at the base of the mixed layer, a euphotic depth of 20 dbar is assumed. Figure 4.15 shows shortwave radiation, NCP in the said euphotic zone, and total NCP in the euphotic zone. As shortwave radiation declines towards winter, the biological activity slowly ceases. From November, there is a small amount of biological production interspersed with events of weak remineralization. The prescribed freshwater advection in March results in a small,

erroneous bloom. Integrated NCP shows peak productivity in late June 2019 and in May 2020. At these times, NCP exceeds 40 mmol C m^{-2} day^{-1}. While productivity appears to be somewhat overestimated from September through October, the values *could* reflect real production. This is not the case for the peak seen in December. The December peak must derive from internal variability, or by sensor instability. Sensor stability is examined inSection 5.2.2.

Annual NCP (ANCP) in the euphotic zone is 39 g C m^{-2} y^{-1} (3.2 mol C m^{-2} y^{-1}). The value is somewhat higher than *Anderson et al.* (2000)'s box model estimate of 34 g C m^{-2} y^{-1}.

4.3.4 Determination of dominant drivers of DIC variability

The previous subsections detailed each of the four identified drivers of DIC variability. However, it is the DIC concentrations in the surface that influence pCO_2 and gas exchange. Parcels within the mixed layer circulate through its entire depth such that a parcel at the bottom will come in contact with the surface and *vice versa*. To best interpret the effects that changing DIC concentrations have on surface pCO_2, it is therefore reasonable to evaluate the total change in the upper 20 dbar. This range is well-mixed through nearly the entire annual cycle, yet shallow enough to exclude depths affected by possible internal waves and eddies. Figure 4.16 shows the monthly change of DIC in the upper 20 dbar caused by F_{F_Z}, F_{GE}, and F_{BIO}, as well as the net change.
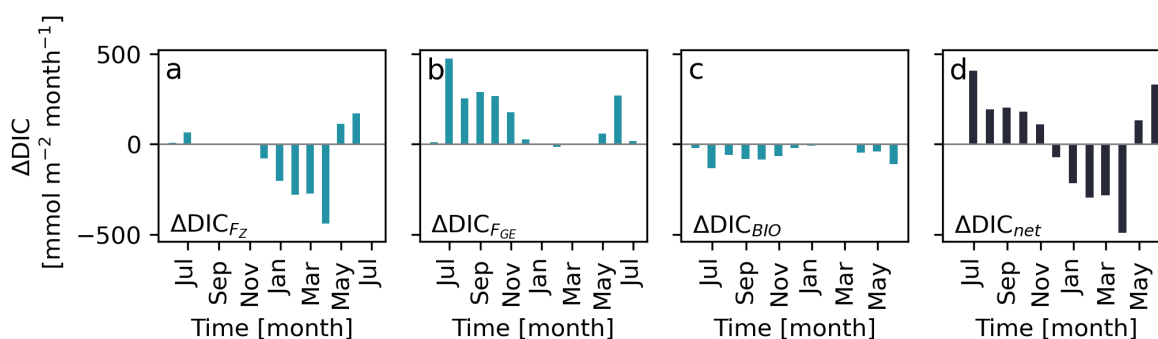

Figure 4.16: Monthly change in DIC in the upper 20 dbar caused by F_{F_Z} (a; ΔDIC_{F_Z}), F_{GE} (b; $\Delta DIC_{F_{GE}}$), and F_{BIO} (c; $\Delta DIC_{F_{BIO}}$). Net change is shown in d. Positive values indicate a net loss of DIC in the upper 20 dbar, positive values indicate a net gain of DIC.

Surface ΔDIC is governed by vertical transport in winter, and air-sea gas exchange in summer. Biology is less important. This could be interpreted as biology enhancing an already existing undersaturation, increasing air-sea gas exchange. Air-sea gas exchange and biology have opposing effects on net ΔDIC, resulting in more moderate positive values. Modelled vertical transport in the upper 20 dbar is negative from November to May. This was seen in Section 4.3.1. The finding is not realistic. The negative flux should give rise to higher $\Delta DIC_{F_{GE}}$, but because of the strong rectifying effect of model reinitalization, $\Delta DIC_{F_{GE}}$ estimates are within reason. It is possible that the mixing scheme of the model is not sufficiently refined for the small-scale analysis carried out in this work. Other applications have not generally scrutinized the predicted vertical transport at the level of individual stability criteria.

Chapter 5

Discussion

In this section I discuss how different parameterizations affect the model, and look into some of the unexpected findings from Chapter 4. The first part entails the sensivity of the model to advection and ice parameterizations. The second part covers other methods of calculating NCP, the suspected sensor drift, the changed mixing shceme, and the observation of possible internal waves and eddies.

5.1 Model sensitivities

5.1.1 Advection

There are many sources of uncertainty within the PWP model. In order to obtain an estimate of the uncertainty associated with predicted vertical fluxes, one can look at how they respond to changes in some of the parameterizations made. Ideally, one would adjust as many adjustable paramters as possible and evaluate model response, but due to time limitations I focus on what is considered by Brakstad to be the greatest source of uncertainty: the parameterization of heat and salt.

The parameterized advection of heat and salt is based on means from 1986-2016. The heat loss in winter through this period is compared to the observed heat content in the region. Advection is then used to close this budget. As explained in Section 3.5.1.9, the vertical structure of the advected properties is based on the difference in mean profiles within the gyre compared to mean profiles of the immediate surrounding water masses (*Brakstad et al.,* 2019). The result is idealized advection profiles, with constant values. In reality, we do not know the variability in the amount of heat and salt advected, nor the real advected vertical structure. As stated above, this is considered a major source of uncertainty (ref. conversation with Brakstad). A sensitivity analysis was applied to evaluate the impact of the total magnitude of advection on model results.

The sensitivity analysis involves 5 cases:

- **Base case**: advection follows *Brakstad et al.* (2019) as described in Chapter 3

- **Increased heat advection**: The annual heat advected is increased by 10%

- **Reduced heat advection**: The annual heat advected is reduced by 10%

- **Increased salt advection**: The monthly salt advected is increased by 10%

- **Reduced salt advection**: The monthly salt advected is reduced by 10%

The main metrics resulting from these cases are tabulated in Table 5.1. In general, the results are surprisingly robust to adjustments in the magnitude of advected heat and salt. This is because the model is strongly constrained by the reinitialization to every Argo profile. Vertical transport is the most sensitive component to alterations in advection. Reduced vertical transport is the major effect, and this drives the changes seen in biogeochemistry. Increased heat advection strengthens stratification because more heat loss is required for convection to occur, which is the reason for reduced F_Z in Heat+10%. But why does intensified salt advection not lead to deeper mixed layers and stronger vertical fluxes of DIC? To understand this, we must remember the vertical structure of the advection profile. At the surface, it imitates advection of polar water, which is relatively fresh. Below, saltier water is advected to mimic Atlantic water. Consequently, reducing advection of salt actually increases the surface freshening and increases stratification at the surface. Conversely, reducing salt advection leads to reduced surface stratification, but also lower salinity within 500-100 dbar compared to the base case. It is curious that the reduction in heat advection does not lead to increased mixing. This could be caused by non-linearities in the model. Further analysis is required to understand this effect better.

Table 5.1: Mean mixed layer depth (MLD), net vertical transport of DIC (F_Z), net air-sea gas exchange flux of DIC (F_{GE}), and net biological flux of DIC in the upper 20 m ($F_{bio}^{z=[0:20]}$) for 5 experiments. "Base" applies advection as parameterized by (*Brakstad et al.*, 2019). "Heat+10%" and "Heat-10%" are runs where the base advection of heat is increased and decreased by 10% respectively. "Salt+10%" and "Salt-10%" are runs where the base advection of salt is increased and decreased by 10% respectively.

	Mean MLD [m]	Net F_z [mol C m^{-2} y^{-1}]	Net F_{GE} [mol C m^{-2} y^{-1}]	Net $F_{bio}^{z=[0:20]}$ [mol C m^{-2} y^{-1}]
Base	138.0	1.26	2.25	3.23
Heat +10%	131.9 (-4.4%)	1.21 (-4.0%)	2.26 (+0.4%)	3.20 (-0.9%)
Heat -10%	136.9 (-0.8%)	1.21 (-4.0%)	2.25 (-0.0%)	3.21 (-0.6%)
Salt +10%	134.7 (-2.4%)	1.06 (-15.9%)	2.25 (-0.0%)	3.25 (+0.6%)
Salt -10%	134.3 (-2.7%)	1.16 (-7.9%)	2.26 (+0.4%)	3.22 (-0.3%)

Shallower mixed layers for all cases compared to the base case is a manifestation of the reduced vertical transport. Both F_{GE} and $F_{bio}^{z=[0:20]}$ appear relatively insensitive to changes in vertical transport. The former could be connected to the negative vertical transport of DIC at the surface seen in Chapter 4 being rectified at each reinitialization. It is likely that the

negative flux is so small that pCO_2^{oc} is never reduced sufficiently to impact F_{GE} to a great extent before it is adjusted to the higher pressure estimated from the Argo float observations. It is therefore not sensitive to small changes in F_Z. Both biology and F_{GE} are calculated based on surface values. Analysis of how the vertical fluxes specifically in the surface change with the various parameterizations of advection is therefore needed, however due to time limitations this is left for future work.

To interpret the differences in vertical transport seen between each case, mixed layer depth is plotted as a proxy for mixing in Figure 5.1. Individual differences in mixing terms are too small to gain an understanding of this visually.
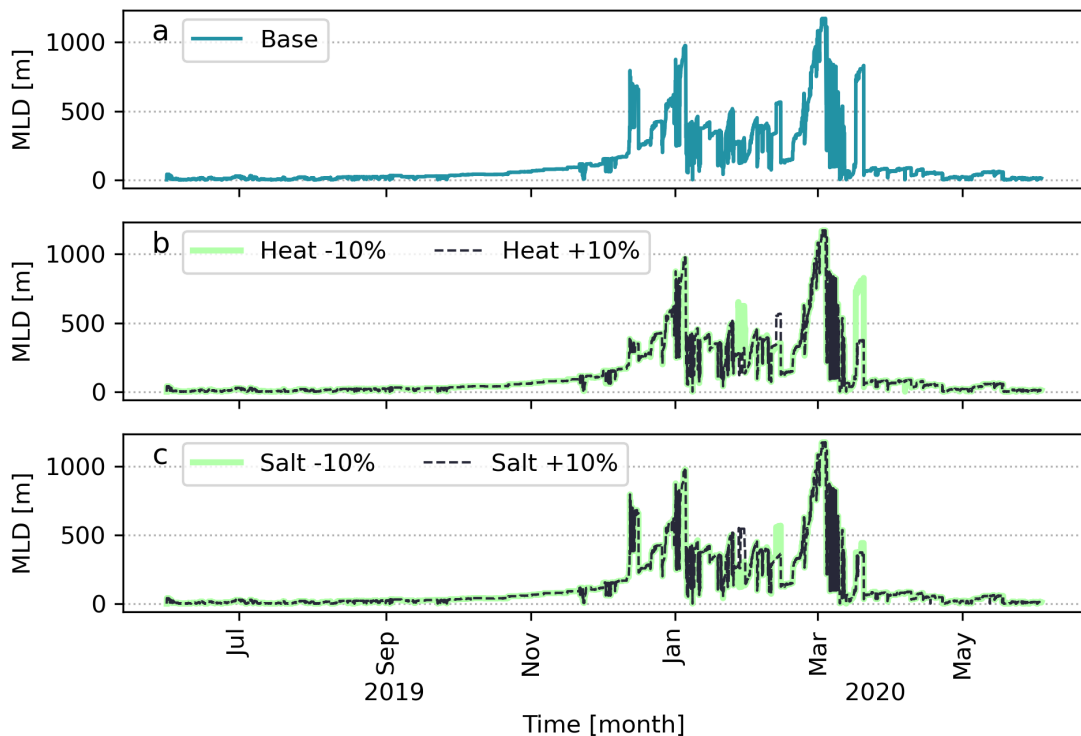

Figure 5.1: Mixed layer depth (MLD) for the base case (a), $\pm 10\%$ heat advection (b), and $\pm 10\%$ salt advection (c). Reduced advection cases are shown in thick, solid, light green lines. Increased advection cases are shown in dashed black lines.

Figure 5.1 shows that the magnitude of advection matters little in the months before deep mixing sets in. The first peak in mixed layer depth in the base case occurs in the beginning of December. Adjusting heat advection results in approximately halved mixed layer depth at this time compared to the base case. It is unclear why this also occurs for Heat-10%. Both salt cases produce MLD comparable to the base case in December. The mixed layer evolves equally for all cases from the end of the December peak to the end of January.

January is a period of highly variable mixed layer depth for all cases. At the end of the month, Heat-10% and Salt+10% both produce deeper mixed layers than the base case. The reduced heat input here leads to a MLD of approximately 600 dbar, compared to the 250 dbar produced in the base case. Strengthened salt advection results in a MLD of 500 dbar. The Salt+10% peak implies that surface forcing has cooled the extra fresh surface layer so much that mixing with the extra salty layer below is enabled. Fresher water in the surface does not lead to extra cooling in itself, however more heat loss is required for the water to

reach densities that will break down stratification. At the time of convection, less saline water will therefore be cooler than more saline water given equal conditions below the mixed layer.

At the beginning of February, there is a short period of shoaling before the main deepening period initiates. Here, Heat-10% and Salt+10% commence the shoaling process somewhat earlier than the other cases. Mixed layer deepening occurs similarly for all cases during the main deepening stage. Shortly after March 1st, advection of polar water is prescribed, surpressing mixing for the duration of two Argo cycles. Following this, the base case features one last deep mixing event. This event is amplified in Heat-10%. All other cases produce significantly shallower MLD. This indicates the water mass at this point in time is stratified in temperature, such that reducing heat advection results in a slightly cooler water mass which breaks down the temperature stratification. As spring progresses and the water column restratifies, all cases behave in a similar manner.

From Figure 5.1 it is clear that the adjustment of advection does not produce unduly different results overall. There are merely a few convection events in which the mixed layer development occurs differently between the modelled cases. The results for carbon in terms of vertical fluxes, air-sea gas exchange, and resulting biology are robust to changes in advection.

5.1.2   Ice

Brine rejection from ice production has historically been regarded as an important pre-conditioning mechanism for convection in the Greenland Sea (*Visbeck et al.*, 1995). It is therefore included in this version of the PWP model. Ice cover also affects gas exchange as it is a barrier between the surface ocean and the atmosphere. There are several ways to parameterize this effect. In Section 4.3 I assume that the thin ice cover produced is so fragmented that gas exchange can proceed as normal, at a 100% rate. The assumption is made because the model never produces more than 1 cm ice and it is assumed newly produced ice is immediately transported out of the gyre. The magnitude of ice production in the model mirrors low sea ice concentrations from ERA5 data. With ERA5 ice concentrations well below 1%, the assumption of a fragmented ice cover is supported. However, the onset of ice production differs between the model and ERA5. This is shown in Figure 5.2. Note that one can not be certain that the ice cover in the ERA5 data is produced within the Greenland Sea. It could also have been advected from the North.

Modelled ice production starts in April. Ice onset in ERA5 coincides with the second modelled production period. ERA5 sea ice concentrations then peak in the start of June. Note that the magnitude of the two datasets is not directly comparable. Sea ice production by the model is given in cm h^{-1} whilst the sea ice concentration from ERA5 is in %. Both datasets do show that ice cover in the considered period is very low.

To assess if the assumption of 100% gas exchange rate during periods of ice cover is reasonable, the model's response to two other parameterizations is tested. In one case, I assume there is no gas exchange (0%) when the model produces ice. In the other case, I ignore the model ice. Instead, I scale gas exchange by the ERA5 sea ice concentration (*Fay et al.*, 2021):

$$\mathrm{F}_{\mathrm{CO_2}} = k_{\mathrm{CO_2}} K_{\mathrm{CO_2}} (p\mathrm{CO}_2^{\mathrm{atm}} - p\mathrm{CO}_2^{\mathrm{oc}})(1 - SIC) \tag{5.1}$$
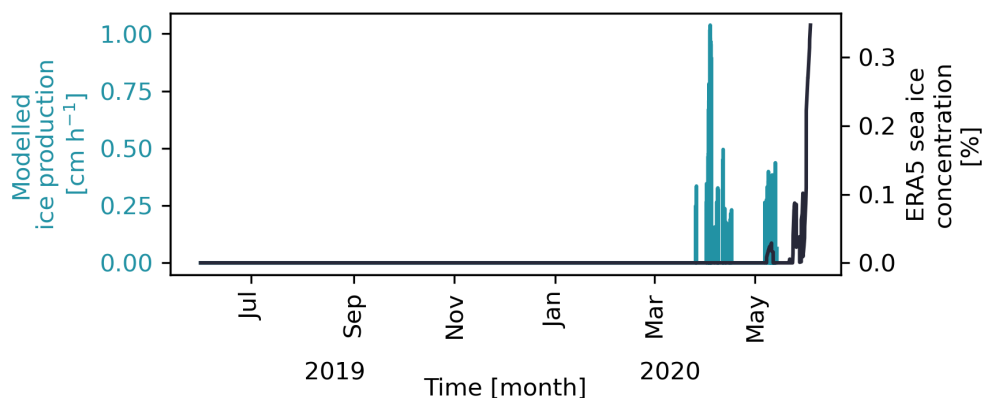
Figure 5.2: Timeseries from June 2019 to June 2020 showing modelled ice production (left axis, blue line) and ERA5 sea ice concentrations (right axis, black line). Note the different units of the two axes.

Here, SIC denotes sea ice concentration. The resulting net yearly CO_2 gas exchange flux is 2.22 mol m^{-2} y^{-1} (26.7 g C m^{-2} y^{-1}) and 2.24 mol m^{-2} y^{-1} (26.9 g C m^{-2} y^{-1}) for the 0% and ERA5-scaled cases respectively. This corresponds to reductions in gas exchange of 1.3% and 0.4%, *i.e.*, well within the range of uncertainty for the gas exchange calculation.

While the 2019/2020 season was one of scarce sea ice production in the Greenland Sea, this is not always the case. In terms of the model's applicability to other years, it is therefore interesting to look at the mechanisms causing the small gas exchange differences. Time series of CO_2 fluxes (mmol m^{-2} h^{-1}) into the mixed layer for each case are displayed in Figure 5.3.

Gas exchange in the 0% case (Figure 5.3b) exhibits stronger fluctuations in periods of ice production than the other two cases. This is because there are no consecutive timesteps of modelled ice production. At its most intense, this leads to bi-hourly events of 0% gas exchange interchanged with fluxes at normal levels. After a longer period of such fluctuations in May, pCO_2^{oc} drops slightly below the levels of the 100% gas exchange case, leading to slightly stronger gas flux at the time (see Figure A.1). Visually, there is no notable difference between the 100% gas exchange case and the ERA5-scaled fluxes. This is because the scaling imposed by ERA5 sea ice cover on air-sea gas exchange is extremely small.

Based on the above, the effect of gas parameterization under sea ice producing conditions is very small in this work. The effect on vertical fluxes and biology was negligble and is not shown here.
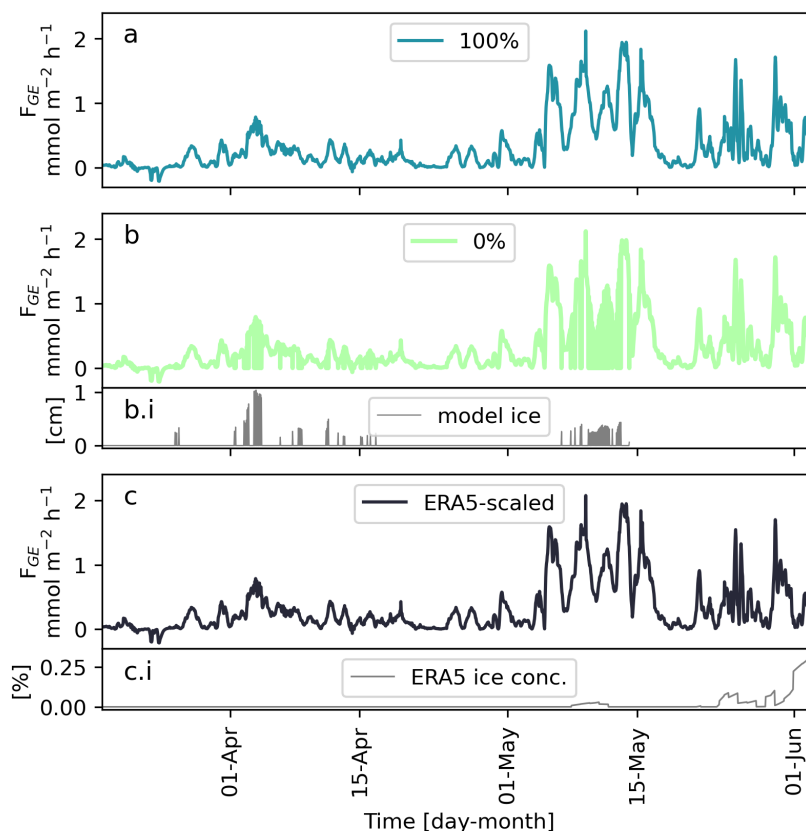
Figure 5.3: Timeseries of hourly gas exchange flux for three modelled cases from March 18th 2020 to June 3rd 2020. a) 100% gas exchange when ice is produced in the model. b) 0% gas exchange when ice is produced in the model. b.i) modelled ice production. c) gas exchange scaled by ERA5 sea ice concentrations. c.i) ERA5 sea ice concentrations. See Figure 5.2 for b.i and c.i in greater detail.

5.2 A further look at the results

5.2.1 Other methods of calculating biology

With a BGC-Argo float it is possible to derive the biological fluxes not only from DIC, but also from oxygen and nitrate. In the following subsections these methods are implemented and discussed. I also discuss the effect of different integration depths on the annual net community production estimates.

5.2.1.1 Oxygen derived NCP

Employing the PWP model and Argo profiles, NCP is derived from oxygen with the same method as NCP from DIC, except the air-sea gas exchange parameterization is somewhat different (Chapter 3). To convert the oxygen production from oxygen to units of carbon, a Redfield ratio of -106:150 was used, following *Anderson* (1995). The resulting daily NCP at all depths is shown in Figure 5.4.
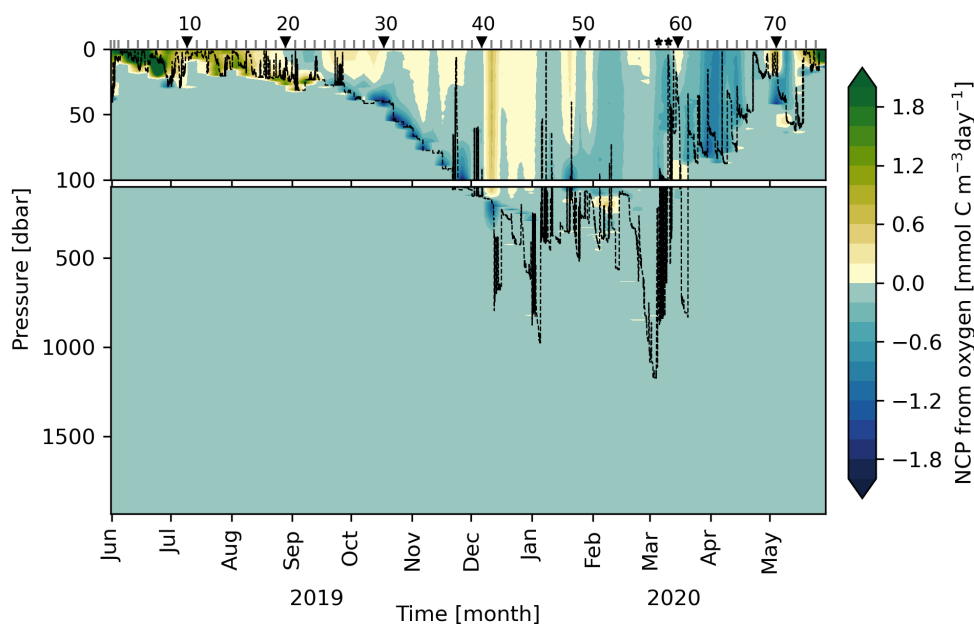
Figure 5.4: Hovmöller diagram showing daily NCP derived from oxygen at each depth for June 2019-June 2020. Blue, negative values indicate remineralization. Yellow to green, positive values indicate biological production. Note the different y-axis scales between the surface box and the deep box. Numbered triangles show every 10th Argo profile. Two stars prior to the 60th Argo station show the profiles for which Polar Water advection is prescribed. Dashed, black lines show modelled mixed layer depth.

There is a seasonal signal showing relatively strong biological production in the surface layer from June to August 2019. As autumn arrives, NCP is reduced. Negative NCP occurs as early as September in the mixed layer, after which there is a new period of moderate production of up to 0.75 mmol C m^{-3} day^{-1}. An unlikely peak in productivity appears throughout the mixed layer in December, at profile 41. Here, productivity exceeds 1.0 mmol C m^{-3} day^{-1}, which is not reasonable at this time of year due to the lack of sunlight. As winter progresses, the biological signal tends toward remineralization interspersed with instances of production. Below the mixed layer, NCP is nearly constant at approximately -0.006 mmol C m^{-3} day^{-1}. With a measurement uncertainty in oxygen of 30 µmol kg^{-1} and further uncertainties in the calculations of the model, this is well within the range of uncertainty in NCP.

Throughout the time period, there are stronger NCP signals at the base of the mixed layer, in both positive and negative direction. While it is possible that these reflect real biological processes, they could also be artifacts of internal waves or eddies. This is explored further in Section 5.2.4. The prescribed advection should not affect NCP from oxygen significantly as oxygen is not diluted in this step.

Although one might expect some signal of remineralization between the mixed layer base and the upper 1000 dbar, it is possible that this is erased through mixing in the model, or is too small to be resolved given the aforementioned uncertainties.

As there are several events of unlikely NCP values in Figure 5.4, it is useful to investigate the surface layer further. Figure 5.5 shows daily NCP in the upper 20 dbar along with integrated NCP over the same pressure range, and oxygen concentrations in the deep (1700, 1800, and 1900 dbar). If there is variability at depth that matches some of the instances of questionable NCP values, then the underlying reason could be sensor instability.
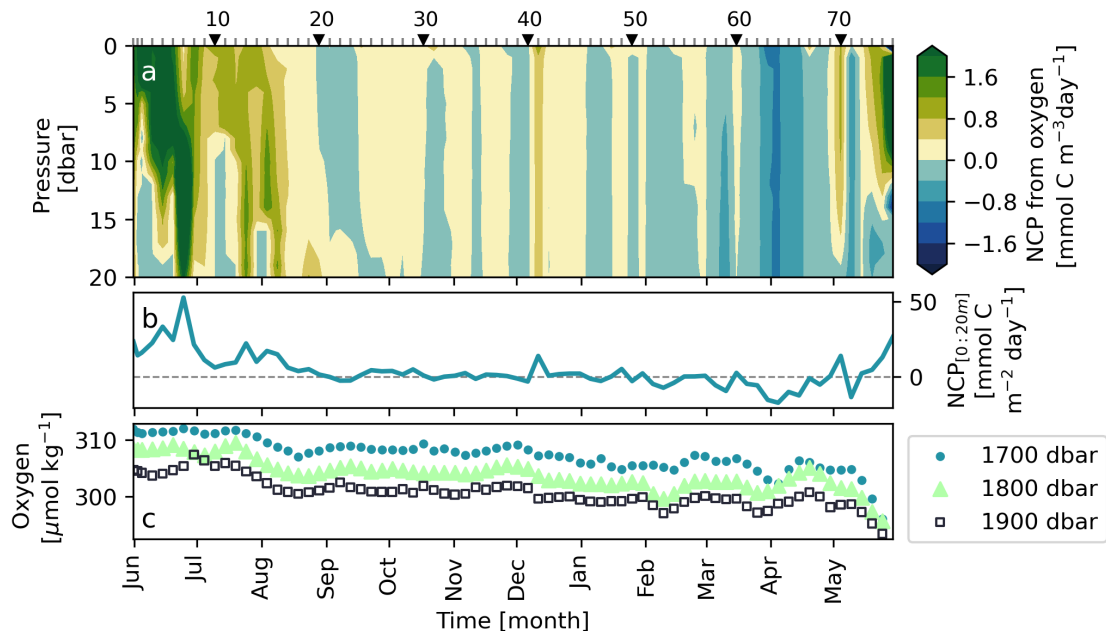

Figure 5.5: a) Hovmöller diagram of daily oxygen-derived NCP in the upper 20 dbar. Blue, negative values indicate remineralization whilst yellow to green positive values indicate biological production. Numbered triangles show every 10th Argo profile. Smaller, vertical lines indicate the Argo profiles between. b) Oxygen-derived NCP integrated over the upper 20 dbar. The dashed gray zero-line marks the divide between remineralization and biological production. c) Oxygen concentrations as measured by the Argo floats at pressure levels of 1700, 1800, and 1900 dbar (blue circles, green triangles, and open black squares respectively). Note the different y-axis scales of the surface box and the deep box.

The surface layer shows the same development as described above, with relatively strong biological production in June-August 2019, followed by alternating events of production and remineralization. The spring bloom in 2020 appears to have commenced in May. The resulting integrated NCP (Figure 5.5b) reveals a seasonal cycle close to what one would expect. There is stronger spring and summer production, and a period of near zero biological activity during September to March. There is a small peak in productivity in December, a consequence of the column of higher NCP at profile 41 also visible in Figure 5.4 and Figure 5.5a. While there is some variability in the measured oxygen concentrations at depth, these do not appear to coincide with specific events of inconsistency. There is a negative trend in all of the displayed pressure levels. This trend could lead to an overall low bias in our NCP estimate as Argo oxygen data would be erroneously low in oxygen. As oxygen is consumed during remineralization and produced during photosynthesis, the low values would lead to either lower production or stronger remineralization in our results. Sensor drift is discussed separately in Section 5.2.2.

5.2.1.2 Nitrate derived NCP

NCP is calculated from nitrate as for DIC and oxygen, except for the application of a different Redfield ratio, and the absence of air-sea gas exchange (Chapter 3). Here, R=6.95 is utilized (*Frigstad et al.*, 2014). The resulting NCP at each pressure level is displayed in Figure 5.6.
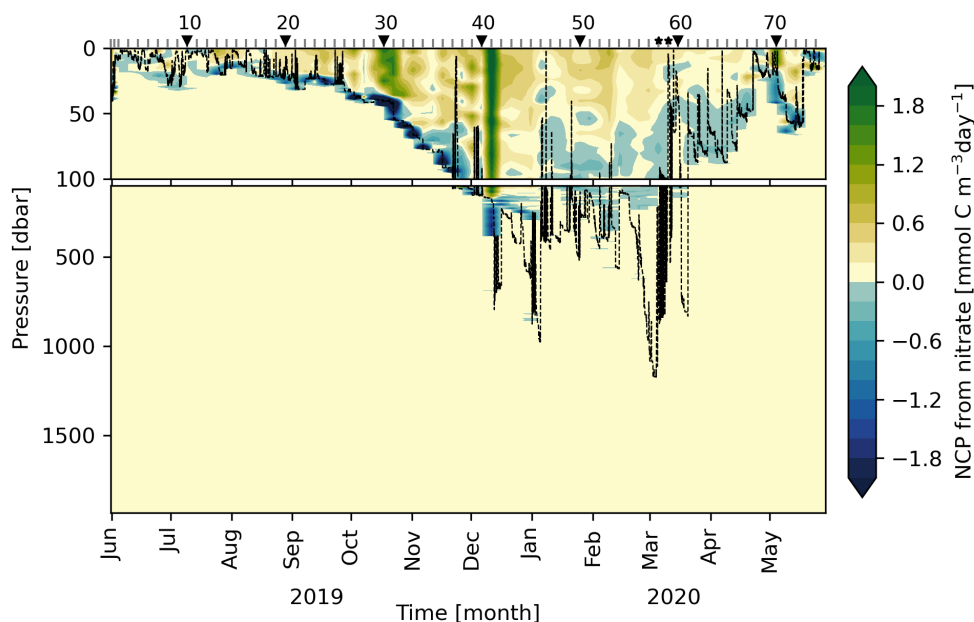

Figure 5.6: Hovmöller diagram showing daily NCP derived from nitrate at each depth for June 2019-June 2020. Blue, negative values indicate remineralization. Yellow to green, positive values indicate biological production. Note the different y-axis scales of the surface box and the deep box. Numbered triangles show every 10th Argo profile. Two stars prior to the 60th Argo station show the profiles for which Polar Water advection is prescribed. Dashed, black lines show modelled mixed layer depth.

Contrary to NCP calculated from oxygen, there appears to be very little remineralization in the nitrate derived estimates; the biological production in the surface is (almost) always positive. Two instances of particularly strong positive NCP stand out: near profiles 30 and 40. These also stood out in NCP calculated from oxygen (Figure 5.4), however there the possible bloom at profile 30 appeared as remineralization. At profile 40, NCP is positive in both cases, but the estimate based on nitrate is much stronger. It is possible for a bloom to occur in October as mixed layer deepening causes nutrients to resurface. At this time there is still some solar radiation which may trigger photosynthesis if conditions otherwise allow. As mentioned in the previous section, however, the production signal at profile 40 cannot reflect reality because it is too deep and too strong. Since it appears in all three estimates of NCP, it is possible that it is an artifact caused by internal variability that the PWP model is unable to capture. Below the mixed layer, NCP is near constant with values of approximately 0.025 mmol C m^{-3} day^{-1}. As for oxygen, thisthis part of the water column should show zero NCP, or at best show some signs of remineralization. However, these low values are within the range of uncertainty, when considering model errors in addition to measurement uncertainties in nitrate of 5 µmol kg^{-1}. Also prominent in Figure 5.6 is the negative NCP at the base of the mixed layer throughout the period. As mentioned in the previous subsection, this could

be an artifact caused by internal waves or eddies, which is further explored in Section 5.2.4. Although it could be signs of remineralization, this is less likely as the signal would then be expected to follow the seasonal production pattern more closely.

To address some of the discrepancies above, daily NCP in the top 20 dbar is shown together with NCP integrated over the same pressure range, and deep nitrate concentrations in Figure 5.7. From the two upper panels (a,b) it is clear that the seasonal pattern in NCP is incorrect. June-September 2019 shows nearly no biological production. Instead, NCP is the highest through September-February. The larger peaks derive from possible discrepancies already seen in oxygen and DIC at profiles 30 and 41. There are no clear events in nitrate concentrations that suggest these are caused by sensor instabilities. The consistently high estimated winter production could be caused by excessively strong vertical transport of nitrate into the mixed layer. In this case, vertical transport is likely also too strong for DIC and oxygen.
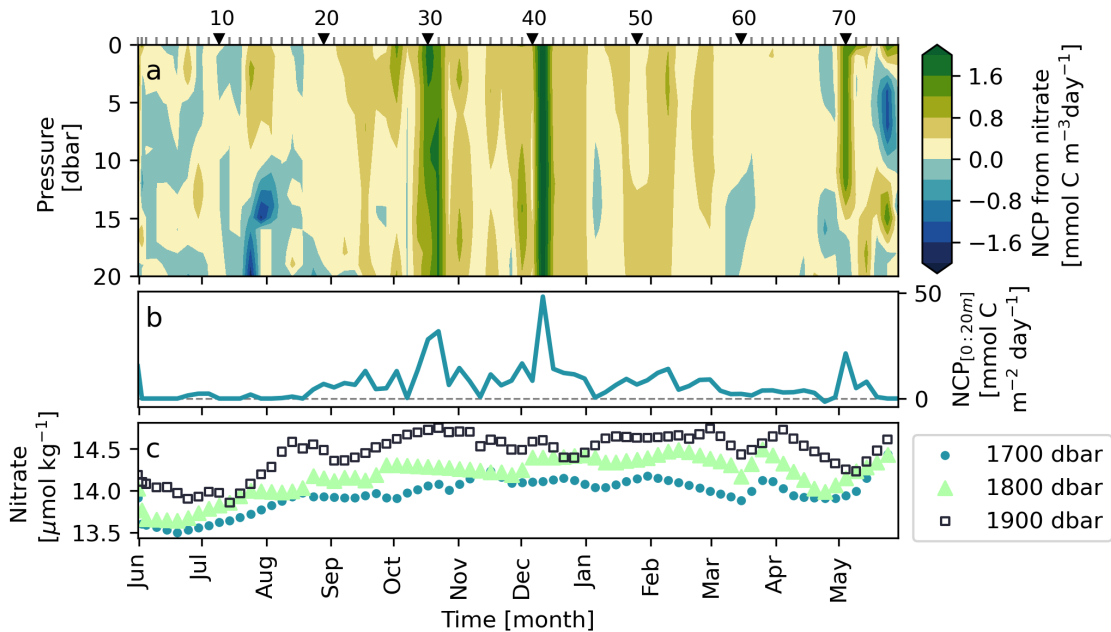

Figure 5.7: a) Hovmöller diagram of daily nitrogen-derived NCP in the upper 20 dbar. Blue, negative values indicate remineralization whilst yellow to green positive values indicate biological production. Numbered triangles show every 10th Argo profile. Smaller, vertical lines indicate the Argo profiles between. b) Nitrate-derived NCP integrated over the upper 20 dbar. The dashed gray zero-line marks the divide between remineralization and biological production. c) Nitrate concentrations as measured by the Argo floats at pressure levels of 1700, 1800, and 1900 dbar (blue circles, green triangles, and open black squares respectively).

5.2.1.3 Comparison

The previous sections have shown that neither the NCP estimates from DIC, oxygen, nor nitrate are perfect. A comparison of the three is instructive. Figure 5.8a-c show integrated NCP over the upper 20 m of the water column derived from DIC (NCP_{DIC}), nitrate (NCP_{NO3}), and oxygen (NCP_{OX}) respectively. In Figure 5.8d, the mean annual NCP (ANCP) with depth is shown for all three variables. The NCP evolution through the year is similar for DIC and

oxygen. Both show peak productivity around July with decreasing biological activity towards November. While oxygen derived NCP shows negative values all through winter, NCP_{DIC} remains positive for large periods of time, only crossing zero for a brief period in late December and in March. As discussed in the Section 5.2.1.2, the development of NCP_{NO3} is not as expected. Since nitrate is treated as a passive tracer in the model, its concentration only changes due to vertical transport. In summer, initialisation profiles are depleted of nitrate and mixed layer changes are minimal. As autumn approaches however, nutrient rich water from below is mixed up to the surface. It is possible that the model includes more transport of nitrate to the surface than what occurs naturally, leading to a falsely positive NCP in winter, and that NCP_{NO3} estimates are more sensitive to this than NCP_{DIC} and NCP_{OX} because relative nitrate gradients in the water column are larger. Alternatively, the very low summertime production and higher levels in winter could indicate a dominance of heterotrophs and a wintertime bloom of phytoplankton. This does not seem as likely.
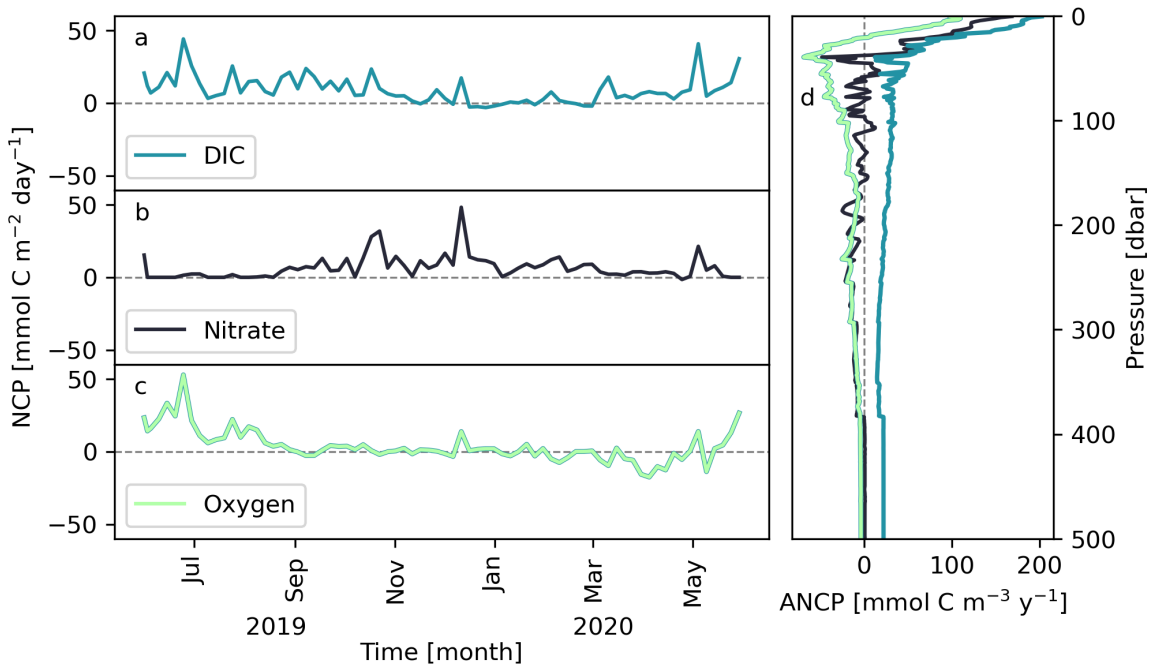

Figure 5.8: Net community production (NCP) integrated over the upper 20 dbar derived from DIC (a; blue line), nitrate (b; black line), and oxygen (c; green line). Panel d shows annual NCP (ANCP) profiles for the same components with the same color scheme applied.

As evident from Figure 5.8d, ANCP estimates also vary considerably. ANCP from DIC ($ANCP_{DIC}$) is too high, indicating grossly underestimated remineralization. There appears to be a constant offset at depth of approximately 23 mmol C m^{-3} day^{-1}. Considering the positive NCP_{DIC} seen at depth in Figure 4.14 this is not surprising, however it does not reflect reality. At steady state, ANCP integrated through the whole water column depth should result in zero such that biological production and remineralization are balanced. When $ANCP_{DIC}$ never crosses 0, this is clearly not fulfilled. The cause must lie in sensor instabilities or within the model calculations. A small imbalance could be explained by the lag in CO_2 equilibration of the carbonate system, however the offset seen is far too large for this to be the case. The depth distribution of ANCP from nitrate ($ANCP_{NO3}$) appears more reasonable, but features incidents of biological production well below 100 dbar, which is far beyond realistic

production depth. Oxygen derived ANCP ($ANCP_{OX}$) follows a similar curve to $ANCP_{NO3}$, but with a lower maximum surface production, shallower intercept (approximately 20 dbar) and more intense remineralization. While possibly showing too much remineralization at depth, $ANCP_{OX}$ appears the most reasonable of the three estimates. Note that there is a small negative offset as was seen in Figure 5.4.

In light of the above discrepancies, two questions remain to be solved: 1) If there is too much vertical transport of nitrate, why is this not also the case for DIC and oxygen? 2) How does possible sensor drift affect the NCP and ANCP estimates? The first question may be tied to air-sea gas exchange. While nitrate in the PWP model is completely governed by vertical mixing, both DIC and oxygen are also subject to equilibration processes with the atmosphere. An excessively strong vertical transport would for these properties be balanced by lower gas transfer rates, or even by outgassing. It is also possible that nitrate is more sensitive to small changes due to its constantly low concentrations compared to oxygen and DIC. Concentration gradients for nitrate are relatively high so the relative effect of vertical transport is greater for nitrate than for DIC and oxygen. The second question chiefly concerns DIC and oxygen, as no clear trend is seen in nitrate concentrations as measured by the SUNA sensor on the Argo. Though small, an evident negative trend in oxygen was seen in Figure 5.5c. This is likely due to sensor drift, though consumption caused by remineralization is also a possibility. This trend would lead to underestimated NCP_{OX} and $ANCP_{OX}$ (including stronger negative values) because the decreasing values caused by the sensor compensates for some of the oxygen production through photosynthesis. On the other hand, oxygen is utilized to correct pH measurements. Hence, oxygen drift propagates to pH. pH is then used together with Alk to calculate DIC, meaning DIC is also influenced. For DIC, the drift is positive, also leading to and underestimate of biological production. Sensor drift and how this propagates is explored further in Section 5.2.2.

5.2.1.4   Choice of integration depth

The choice of integration depth (euphotic zone) in NCP calculations is not arbitrary. In this work, an integration depth of 20 dbar was used in order to circumvent the influence of possible spurious remineralization signals at the base of the mixed layer. However, other depths would also have been reasonable. One could, for instance, use the depth at which $ANCP_{DIC}$, $ANCP_{NO3}$, or $ANCP_{OX}$ first remain negative across a significant depth interval. $ANCP_{DIC}$ does not cross zero and as such, this criterion cannot be used. For $ANCP_{OX}$, the depth would be at 21 dbar, which is very close to the already applied integration depth. $ANCP_{NO3}$ first crosses zero at 38 dbar. While it does not firmly remain in the negative range until deeper into the water column, it is a reasonable estimate of euphotic depth. This value is close to what one may find in literature. 35 dbar was obtained by taking the average of inferred values from Figure A1 in *Cherkasheva et al.* (2013). This estimate of euphotic depth incorporates calculations from both chl-α and photosynthetically available radiation (PAR) depth in the Greenland Sea. Finally, one may estimate euphotic depth as the point in which 1% of shortwave radiation is absorbed in the water column. In the PWP model, which assumes type IA waters, this equates to 73 dbar (*Plant et al.*, 2016). To evaluate the sensitivity of NCP and ANCP estimates to the choice of integration depth, I apply euphotic depths of 20, 35, and 73 dbar. Figure 5.9 shows the resulting NCP seasonal cycles, and total ANCP values are displayed in Table 5.2.

Table 5.2: ANCP derived from DIC, nitrate (NO_3), and oxygen (OX) using integration depths of 20, 35 and 73 dbar. Unbracketed values are reported in mol C $m^{-2}y^{-1}$, round brackets indicate values in g C $m^{-2}y^{-1}$.

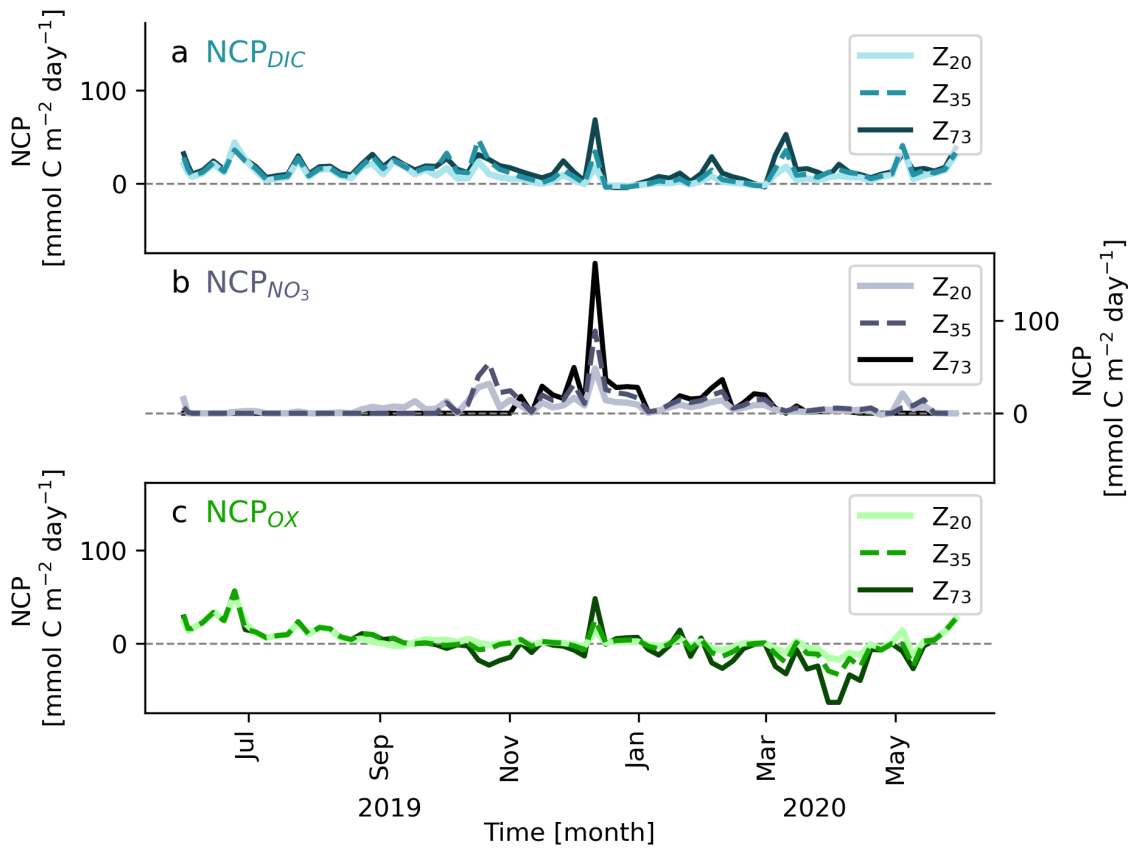|	$ANCP_{DIC}$	$ANCP_{NO_3}$	$ANCP_{OX}$
	[mol C $m^{-2}y^{-1}$] (g C $m^{-2}y^{-1}$)	[mol C $m^{-2}y^{-1}$] (g C $m^{-2}y^{-1}$)	[mol C $m^{-2}y^{-1}$] (g C $m^{-2}y^{-1}$)
$Z_{int} = 20$ dbar	3.2 (38.8)	2.4 (29.0)	1.3 (15.6)
$Z_{int} = 35$ dbar	4.3 (51.5)	3.2 (38.7)	0.8 (10.3)
$Z_{int} = 73$ dbar	5.7 (67.9)	3.2 (38.2)	-0.9 (-10.3)

Figure 5.9: NCP calculated from DIC (a), nitrate (b), and oxygen (c) using integration depths of 20 dbar (Z_{20}; lightest colors), 35 dbar (Z_{20}; dashed lines), and 73 dbar (Z_{20}; darkest colors).

The seasonal pattern of daily NCP is not altered significantly by changing integration depth. This is in accordance with work in other areas (*Plant et al.*, 2016). The magnitude of NCP_{DIC} and NCP_{NO_3}, which already suffered a positive bias, is merely increased. This is expected as positive offsets below integration depth were seen in both. The opposite occurs for NCP_{OX}, which is more negative with increasing integration depth. Total ANCP values largely mirror these findings. The exception is $ANCP_{NO_3}$. Due to its oscillating vertical ANCP profile in the range 35-200 dbar (Figure 5.8d), $ANCP_{NO_3}$ is nearly equal using integration depths of 35 and 73 dbar. Considering the anomolous NCP and ANCP patterns produced in this work, it is hard to determine how sensitive this method is to integration depth.

5.2.2   Sensor drift

Signs of sensor drift have been observed in Figure 4.3, Figure 5.5, and Figure 5.7. It is necessary to determine if this is the case and if so, to what degree. As mentioned in Chapter 3, the Argo data used is quality flagged 1, meaning it is already corrected for drift and offsets. However, is appears that the corrections have not removed all drift. One method to detect drift is to examine the development of measurements at depth, as was done in the aforementioned figures. It is useful to further consider linear regression slopes at these depths. In light of this, values at 1700, 1800, and 1900 dbar are plotted for DIC, nitrate, oxygen, and pH in Figure 5.10, with respective regression lines.
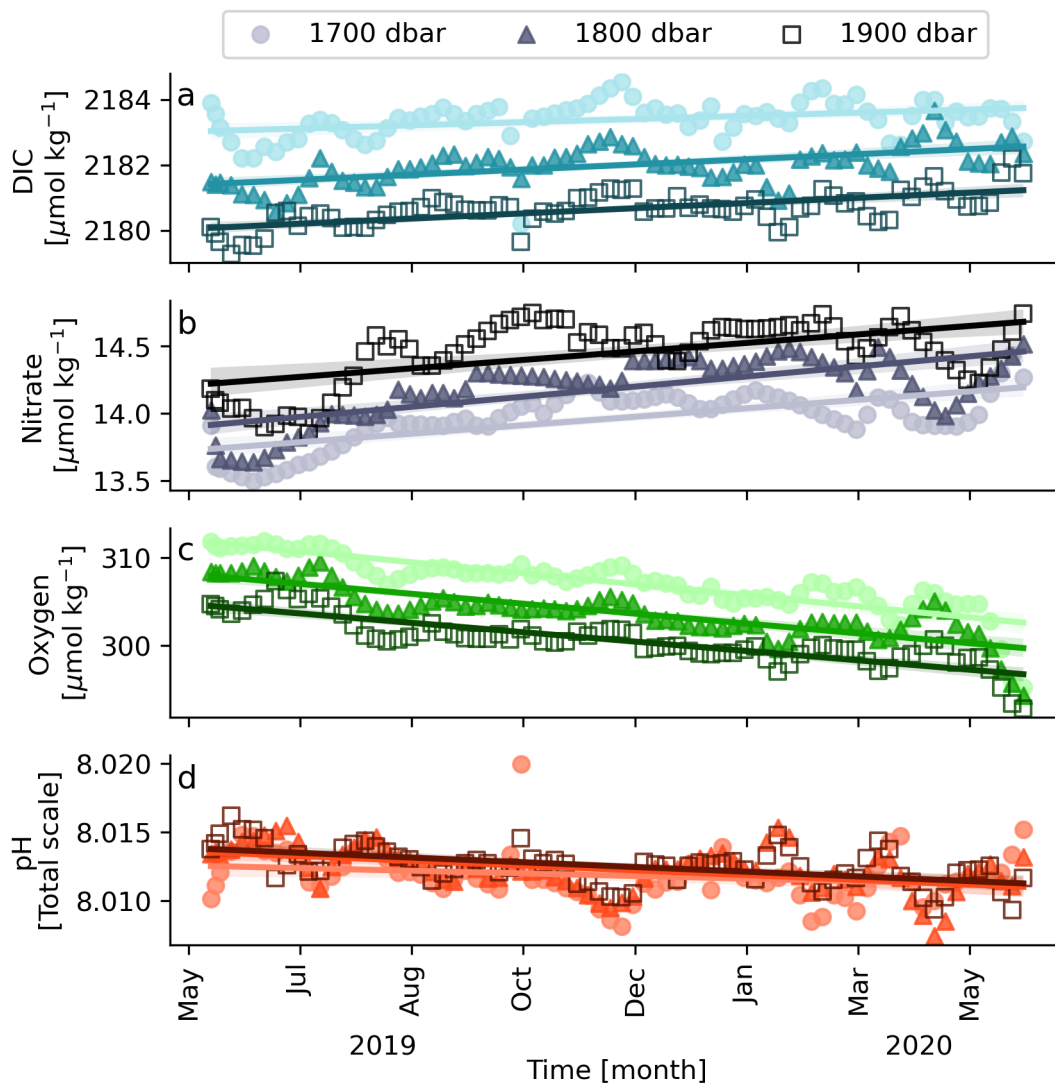
Figure 5.10: DIC (a), nitrate (b), oxygen (c), and pH (d) at pressures of 1700, 1800, and 1900 dbar. The pressure levels are indicated by light-colored circles, dark triangles, and open squares respectively. Regression lines for each pressure level are shown as solid lines in the same color scheme.

The regression lines show that there is a small trend in each property. The trend is nearly equal at each pressure level for all properties. The percentage change is largest in oxygen, with a reduction in 2.6% year^{-1}. Next is nitrate with an increase of 1.8% year^{-1}. The

changes in DIC and pH are comparatively small: $+0.05\%$ and -0.03% respectively. The calculated percentage trends support what was inferred visually from Figure 4.3. The trend in oxygen is likely the ultimate root of the erroneous drift in pH and DIC. As mentioned in Chapter 3, when pH is calibrated, it uses corrected temperature, salinity and oxygen from the float as input in CANYON-B (*Bittig et al.*, 2018) to calculate the reference data used to correct the float pH. CANYON-B is very sensitive to the oxygen input data, and thus any inconsistencies in these. When this oxygen data set with a 2.6% was used to calculate the pH reference data, it ultimately left a small trend in the calibrated pH. As pH then is used to calcualte DIC, the trend propagates. The trend in nitrate, however, is unrelated since WOA2018 was used as reference data and not CANYON-B.

The small drift seen in DIC, nitrate, oxygen, and pH is well within the range of uncertainty of each property. However, it is possible that even small drifts accumulate such that other calculations are affected. If the drift seen in Figure 5.10 strongly affects the NCP estimates, plotting the change in a property at depth between two consecutive Argo profiles against the biological production calculated for the same time interval could reveal this. Figure 5.11 shows this for NCP at 10 dbar, and profile differences at 1700, 1800, and 1900 dbar.
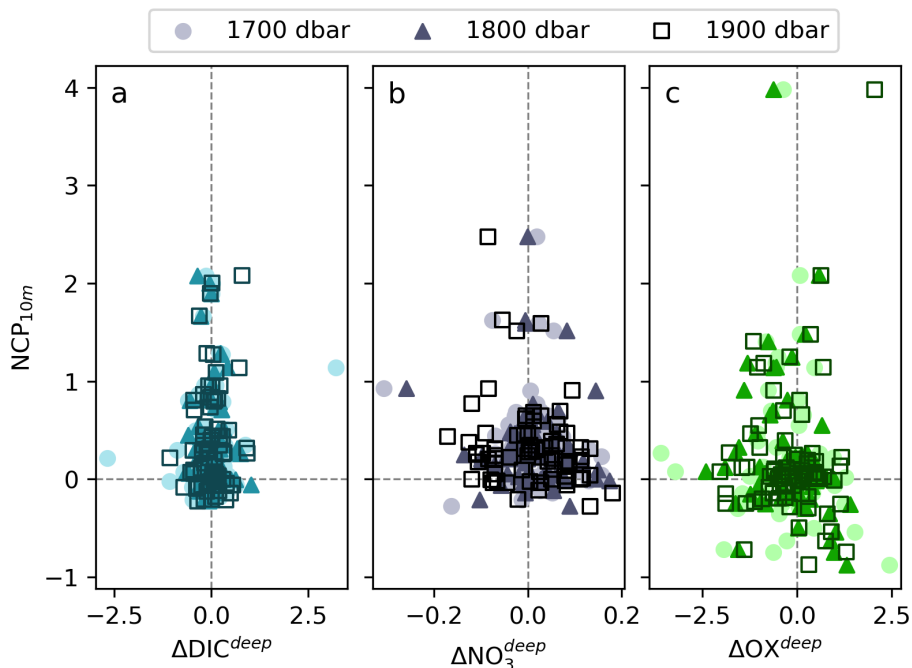

Figure 5.11: Change in DIC (a), nitrate (b), and oxygen (c) concentrations between an Argo profile and the previous (ΔDIC^{deep}, ΔNO_3^{deep}, ΔOX^{deep}) plotted against NCP at 10 m as calculated from respective properties. Light-shaded circles indicate delta values from 1700 dbar, dark triangles 1800 dbar, and open squares 1900 dbar.

Profile-to-profile change at the three displayed pressure levels do not appear to correlate strongly with NCP at 10 m for any of the plotted properties. In fact, linear regression for panels a-c result in Pearson correlation coefficients (r) with absolute values below 0.25 in all cases. Moreover, the sign of r for DIC and oxygen is not the same at all pressure levels. This implies that sensor drift is inconsequential for NCP calculations.

This implies the correlation strengths are inconsequential as a measure of the sensor drift's

impact on NCP. If there was indeed a strong significant correlation, then it should be of roughly the same magnitude and sign at all three pressure levels. While r is negative for all three pressure levels for nitrate, the values are still too small to carry weight. However, we cannot with certainty eliminate sensor drift as an influence on NCP calculations from this test alone. Non-linearities in the model makes it challenging to identify the exact impact of sensor drift, if any.

The way in which sensor drift corrections are carried out limits the amount of meaningful interpretation one can do when corrected data still exhibits trends. Time allowing, it would have been useful to further examine the corrections applied. The corrections may not capture everything. The underlying assumption when using oxygen to correct pH is that the relation between the two is constant in the deep water masses. However, the Greenland Sea is a region with periods of deep convection. Mixing ventilating the deep could alter the ratio. It is possible that conditions have changed compared to the climatology used as reference data for corrections. In that case, maybe there *should* be a gradient, or a trend is overcorrected. Though the observed trends are small, it would be interesting to understand more of where they derive from. Due to time limitations, however, I leave this task for others to explore.

5.2.3 Faulty mixing scheme?

As mentioned in Section 4.2, I have changed the mixing scheme in the model to account for the fact that concentrations are not additive. In the version of *Brakstad et al.* (2019), the mixing algorithm invoked during the first two mixing processes uses the mean values of a property within the new mixed layer as the new value. For temperature and density, this is okay, because they are not dependent on solvent mass. The same approach is used by *Glover et al.* (2011) for hydrographic and biogeochemical parameters. However, salinity and biogeochemical properties are in units of concentration. While mass is conserved upon mixing, concentration is not. It is therefore necessary to convert concentrations to mass to calculate the mass exchange before converting the units back to concentrations to correctly model these fluxes. Preliminary results showed that changing the mixing scheme from the means-based mixing to mass-based made the model somewhat more sensitive. Here, I further investigate the differences in results between the two mixing schemes to determine if the new mixing scheme is indeed an improvement or if it is the cause of some of the discrepancies found.

Table 5.3: Net vertical transport (F_Z) and net air-sea gas exchange (F_{GE}) through the water column, and ANCP over the upper 20 dbar calculated from DIC, nitrate, and oxygen ($ANCP_{DIC}^{20}$, $ANCP_{NO_3}^{20}$, and $ANCP_{OX}^{20}$ respectively) for mix_{new} and mix_{old}. mix_{new} is the bulk mixing scheme implemented in this work, mix_{old} is the mixing scheme used previously.

	F_Z [mol C m^{-2} y^{-1}]	F_{GE} [mol C m^{-2} y^{-1}]	$ANCP_{DIC}^{20}$ [mol C m^{-2} y^{-1}]	$ANCP_{NO_3}^{20}$ [mol C m^{-2} y^{-1}]	$ANCP_{OX}^{20}$ [mol C m^{-2} y^{-1}]
mix_{new}	1.26	2.25	3.23	2.4	1.3
mix_{old}	1.21	2.31	2.76	2.26	1.11

Key results from the calculations using the mean-based (mix_{old}) and the mass-based (mix_{new}) bulk mixing methods are displayed in Table 5.3. It is clear that the differences are minor, and within the range of uncertainty for each estimate. F_Z in mix_{old} is lower than

in mix_{new}. Since less carbon is transported to the surface, air-sea gas exchange of carbon is stronger, as reflected in the higher value of F_{GE} for mix_{old}. Note that F_Z and F_{GE} are computed totals over the entire water column, while ANCP estimates are for the upper 20 dbar only. This is to ease comparison with results of others' work. Lower values of ANCP in mix_{old} compared to mix_{new} indicates more remineralization and/or less production.

Having seen that there is a difference in vertical transport between the two bulk mixing schemes, it is interesting to examine vertical transport further. Figure 5.12 shows the total vertical transport into the mixed layer, and into the surface by each mixing process, as well as the mixing depths of each process. Figure 5.12h shows that mixing is shallower for mix_{old}, than was seen in Figure 4.12h for mix_{new}. While the model calculates a mixed layer depth maximum of around 800 dbar in March, actual mixing depth is much shallower. This was also seen for mix_{new}. There is vertical transport out of the surface (upper 20 dbar) for both StIn and BRi mixing processes. This means that reverting to the old mixing scheme does not solve the problem of negative fluxes.
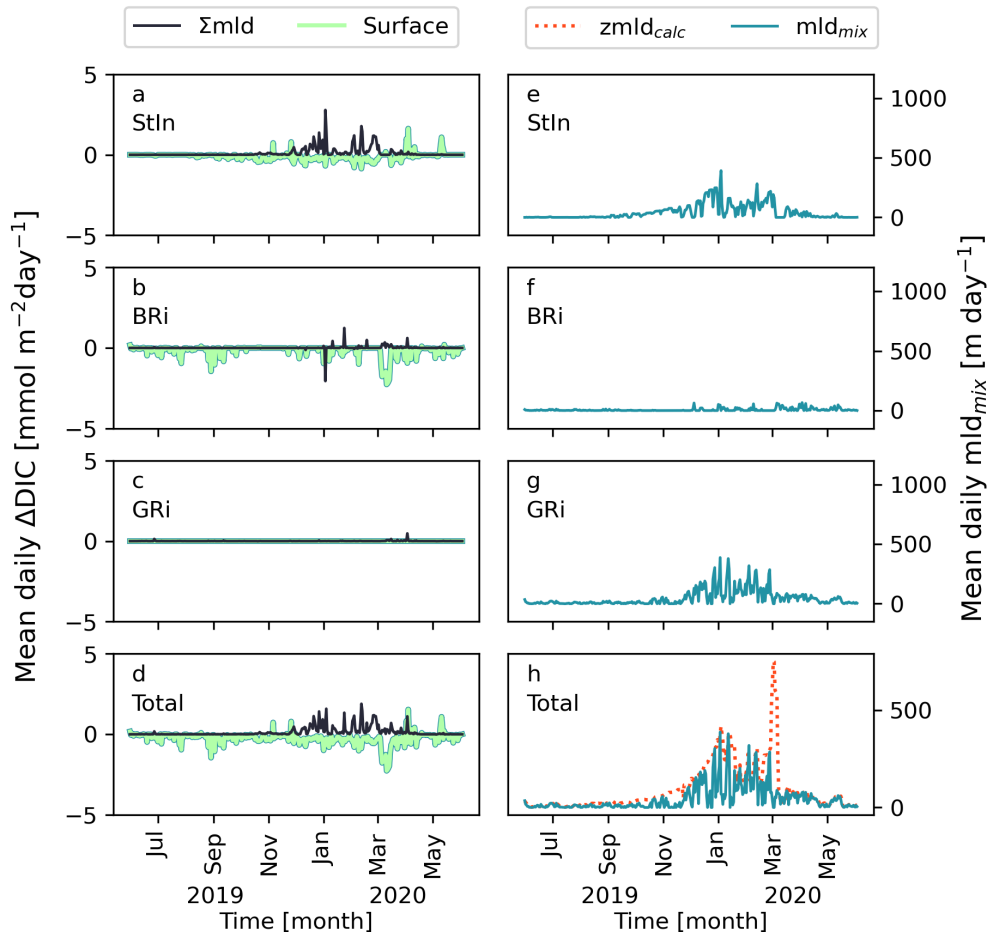
Figure 5.12: Mean daily change in DIC as a result of vertical transport induced by static instability (StIn; a), bulk Richardson number instability (BRi; b), gradient Richardson number instability (GRi; c) and the sum of the three (Total; d) are displayed on the left hand side. The values are calculated for the surface box (light green line) and summed over the mixed layer (black line). The right hand side (e-h) shows the mean daily change in mixing depth caused by the same mechanisms. Panel h also shows the mixed layer depth calculated by the Nilsen method ($zmld_{calc}$; dashed red line).

To determine the cause of the reduced ANCP in mix_{old} compared to mix_{new}, NCP_{DIC}, NCP_{NO_3}, and NCP_{OX} summed over the upper 20 dbar are plotted with time in Figure 5.13a-c for each method. Figure 5.13d shows the respective vertical distributions of ANCP. The spurious December peak seen in mix_{new} is not present for mix_{old} in any of the NCP estimates. This peak was attributed to an episode of relatively strong transport out of the mixed layer. Figure 5.12d shows that this mixing event does not occur for mix_{old}, strengthening the hypothesis that the peak is caused by excessive mixing. Lower $ANCP_{DIC}$ for mix_{old} appears to be caused by both a removal of the spurious peak and by a little more remineralization than for mix_{new}. For the other two estimates, the largest difference is the removal of the spurious peak. The ANCP profiles do not show significant differences.
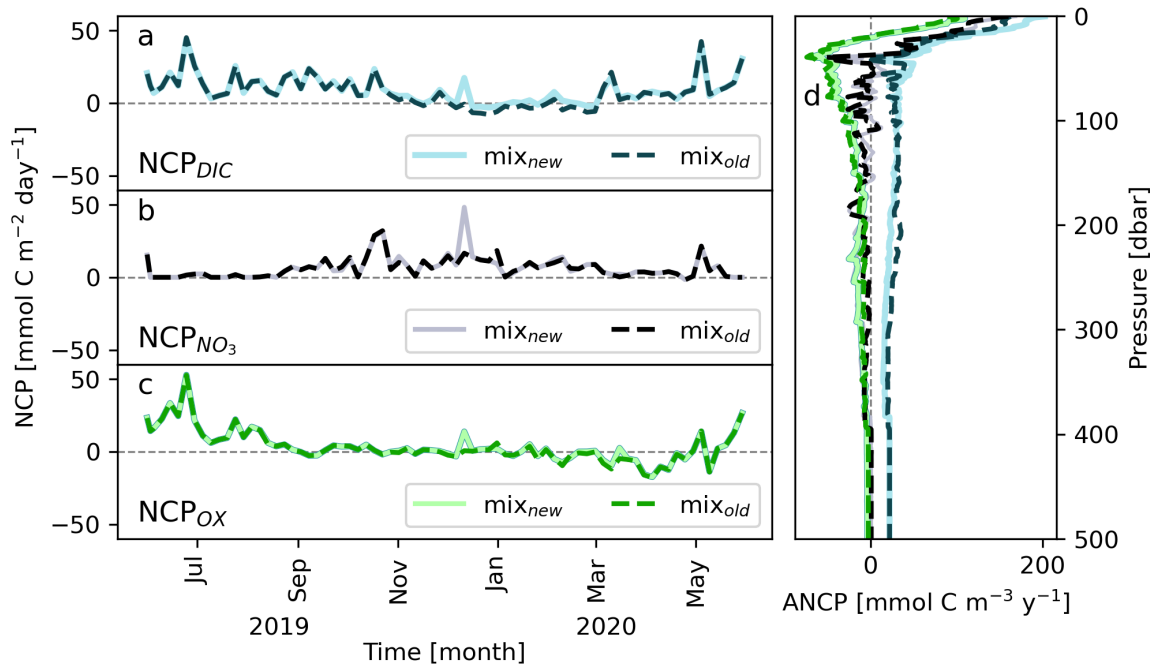

Figure 5.13: Net community production (NCP) integrated over the upper 20 dbar derived from DIC (a; blue lines), nitrate (b; black lines), and oxygen (c; green lines). Panel d shows annual NCP (ANCP) profiles for the same components with the same color scheme applied. Solid, light lines show calculations using a mass-based mixing scheme (mix_{new}). Dashed, dark lines show calculations using a means-based mixing scheme (mix_{old}).

The differences in air-sea gas exchange are best viewed by plotting $F_{GE}(mix_{new})$-$F_{GE}(mix_{old})$. This is done in Figure 5.14 along with mixed layer depth calculated for mix_{new}. The figure shows that F_{GE} is nearly equal for the two cases from June until November. As the mixed layer starts to deepen, the aforementioned event of strong mixing in December for mix_{new} transports DIC towards the surface, reducing air-sea gas transfer compared to mix_{old} where the onset of deeper mixing is delayed.
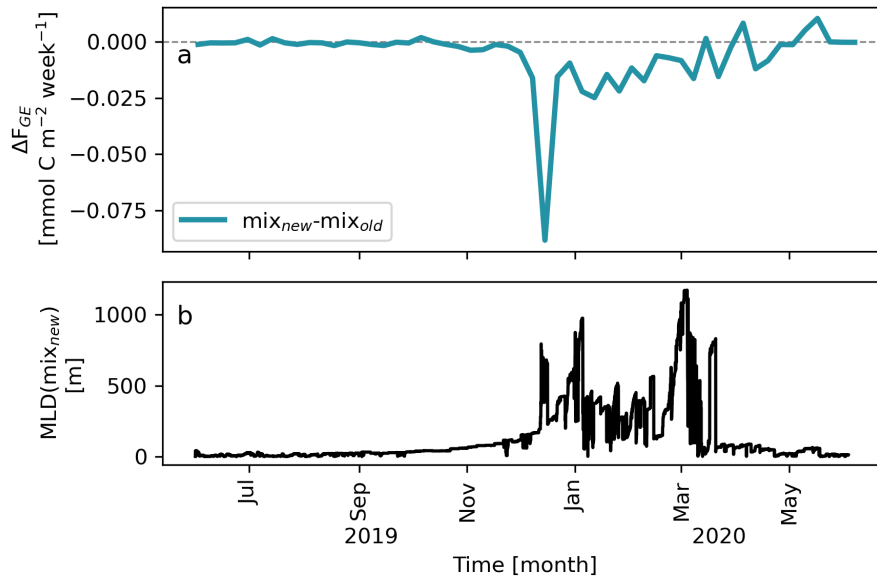
Figure 5.14: a) Mean weekly $F_{GE}(mix_{new})$-$F_{GE}(mix_{old})$. b) Mixed layer depth as calculated by the Nilsen method for mix_{new}.

5.2.4 Internal waves?

In Figure 4.2a there were signs of possible internal waves. Later, in Figure 4.14, possibly spurious signals of remineralization were observed at the base of the mixed layer. Internal waves are caused by perturbations at the surface or from tides meeting topography. The perturbation in one layer of the water column propagates to the next density surface, leading to oscillations through the whole stratified water column. As the Argo float travels through these oscillations, values within a density surface are displaced vertically relative to the previous profile. Internal waves would therefore appear as structurally similar undulations in all the conservative tracers measured, and at all density surfaces. If the float encounters an eddy, the effect is the same. The presence of internal waves in the Argo data could lead to the mentioned spurious signals of remineralization as the PWP model is not equipped to account for processes causing internal waves. To determine if there is indeed a presence of internal waves in the dataset, temperature, σ_θ, and AOU are plotted from 1500-1900 dbar for the full annual cycle in Figure 5.15.
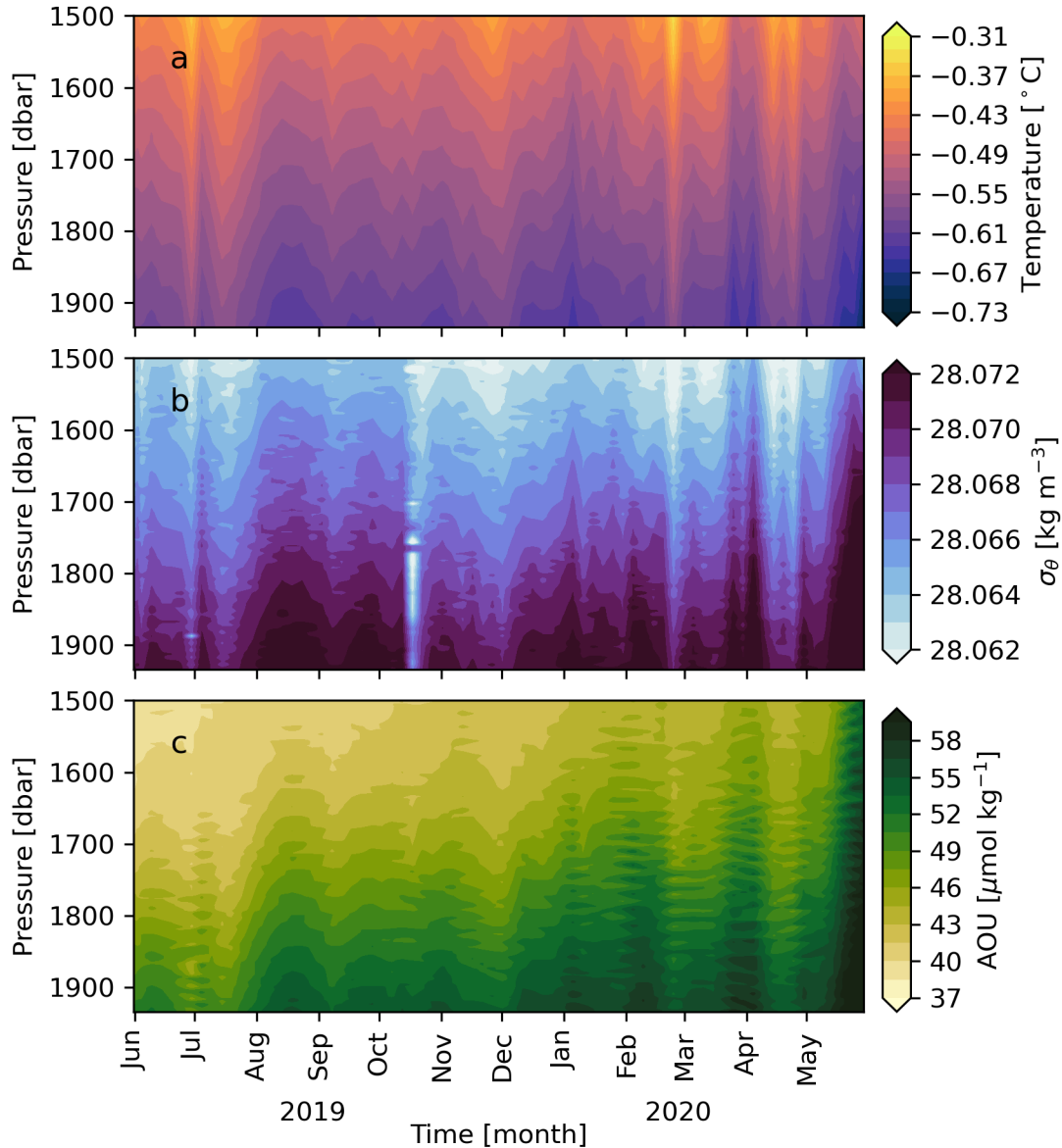
Figure 5.15: Hovmöller diagrams of temperature (a), potential density anomaly (σ_θ; b), and AOU (c) from 1500-1934 dbar. The figure covers the period June 2019-May 2020.

There is conspicuous evidence of internal waves and/or eddies in all plotted tracers. Wave crests and troughs of each tracer coincide in time. Especially clear is the negative displacement in July-August followed by lifting of the water masses in August-September. Several oscillations of lower amplitude follow in September-December. The internal wave signal in AOU is somewhat affected by the oxygen sensor drift, leading to a visible positive trend through the period.

Plant et al. (2016) found similar oscillations attributed to internal waves in several profiling floats in the Gulf of Alaska. They corrected for the vertical displacement in the Argo floats by adjusting model density profiles to match those of the Argo values. They then interpolate the new model profiles back to the model vertical grid before calculating NCP. In this work, I do not correct for internal waves due to time limitations.

Chapter 6

Conclusions

In this work, a mixed layer budget was used to decompose the drivers of DIC variability, with the ultimate goal of determining the drivers of $p\mathrm{CO}_2^{oc}$ variability. Physical fluxes from the mixed layer budget, *i.e.* vertical fluxes and air-sea gas exchange, were estimated using a one dimensional mixing model. Net community production was estimated as a residual between DIC calculated from measurements from an Argo float and model output. To this end, an existing PWP model tuned for the Greenland Sea was improved by including inorganic carbon chemistry and air-sea gas exchange. A scheme to reinitialize the model for every Argo profile was implemented in order to facilitate estimation of NCP.

Net fluxes of vertical transport and air-sea gas exchange were estimated to be 15±15% g C m^{-2} y^{-1} and 27±20% g C m^{-2} y^{-1} respectively. The residual, *i.e.* NCP and unexplained fluxes, was 39±25% g C m^{-2} y^{-1}. The evolution of net transport into the mixed layer was as expected, with fluxes near zero in summer, and a net positive transport in winter. However, surface fluxes were negative. This was surprising, and may indicate the existence of unresolved deficiencies in the approach. However, considering that the estimated air-sea gas exchange flux was robust to changes in advection, and the fact that it follows the expected seasonal pattern, the negative fluxes likely have little effect on the other fluxes. In fact, vertical transport appears to be too strong, leading to overestimated NCP. Thus, everything considered, the results agree quite well with the theoretical changes in DIC estimated by *Miller et al.* (1999). Like their results, I have found strong biological activity in the summer months that draws down carbon concentrations. Despite the anomolous surface fluxes, I too have found that there is a net flux of carbon into the mixed layer in the convective months which results in drastically reduced air-sea gas exchange. While *Miller et al.* (1999) found vertical fluxes of similar magnitude to their estimates of fluxes caused by biology, vertical transport here is only 38% of NCP. In this work, the vertical fluxes lead to periods of weak outgassing, in alignment with the supersaturation seen in the Argo float $p\mathrm{CO}_2$. The means-based mixing scheme implemented in previous versions of the model (*e.g. Brakstad et al.* (2019); *Glover et al.* (2011)) was less sensitive to atmospheric forcing, leading to somewhat smaller vertical fluxes which in turn caused a higher net air-sea gas exchange flux in part owing to less outgassing in winter. For both the mass-based mixing used in this work, and the means-based mixing tested in Section 5.2.3, convection does cause a net increase of carbon in the mixed layer in winter. While this is not reflected in the estimated $p\mathrm{CO}_2^{oc}$ by the model due to the negative surface fluxes, the constraint on $p\mathrm{CO}_2$ by reinitializations every

5th day clearly shows the interplay between vertical transport and air-sea gas exchange in winter. The results are thus ambiguous: the overall dynamics are consistent with literature, but work remains to be done to uncover model deficiencies to properly elucidate the influence of DIC dynamics on $p\mathrm{CO}_2^{oc}$ in the Greenland Sea.

It is not possible to fully evaluate the effect of DIC changes on $p\mathrm{CO}_2^{oc}$ variability with the method applied at the current time. However, the method shows potential. Thanks to the frequent reinitializations it is possible to gain an overview of the seasonal carbon dynamics by disregarding some of the evidently erroneous results. With further improvements, the method could constitute a novel technique to decompose carbon fluxes in the Greenland Sea, giving unique insight on carbon dynamics in the region. The concept works well in terms of calculating biology as a residual, as has already been demonstrated in the Southern Ocean and Gulf of Alaska (*Briggs et al.*, 2018; *Plant et al.*, 2016). Yet, the estimate of vertical transport requires refinement. Further work is needed to understand the negative surface fluxes and how to correct these, if needed, before the model can be applied to study carbon dynamics at the detailed scale attempted in this work. Additionally, the influence of internal waves and eddies is currently not accounted for. This has likely caused spurious signals of remineralization at the base of the mixed layer. Future work might include filtering out internal waves or applying σ surfaces as vertical coordinates instead of pressure.

A major assumption is made in assuming that no local advection occurs, and that horizontal homogeneity is valid. This is the basis that enables us to use a one-dimensional model to estimate fluxes representative for the whole Greenland Sea gyre. The limitation of this assumption is clear from the influence that presence of PW has on the results at the end of the captured annual cycle. The first signs of PW occur within the Greenland Sea, but the last two Argo profiles are relatively close to the gyre's Western boundary and may be affected by the East Greenland Current. The model cannot capture such influences and *ad hoc* parameterizations must be added to account for them. On the scale of individual floats, care must be taken to include the profiles most representative of the gyre. This was attempted here, but one could argue that the last 3-4 profiles should have been excluded. Here, the opportunity to include a full annual cycle weighed heavily in the decision to keep these profiles, but the results need to be taken with care. On the scale of capturing the general annual cycle of carbon dynamics in the region, more Argo floats are needed. A solid fleet capturing several years of continuous measurements in the region would lead to much more robust results. A challenge in this respect is the tendency of the Argo floats to drift out of the gyre relatively quickly. To circumvent this, it has been suggested to alter the parking depth in the Greenland Sea to depths greater than 1000 dbar since this pressure level is a major transport vein out of the region (ref. personal communication with Kjell Arne Mork).

While more Argo floats are certainly required as a cost-efficient way to obtain measurements, the importance of scientific cruises to the Greenland Sea is not diminished. Until measurement uncertainty in Argo floats reaches an acceptable level, cruises (especially winter cruises) are vital to maintain an updated set of reference values for calibration purposes. The Argo data compared reasonably well to GLODAPv2 data, but discrepancies were found in some of the carbon system properties. This is likely due to the known incoherence in measured *versus* calculated variables. For the Argo float, pH was measured while DIC and Alk were calculated. For GLODAPv2, pH is usually calculated, while DIC and Alk are measured. The incoherence between measured and calculated values is especially a challenge for pH. Moreover, the pH sensors themselves are prone to relatively large uncertainties. An additional challenge for

this work has been that Argo quality control requirements proved inadequately strict for this application. Through this work, weaknesses in quality control have been discovered and corrected. Calibration of pH data in the Nordic Seas is in general a challenge. CANYON-B works well in the Southern Ocean, but deep convection and mixing of water masses in addition to the lack of spectrophotometrically measured pH data makes it harder to use in the Nordic Seas (ref. personal communication with Siv Kari Lauvset). Other methods used to calibrate Argo pH data are the locally interpolated regression (LIR; (*Carter et al.*, 2018)) and Empirical Seawater Property Estimation Routines (ESPERs; (*Carter et al.*, 2021)) algorithms. However, pH vlues calculated using these three methods are slightly different, indicating there are underlying inconsistencies in the reference data for the Nordic Seas. Clearly, much work is needed on improving pH measurements, closing the gap between measured and calculated carbon properties, and in reconciling reference data used for calibration. As a simple, first step of future work, it would be interesting to rerun the analysis carried out in this work on the newly recorrected data from the Argo float used in this work.

In addition to the mentioned investigations needed on the mechanisms of vertical transport in the model, and potentially changing the vertical coordinates, optimizing the air-sea gas exchange coefficients for oxygen could prove a useful improvement. Currently, these are tuned for the Gulf of Alaska (*Plant et al.*, 2016). As the Greenland Sea, the Gulf of Alaska is a high-latitude region in the Northern hemisphere strongly influenced by wind. However, there could be regional differences that alter the relative contribution of diffusive gas exchange, the effect of partially dissolved bubbles, and that of completely dissolved bubbles between the two locations.

The uncertainty analysis carried out in this work is simple by nature and relies on assumptions of independence in the calculated uncertainties that are not valid. A more rigorous approach, such as a Monte Carlo analysis would be beneficial to improve the legitimacy of the results. This should be considered if the method is to be further developed in the future.

Although imperfect, the methods applied in this work constitute a valuable addition to the toolbox of techniques used to examine carbon dynamics. For the first time, biogeochemistry and air-sea gas exchange has been added to a PWP-model tuned to the Greenland Sea. With further improvements, the method could become an important technique for studies on the biogeochemical dynamics in this region. This requires continued efforts in both Argo deployment and ship-based measurements, as well as advances in pH sensor reliability and Argo quality control requirements.

Appendix A

Appendix

Figure A.1 shows how ice production in the model is extremely intermittent, and how this affects air-sea gas transfer.
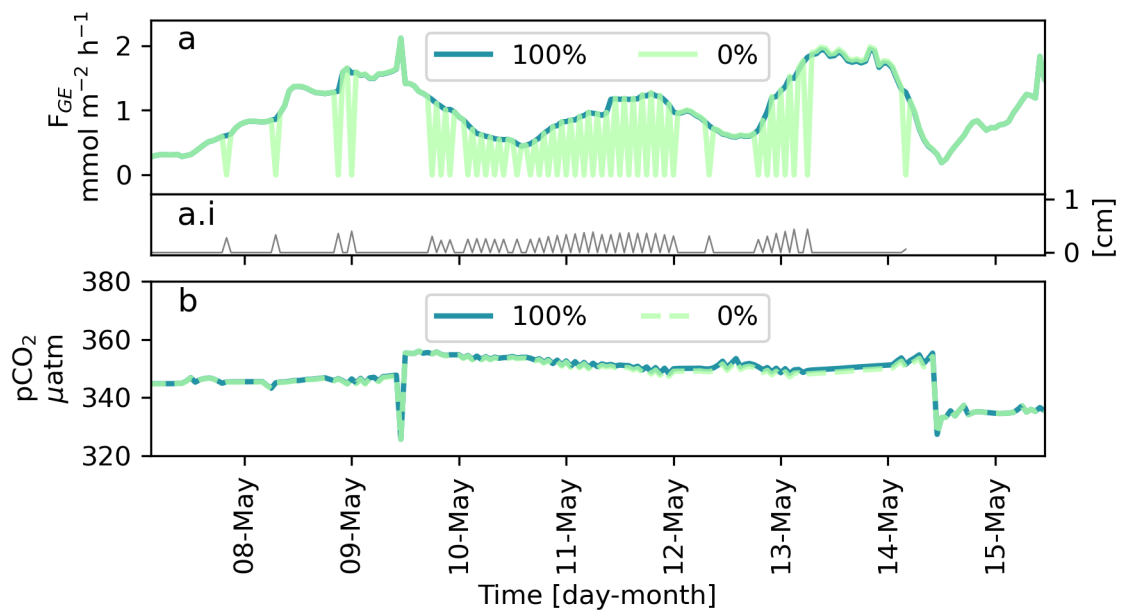

Figure A.1: a) Hourly air-sea gas exchange for model run with 100% gas flux under ice conditions (blue line), and 0% gas flux under ice conditions (light green line). a.i) Ice produced by the model. b) $p\text{CO}_2^{oc}$ for the same cases as in a.

Bibliography

Álvarez, M., N. M. Fajar, B. R. Carter, E. F. Guallart, F. F. Pérezpérez, R. J. Woosley, and A. Murata, Global Ocean Spectrophotometric pH Assessment: Consistent Inconsistencies, *Cite This: Environ. Sci. Technol*, *54*, 10,977–10,988, doi:10.1021/acs.est.9b06932, 2020.

Anderson, L. A., On the hydrogen and oxygen content of marine phytoplankton, *Deep Sea Research Part I: Oceanographic Research Papers*, *42*(9), 1675–1680, 1995.

Anderson, L. G., H. Drange, M. Chirerici, A. Fransson, T. Johannessen, I. Skjelvan, and F. Rey, Annual carbon fluxes in the upper Greenland Sea based on measurements and a box-model approach, *Tellus*, *52B*(3), 1013–1024, doi:10.1034/j.1600-0889.2000.d01-9.x, 2000.

Arrigo, K. R., S. Pabi, G. L. Van Dijken, and W. Maslowski, Air-sea flux of CO2 in the Arctic Ocean, 1988-2003, *J. Geophys. Res*, *115*, 4024, doi:10.1029/2009JG001224, 2010.

Belbéoch, M., A. Lizé, and T. Latter, OceanOPS.

Benson, B., and D. Krause, The concentration and isotopic fractionation of oxygen dissolved in freshwater and seawater in equilibrium with the atmosphere, *Limnology and Oceanography*, *29*, 620–632, 1984.

Bittig, H., et al., SCOR WG 142: Quality Control Procedures for Oxygen and Other Biogeochemical Sensors on Floats and Gliders. Recommendation for oxygen measurements from Argo floats, implementation of in-air-measurement routine to assure highest long-term accuracy, *Tech. rep.*, doi:https://doi.org/10.13155/45917, 2014.

Bittig, H. C., T. Steinhoff, H. Claustre, B. Fiedler, N. L. Williams, R. Sauzède, A. Körtzinger, and J. P. Gattuso, An alternative to static climatologies: Robust estimation of open ocean CO2 variables and nutrient concentrations from T, S, and O2 data using Bayesian neural networks, *Frontiers in Marine Science*, *5*(SEP), 328, doi:10.3389/FMARS.2018.00328/BIBTEX, 2018.

Brakstad, A., K. Våge, L. Håvik, and G. W. K. Moore, Water Mass Transformation in the Greenland Sea during the Period 1986–2016, *Journal of Physical Oceanography*, *49*(1), 121–140, doi:10.1175/JPO-D-17-0273.1, 2019.

Brakstad, A., G. Gebbie, K. Våge, E. Jeansson, and S. R. Ólafsdóttir, Formation and pathways of dense water in the Nordic Seas based on a regional inversion, *Progress in Oceanography*, *212*, 102,981, doi:10.1016/J.POCEAN.2023.102981, 2023.

Briggs, E. M., T. R. Martz, L. D. Talley, M. R. Mazloff, and K. S. Johnson, Physical and Biological Drivers of Biogeochemical Tracers Within the Seasonal Sea Ice Zone of the Southern Ocean From Profiling Floats, *Journal of Geophysical Research: Oceans*, *123*(2), 746–758, doi:10.1002/2017JC012846, 2018.

Carter, B. R., R. A. Feely, N. L. Williams, A. G. Dickson, M. B. Fong, and Y. Takeshita, Updated methods for global locally interpolated estimation of alkalinity, pH, and nitrate, *Limnology and Oceanography: Methods*, *16*(2), 119–131, doi:10.1002/LOM3.10232, 2018.

Carter, B. R., et al., New and updated global empirical seawater property estimation routines, *Limnology and Oceanography: Methods*, *19*, 785–809, doi:https://doi.org/10.1002/lom3.10461, 2021.

Carval, T., et al., Argo User's Manual, *Tech. rep.*, doi:10.13155/29825, 2019.

Cherkasheva, A., E.-M. Nöthig, E. Bauerfeind, C. Melsheimer, and A. Bracher, From the chlorophyll a in the surface layer to its vertical profile: a Greenland Sea relationship for satellite applications, *Ocean Sci*, *9*, 431–445, doi:10.5194/os-9-431-2013, 2013.

Codispoti, L. A., V. Kelly, A. Thessen, P. Matrai, S. Suttles, V. Hill, M. Steele, and B. Light, Synthesis of primary production in the Arctic Ocean: III. Nitrate and phosphate based estimates of net community production, *Progress in Oceanography*, *110*, 126–150, doi:10.1016/J.POCEAN.2012.11.006, 2013.

De Boyer Montégut, C., G. Madec, A. S. Fischer, A. Lazar, and D. Iudicone, Mixed layer depth over the global ocean: An examination of profile data and a profile-based climatology, *J. Geophys. Res*, *109*, 12,003, doi:10.1029/2004JC002378, 2004.

Dickson, A. G., Standard potential of the reaction: AgCl(s) + 0.5 H2(g) = Ag(s) + HCl(aq), and the standard acidity constant of the ion HSO4- in synthetic sea water from 273.15 to 318.15 K, *Journal of Chemical Thermodynamics*, *22*, 113–127, doi:10.1016/0021-9614(90)90074-Z, 1990.

Dlugokencky, E., K. Thoning, X. Lan, and P. Tans, NOAA Greenhouse Gas Reference from Atmospheric Carbon Dioxide Dry Air Mole Fractions from the NOAA GML Carbon Cycle Cooperative Global Air Sampling Network, 2021.

Egleston, E. S., C. L. Sabine, and F. M. M. Morel, Revelle revisited: Buffer factors that quantify the response of ocean chemistry to changes in DIC and alkalinity, *Global Biogeochemical Cycles*, *24*(1), doi:https://doi.org/10.1029/2008GB003407, 2010.

Emerson, S., and C. Stump, Net biological oxygen production in the ocean—II Remote in situ measurements of O2 and N2 in subarctic pacific surface waters, *Deep-Sea Research*, *57*, 1255–1265, doi:doi:10.1016/j.dsr.2010.06.001, 2010.

Fay, A. R., et al., SeaFlux: Harmonization of air-sea CO2 fluxes from surface pCO2 data products using a standardized approach, *Earth System Science Data*, *13*(10), 4693–4710, doi:10.5194/ESSD-13-4693-2021, 2021.

Fransner, F., et al., Acidification of the Nordic Seas, *Biogeosciences*, *19*(3), 979–1012, doi:10.5194/bg-19-979-2022, 2022.

Friedlingstein, P., et al., Global Carbon Budget 2022, *Earth Syst. Sci. Data*, *14*, 4811–4900, doi:10.5194/essd-14-4811-2022, 2022.

Frigstad, H., T. Andersen, R. G. Bellerby, A. Silyakova, and D. O. Hessen, Variation in the seston C:N ratio of the Arctic Ocean and pan-Arctic shelves, *Journal of Marine Systems*, *129*, 214–223, doi:10.1016/J.JMARSYS.2013.06.004, 2014.

Fröb, F., A. Olsen, M. Becker, L. Chafik, T. Johannessen, G. Reverdin, and A. Omar, Wintertime fCO2 variability in the subpolar North Atlantic since 2004, *Geophysical Research Letters*, *46*(3), 1580–1590, doi:10.1029/2018GL080554, 2019.

Garcia, H., and L. Gordon, Oxygen solubility in seawater: Better fitting equations, *Limnology and Oceanography*, *37*, 1307–1312, 1992.

Garcia, H., and L. Gordon, Erratum: Oxygen solubility in seawater: better fitting equations, *Limnology and Oceanography*, *38*, 656, 1993.

Garcia, H., et al., World Ocean Atlas 2018. Volume 4: Dissolved Inorganic Nutrients (phosphate, nitrate and nitrate+nitrite, silicate), *Tech. rep.*, NOAA Atlas NESDIS 84, 2019.

García-Ibáñez, M. I., Y. Takeshita, E. F. Guallart, N. M. Fajar, D. Pierrot, F. F. Pérez, W.-J. Cai, and M. Alvarez, Gaining insights into the seawater carbonate system using discrete fCO 2 measurements, *Marine Chemistry*, *245*, doi:10.1016/j.marchem.2022.104150, 2022.

Gascard, J.-C., A. J. Watson, M.-J. Messias, K. A. Olsson, T. Johannessen, and K. Simonsen, Long-lived vortices as a mode of deep ventilation in the Greenland Sea, *Nature*, *416*, 525–527, 2002.

GEBCO Bathymetric Compilation Group 2022, The GEBCO_2022 Grid - a continuous terrain model of the global oceans and land., 2022.

Glover, D. M., W. J. Jenkins, and S. C. Doney, Upper ocean 1D seasonal models, in *Modeling Methods for Marine Science*, chap. 15, pp. 365–408, Cambridge University Press, Cambridge, 2011.

Gruber, N., and J. L. Sarmiento, Large-Scale Biogeochemical-Physical Interactions in Elemental Cycles, in *The Sea*, vol. 12, edited by A. R. Robinson, J. J. McCarthy, and B. J. Rothschild, chap. 9, Wiley, 2002.

Gruber, N., et al., The oceanic sink for anthropogenic CO 2 from 1994 to 2007, *Science*, *363*(6432), 1193–1199, doi:10.1126/SCIENCE.AAU5153, 2019.

Hayduk, W., and H. Laudie, Prediction of Diffusion Coefficients for Nonelectrolytes in Dilute Aqueous Solutions, *AIChE*, *20*(3), 611–615, doi:10.1002/aic.690200329, 1974.

Hersbach, H., et al., ERA5 hourly data on single levels from 1959 to present, doi:10.24381/cds.adbb2d47, 2018.

Ho, D. T., C. S. Law, M. J. Smith, P. Schlosser, M. Harvey, and P. Hill, Measurements of air-sea gas exchange at high wind speeds in the Southern Ocean: Implications for global parameterizations, *Geophysical Research Letters*, *33*(16), doi:10.1029/2006GL026817, 2006.

Holte, J., and L. Talley, A New Algorithm for Finding Mixed Layer Depths with Applications to Argo Data and Subantarctic Mode Water Formation, *Journal of Atmospheric and Oceanic Technology*, *26*(9), 1920–1939, doi:10.1175/2009JTECHO543.1, 2009.

Hood, E. M., L. Merlivat, M. Curie, and P. T. Johannessen, Variations of fCO2 and air-sea flux of CO2 in the Greenland Sea gyre using high-frequency time series data from CARIOCA drift buoys, *Journal of Geophysical Research*, *104*(C9), 571–591, doi:10.1029/1999JC900130, 1999.

Humphreys, M. P., E. R. Lewis, J. D. Sharp, and D. Pierrot, PyCO2SYS v1.8: Marine carbonate system calculations in Python, *Geoscientific Model Development*, *15*(1), 15–43, doi:10.5194/GMD-15-15-2022, 2022.

IOC, SCOR, and IAPSO, The international thermodynamic equation of seawater - 2010: Calculation and use of thermodynamic properties, *Intergovernmental Oceanographic Commission, Manuals and Guides*, *56*, 196 pp., 2010.

Jeansson, E., A. Olsen, and S. Jutterström, Arctic Intermediate Water in the Nordic Seas, 1991–2009, *Deep Sea Research Part I: Oceanographic Research Papers*, *128*, 82–97, doi:10.1016/j.dsr.2017.08.013, 2017.

Jeansson, E., T. Tanhua, A. Olsen, W. M. J. Smethie, B. Rajasakaren, S. R. Ólafsdóttir, and J. Ólafson, Decadal Changes in Ventilation and Anthropogenic Carbon in the Nordic Seas , 2023.

Jeansson, E., et al., The Nordic Seas carbon budget: Sources, sinks, and uncertainties, *Global biogeochemical cycles*, *25*(4), doi:10.1029/2010GB003961, 2011.

Key, R. M., et al., Global Ocean Data Analysis Project, Version 2 (GLODAPv2), ORNL/CDIAC-162, NDP-P093, *Earth System Science Data (Online)*, *8*(2), doi:10.3334/CDIAC/OTG.NDP093{_}GLODAPV2, 2015.

Koelling, J., D. W. Wallace, U. Send, and J. Karstensen, Intense oceanic uptake of oxygen during 2014–2015 winter convection in the Labrador Sea, *Geophysical Research Letters*, *44*(15), 7855–7864, doi:10.1002/2017GL073933, 2017.

Körtzinger, A., J. I. Hedges, and P. D. Quay, Redfield ratios revisited: Removing the biasing effect of anthropogenic CO2, *Limnology and Oceanography*, *46*(4), 964–970, doi:10.4319/lo.2001.46.4.0964, 2001.

Landschützer, P., N. Gruber, and D. C. Bakker, Decadal variations and trends of the global ocean carbon sink, *Global Biogeochemical Cycles*, *30*(10), 1396–1417, doi:10.1002/2015GB005359, 2016.

Lauvset, S. K., A. Brakstad, K. Våge, A. Olsen, E. Jeansson, and K. A. Mork, Continued warming, salinification and oxygenation of the Greenland Sea gyre, *Tellus, Series A: Dynamic Meteorology and Oceanography*, *70*(1), 1–9, doi:10.1080/16000870.2018.1476434, 2018.

Lauvset, S. K., et al., A new global interior ocean mapped climatology: The $1° \times 1°$ GLODAP version 2, *Earth System Science Data*, *8*(2), 325–340, doi:10.5194/ESSD-8-325-2016, 2016.

Lauvset, S. K., et al., GLODAPv2.2022: the latest version of the global interior ocean biogeochemical data product, *Earth Syst. Sci. Data*, *14*, 5543–5572, doi:10.5194/essd-14-5543-2022, 2022.

Lee, K., T.-W. Kim, R. Byrne, F. Millero, R. Feely, and Y.-M. Liu, The universal ratio of boron to chlorinity for the North Pacific and North Atlantic oceans, *Geochimica et Cosmochimica Acta*, *74*, 1801–1811, doi:10.1016/j.gca.2009.12.027, 2010.

Lewis, E., D. Wallace, and L. Allison, Program developed for CO2 system calculations, *Tech. rep.*, University of North Texas Libraries, Upton, New York, 1998.

Liang, J.-H., C. Deutsch, J. C. McWilliams, B. Baschek, P. P. Sullivan, and D. Chiba, Parameterizing bubble-mediated air-sea gas exchange and its effect on ocean ventilation, *Global Biogeochemical Cycles*, *27*(3), 894–905, doi:10.1002/gbc.20080, 2013.

Liss, P. S., and L. Merlivat, Air-sea gas exchange rates: introduction and synthesis, *The Role of Air-Sea Exchange in Geochemical Cycling*, pp. 113–129, 1986.

Lorbacher, K., D. Dommenget, P. P. Niiler, and A. Köhl, Ocean mixed layer depth: A subsurface proxy of ocean-atmosphere variability, *Journal of Geophysical Research: Oceans*, *111*(C07010), 1–22, doi:10.1029/2003JC002157, 2006.

Lueker, T. J., A. G. Dickson, and C. D. Keeling, Ocean pCO2 calculated from dissolved inorganic carbon, alkalinity, and equations for K1 and K2: validation based on laboratory measurements of CO2 in gas and seawater at equilibrium, *Marine Chemistry*, *70*(1-3), 105–119, doi:10.1016/S0304-4203(00)00022-0, 2000.

Manizza, M., M. J. Follows, S. Dutkiewicz, D. Menemenlis, C. N. Hill, and R. M. Key, Changes in the Arctic Ocean CO2 sink (1996-2007): A regional model analysis, *Global Biogeochemical Cycles*, *27*(4), 1108–1118, doi:10.1002/2012GB004491, 2013.

Martin, J. H., G. A. Knauer, D. M. Karl, and W. W. Broenkow, VERTEX: carbon cycling in the northeast Pacific, *Deep Sea Research Part A. Oceanographic Research Papers*, *34*(2), 267–285, doi:10.1016/0198-0149(87)90086-0, 1987.

Martin, S., and P. Kauffman, A Field and Laboratory Study of Wave Damping by Grease Ice*, *Journal of Glacialag)*, *27*(96), 283–313, doi:10.3189/S0022143000015392, 1981.

Maurer, T. L., J. N. Plant, and K. S. Johnson, Delayed-Mode Quality Control of Oxygen, Nitrate, and pH Data on SOCCOM Biogeochemical Profiling Floats, *Frontiers in Marine Science*, doi:10.3389/fmars.2021.683207, 2021.

Metzl, N., et al., Recent acceleration of the sea surface fCO2 growth rate in the North Atlantic subpolar gyre (1993–2008) revealed by winter observations, *Global Biogeochemical Cycles*, *24*(4), doi:10.1029/2009GB003658, 2010.

Miller, L. A., M. Chierici, T. Johannessen, T. T. Noji, F. Rey, and I. Skjelvan, Seasonal dissolved inorganic carbon variations in the Greenland Sea and implications for atmospheric CO2 exchange, *Deep-Sea Research Part II: Topical Studies in Oceanography*, *46*(6-7), 1473–1496, doi:10.1016/S0967-0645(99)00031-4, 1999.

Moore, G. W. K., K. Våge, R. S. Pickart, and I. A. Renfrew, Decreasing intensity of open-ocean convection in the Greenland and Iceland seas, *Nature Climate*, doi: 10.1038/NCLIMATE2688, 2015.

Naegler, T., P. Ciais, K. Rodgers, and I. Levin, Excess radiocarbon constraints on air-sea gas exchange and the uptake of CO2 by the oceans, *Geophysical Research Letters*, *33*(11), doi:10.1029/2005GL025408, 2006.

Nakaoka, S.-I., S. Aoki, T. Nakazawa, G. Hashida, S. Morimoto, T. Yamanouchi, and H. Yoshikawa-Inoue, Temporal and spatial variations of oceanic pCO2 and air–sea CO2 flux in the Greenland Sea and the Barents Sea, *Tellus B: Chemical and Physical Meteorology*, *58*(2), 148–161, doi:10.1111/J.1600-0889.2006.00178.X, 2006.

Nicholson, D. P., S. T. Wilson, S. C. Doney, and D. M. Karl, Quantifying subtropical North Pacific gyre mixed layer primary productivity from Seaglider observations of diel oxygen cycles, *Geophysical Research Letters*, *42*(10), 4032–4039, doi:10.1002/2015GL063065, 2015.

Nilsen, J. E. Ø., and E. Falck, Variations of mixed layer properties in the Norwegian Sea for the period 1948–1999, *Progress in Oceanography*, *70*(1), 58–90, doi:10.1016/J.POCEAN. 2006.03.014, 2006.

Nondal, G., R. G. Bellerby, A. Olsen, T. Johannessen, and J. Olafsson, Optimal evaluation of the surface ocean CO2 system in the northern North Atlantic using data from voluntary observing ships, *Limnology and Oceanography: Methods*, *7*(1), 109–118, doi:10.4319/ LOM.2009.7.109, 2009.

Olsen, A., K. R. Brown, M. Chierici, T. Johannessen, and C. Neill, Sea surface CO2 fugacity in the subpolar North Atlantic, *Biogeosciences*, *5*, 535–547, 2008.

Olsen, A., A. M. Omar, E. Jeansson, L. G. Anderson, and R. G. J. Bellerby, Nordic seas transit time distributions and anthropogenic CO2, *Journal of Geophysical Research: Oceans*, *115*(C5), 5005, doi:10.1029/2009JC005488, 2010.

Orr, J. C., J. M. Epitalon, A. G. Dickson, and J. P. Gattuso, Routine uncertainty propagation for the marine carbon dioxide system, *Marine Chemistry*, *207*, 84–107, doi:10.1016/J. MARCHEM.2018.10.006, 2018.

Owens, W. B., and A. P. S. Wong, An improved calibration method for the drift of the conductivity sensor on autonomous CTD profiling floats by theta-S climatology, *Deep-Sea Research I*, *56*, 450–457, doi:10.1016/j.dsr.2008.09.008, 2009.

Perez, F., and F. Fraga, Association constant of fluoride and hydrogen ions in seawater, *Marine Chemistry*, *21*, 161–168, doi:10.1016/0304-4203(87)90036-3, 1987.

Pickart, R. S., G. W. Moore, C. Mao, F. Bahr, C. Nobre, and T. J. Weingartner, Circulation of winter water on the Chukchi shelf in early Summer, *Deep Sea Research Part II: Topical Studies in Oceanography*, *130*, 56–75, doi:10.1016/J.DSR2.2016.05.001, 2016.

Pierrot, D., et al., Recommendations for autonomous underway pCO2 measuring systems and data-reduction routines, *Deep Sea Research Part II: Topical Studies in Oceanography*, *56*(8-10), 512–522, doi:10.1016/J.DSR2.2008.12.005, 2009.

Plant, J. N., K. S. Johnson, C. M. Sakamoto, H. W. Jannasch, L. J. Coletti, S. C. Riser, and D. D. Swift, Net community production at Ocean Station Papa observed with nitrate and oxygen sensors on profiling floats, *Global Biogeochemical Cycles*, *30*(6), 859–879, doi:10.1002/2015GB005349, 2016.

Price, J. F., R. A. Weller, and R. Pinkel, Diurnal cycling: Observations and models of the upper ocean response to diurnal heating, cooling, and wind mixing, *Journal of Geophysical Research: Oceans*, *91*(C7), 8411–8427, doi:10.1029/JC091IC07P08411, 1986.

Qasem, N. A. A., M. M. Generous, B. A. Qureshi, and S. M. Zubair, A Comprehensive Review of Saline Water Correlations and Data: Part II-Thermophysical Properties, *Arabian Journal for Science and Engineering*, *46*(3), 1941–1979, doi:10.1007/s13369-020-05020-5, 2021.

Redfield, A. C., B. H. Ketchum, and F. A. Richards, The influence of organisms on the composition of seawater, *The Sea*, *2*, 26–77, 1963.

Sarmiento, J. L., and N. Gruber, *Ocean Biogeochemical Dynamics*, Princeton University Press, Princeton, 2006.

Sharqawy, M. H., J. H. Lienhard V, and S. M. Zubair, Erratum to Thermophysical properties of seawater: A review of existing correlations and data, *New pub: Balaban*, *29*(1-3), 355, doi:10.5004/DWT.2011.2947, 2012a.

Sharqawy, M. H., J. H. Lienhard V, and S. M. Zubair, Thermophysical properties of seawater: a review of existing correlations and data, *New pub: Balaban*, *16*(1-3), 354–380, doi:10.5004/DWT.2010.1079, 2012b.

Skjelvan, I., T. Johannessen, and L. A. Miller, Interannual variability of fCO2 in the Greenland and Norwegian Seas, *Tellus B: Chemical and Physical Meteorology*, *51*(2), 477–489, doi:10.3402/TELLUSB.V51I2.16327, 1999.

Stanley, R. H., W. J. Jenkins, D. E. Lott, and S. C. Doney, Noble gas constraints on air-sea gas exchange and bubble fluxes, *Journal of Geophysical Research: Oceans*, *114*(11), doi:10.1029/2009JC005396, 2009.

Sulpis, O., S. K. Lauvset, and M. Hagens, Current estimates of K1*and K2* appear inconsistent with measured CO2 system parameters in cold oceanic regions, *Ocean Science*, *16*(4), 847–862, doi:10.5194/OS-16-847-2020, 2020.

Sweeney, C., E. Gloor, A. R. Jacobson, R. M. Key, G. McKinley, J. L. Sarmiento, and R. Wanninkhof, Constraining global air-sea gas exchange for CO2 with recent bomb 14C measurements, *Global Biogeochemical Cycles*, *21*(2), doi:10.1029/2006GB002784, 2007.

Takahashi, T., J. Olafsson, J. G. Goddard, D. W. Chipman, and S. C. Sutherland, Seasonal variation of CO2 and nutrients in the high-latitude surface oceans: A comparative study, *Global Biogeochemical Cycles*, *7*(4), 843–878, doi:10.1029/93GB02263, 1993.

Thierry, V., and H. Bittig, Argo Quality Control Manual for Dissolved Oxygen Concentration Argo Quality Control Manual for Dissolved Oxygen Concentration, v2.0, *Tech. rep.*, doi:10.13155/46542, 2018.

Uppström, L. R., The boron/chlorinity ratio of deep-sea water from the Pacific Ocean, *Deep Sea Research and Oceanographic Abstracts*, *21*(2), 161–162, doi:10.1016/0011-7471(74)90074-6, 1974.

Våge, K., R. S. Pickart, G. W. Moore, and M. H. Ribergaard, Winter Mixed Layer Development in the Central Irminger Sea: The Effect of Strong, Intermittent Wind Events, *Journal of Physical Oceanography*, *38*(3), 541–565, doi:10.1175/2007JPO3678.1, 2008.

Våge, K., G. W. Moore, S. Jónsson, and H. Valdimarsson, Water mass transformation in the Iceland Sea, *Deep Sea Research Part I: Oceanographic Research Papers*, *101*, 98–109, doi:10.1016/J.DSR.2015.04.001, 2015.

Vagle, S., C. McNeil, and N. Steiner, Upper ocean bubble measurements from the NE Pacific and estimates of their role in air-sea gas transfer of the weakly soluble gases nitrogen and oxygen, *Journal of Geophysical Research: Oceans*, *115*(C12), doi:10.1029/2009JC005990, 2010.

Visbeck, M., J. Fischer, and F. Schott, Preconditioning the Greenland Sea for deep convection: Ice formation and ice drift, *JOURNAL OF GEOPHYSICAL RESEARCH*, *100*(C9), 489–507, doi:10.1029/95JC01611, 1995.

Wang, C., R. M. Graham, K. Wang, S. Gerland, and M. A. Granskog, Comparison of ERA5 and ERA-Interim near-surface air temperature, snowfall and precipitation over Arctic sea ice: effects on sea ice thermodynamics and evolution, *Cryosphere*, *13*(6), 1661–1679, doi:10.5194/TC-13-1661-2019, 2019.

Wang, X., J. Zhao, T. Hattermann, L. Lin, and P. Chen, Transports and Accumulations of Greenland Sea Intermediate Waters in the Norwegian Sea, *Journal of Geophysical Research: Oceans*, *126*(4), doi:10.1029/2020JC016582, 2021.

Wanninkhof, R., Relationship between wind speed and gas exchange over the ocean, *Journal of Geophysical Research*, *97*(C5), 7373, doi:10.1029/92JC00188, 1992.

Wanninkhof, R., Relationship between wind speed and gas exchange over the ocean revisited, *Limnology and Oceanography: Methods*, *12*(6), 351–362, doi:10.4319/LOM.2014.12.351, 2014.

Wanninkhof, R., and W. R. McGillis, A cubic relationship between air-sea CO2 exchange and wind speed, *Geophysical Research Letters*, *26*(13), 1889–1892, doi:10.1029/1999GL900363, 1999.

Wanninkhof, R., W. E. Asher, D. T. Ho, C. Sweeney, and W. R. McGillis, Advances in Quantifying Air-Sea Gas Exchange and Environmental Forcing, *Annual Review of Marine Science*, *1*(1), 213–244, doi:10.1146/annurev.marine.010908.163742, 2009.

Weiss, R. F., The solubility of nitrogen, oxygen and argon in water and seawater, *Deep-Sea Research and Oceanographic Abstracts*, *17*(4), 721–735, doi:10.1016/0011-7471(70)90037-9, 1970.

Weiss, R. F., Carbon dioxide in water and seawater: the solubility of a non-ideal gas, *Marine Chemistry*, *2*(3), 203–215, doi:10.1016/0304-4203(74)90015-2, 1974.

Weiss, R. F., and B. Price, Nitrous oxide solubility in water and seawater, *Marine Chemistry*, *8*, 347–359, doi:10.1016/0304-4203(80)90024-9, 1980.

Wolf, M. K., R. C. Hamme, D. Gilbert, I. Yashayaev, and V. Thierry, Oxygen Saturation Surrounding Deep Water Formation Events in the Labrador Sea From Argo-O2 Data, *Global Biogeochemical Cycles*, *32*(4), 635–653, doi:10.1002/2017GB005829, 2018.

Wong, A., R. Keeley, and T. Carval, Argo Quality Control Manual for CTD and Trajectory Data Version 3.7, *Tech. rep.*, doi:10.13155/33951, 2023.

Woolf, D. K., *Bubbles and their role in gas exchange*, 1997.

Woolf, D. K., and S. A. Thorpe, Bubbles and the air-sea exchange of gases in near-saturation conditions, *Journal of Marine Research*, *49*(3), 435–466, doi:10.1357/002224091784995765, 1991.

Yasunaka, S., et al., Mapping of the air–sea CO2 flux in the Arctic Ocean and its adjacent seas: Basin-wide distribution and seasonal to interannual variability, *Polar Science*, *10*(3), 323–334, doi:10.1016/J.POLAR.2016.03.006, 2016.

Zeebe, R. E., History of Seawater Carbonate Chemistry, Atmospheric CO2, and Ocean Acidification, *https://doi.org/10.1146/annurev-earth-042711-105521*, *40*, 141–165, doi:10.1146/ANNUREV-EARTH-042711-105521, 2012.